THESIS FOR THE DEGREE OF DOCTOR OF PHILOSOPHY

Alkali Chloride-Induced High-Temperature Corrosion of Alloys

Utilising long-term corrosion mechanisms to predict boiler corrosion

VICENT SSENTEZA

Department of Chemistry and Chemical Engineering

CHALMERS UNIVERSITY OF TECHNOLOGY

Gothenburg, Sweden 2025

Alkali Chloride-Induced High-Temperature Corrosion of Alloys

Utilising long-term corrosion mechanisms to predict boiler corrosion

VICENT SSENTEZA

ISBN 978-91-8103-183-6

Doktorsavhandlingar vid Chalmers tekniska högskola

Ny serie nr 5641

ISSN 0346-718X

Department of Chemistry and Chemical Engineering

Chalmers University of Technology

SE-412 96 Gothenburg

Sweden

Telephone + 46 (0)31-772 1000

Cover:

SEM-SE image showing surface morphology of a Ni-based alloy after exposure to 5% O_2 + 20% H_2O + N_2 (Bal) + KCl(s)/KCl(g) at 600°C for 8000 hours.

Left: a region that has experienced scale spallation.

Right: a region with oxide scale intact, displaying the iron-rich oxide whiskers in between potassium chromate particles.

Printed by Chalmers Digitaltryck

Gothenburg, Sweden 2025

Alkali Chloride-Induced High-Temperature Corrosion of Alloys

Utilising long-term corrosion mechanisms to predict boiler corrosion

VICENT SSENTEZA

Department of Chemistry and Chemical Engineering

Chalmers University of Technology

Abstract

Biomass and waste fuels show strong potentials as alternative renewable energy sources that can help meet the increasing global energy demand while reducing the net release of CO_2 into the atmosphere. The combustion of biomass and waste is however associated with the release of flue gases that contain high levels of alkali salts (e.g., KCl) that cause breakaway oxidation, and this leads to accelerated corrosion of metallic boiler components. The rapid corrosion restricts boiler operating parameters, i.e., steam temperature and pressure, and thereby limits the electrical efficiency. One way to tackle this issue is to use more-corrosion-resistant materials for boiler applications, to enable operations at higher temperatures and pressures. To achieve this, it is crucial to gain an in-depth understanding of the corrosion mechanisms of boiler materials. However, there is lack of comprehensive long-term investigations that have employed well-controlled systems to elucidate the corrosion phenomenon as well as the long-term corrosion kinetics.

To date, most of the high-temperature corrosion studies related to biomass and waste combustion have involved short-term laboratory investigations with a focus on understanding the initial stages of corrosion. This thesis concerns long-term high-temperature corrosion research in the laboratory through the development of a state-of-the-art experimental set-up that mimics key corrosive species in the boiler environment at a relevant temperature. This approach offers the possibility to study several materials and coatings with the aim of evaluating the corrosion properties during long-term exposure to the corrosive environment. The corrosion products are characterised using x-ray diffraction (XRD) and advanced electron and ion microscopy, such as SEM/EDX, EBSD and TEM, on cross-sections prepared using broad ion beam (BIB) milling and focused ion beam (FIB) milling. Moreover, thermodynamic calculations and kinetics-based simulations are applied to elucidate the growth mechanisms of oxide scales.

The results reveal that all of the investigated alloys experience breakaway oxidation and form multi-layered oxide scales, referred to as secondary protection. Secondary protection could be divided into two categories in the presence of KCl: (i) fast-growing and less-protective iron-rich oxide scales, representing poor secondary protection; and (ii) slow-growing and more-protective chromium/aluminium-rich corundum-type oxide scales, representing good secondary protection. The long-term oxidation kinetics studies in the presence of KCl, together with the oxide microstructural evolution showed that the scale growth is diffusion-controlled, and that the properties of the secondary protection may be influenced by the alloying elements and the bulk microstructure. In addition, the findings showed that long-term laboratory oxidation kinetics can be utilised to understand the mechanism and predict the corrosion of metals in the complex boiler environment. The insights gained from this thesis will help to improve predictions of material corrosion and facilitate the design and development of high-temperature alloys.

Keywords: Biomass, Waste, High-temperature corrosion, Alkali chloride, Primary protection, Breakaway, Secondary protection, Alloys

List of appended papers

This thesis is based on the following papers:

Paper I
V. Ssenteza, J. Eklund, I. Hanif, J. Liske, T. Jonsson, High temperature corrosion resistance of FeCr(Ni, Al) alloys as bulk/overlay weld coatings in the presence of KCl at 600 °C, Corros Sci 213 (2023) 110896. https://doi.org/10.1016/J.CORSCI.2022.110896

Paper II
I. Hanif, V. Ssenteza, J. Eklund, J. Nockert Olovsjö, T. Jonsson, High-temperature corrosion of weld overlay coating/bulk FeCrAl exposed in O_2 + H_2O + KCl(s) at 600 °C – A microstructural investigation, Journal of Materials Research and Technology 25 (2023) 7008–7023. https://doi.org/10.1016/j.jmrt.2023.07.073

Paper III
V. Ssenteza, J. Eklund, S. Bigdeli, T. Jonsson, Long-term corrosion behavior of FeCr(Al, Ni) alloys in O_2 + H_2O with KCl(s) at 600 °C: Microstructural evolution after breakaway oxidation, Corros Sci 226 (2024) 111654. https://doi.org/10.1016/j.corsci.2023.111654

Paper IV
J. Eklund, A. Persdotter, V. Ssenteza, T. Jonsson, The long-term corrosion behavior of FeCrAl(Si) alloys after breakaway oxidation at 600 °C, Corros Sci 217 (2023) 111155. https://doi.org/10.1016/j.corsci.2023.111155

Paper V
V. Ssenteza, T. Jonsson, J. Nockert, J. Liske, The Impact of HCl on Alkali-Induced Corrosion of Stainless Steels/FeCrAl Alloy at 600 °C: The Story After Breakaway, High Temperature Corrosion of Materials (2024). https://doi.org/10.1007/s11085-024-10265-8

Paper VI
V. Ssenteza, M.D.P. Olausson, J. Eklund, J. Nockert, J. Liske, T. Jonsson, High-Temperature Corrosion Behavior of Superheater Materials at 600 °C: Insights from Laboratory and Field Exposures, Energy & Fuels (2024). https://doi.org/10.1021/acs.energyfuels.4c04806

Paper VII

V. Ssenteza, L. Rioja-Monllor, A. Chyrkin, T. Sand, R. Siriki, T. Jonsson, New insights into oxidation-driven grain refinement in Ni-containing alloys at 600 °C. Submitted 2025, Materials & Design.

Statement of the author's contribution

Paper I: I am the principal author, and contributed with conceptualization, performed all the exposures, performed the analyses and wrote the original draft and the final review.

Paper II: I contributed with performing corrosion exposures, some post-exposure analyses (gravimetric analysis and SEM imaging), conceptualization, and writing – review and editing of the manuscript.

Paper III: I am the principal author, and contributed with conceptualization, performance of corrosion exposures, sample analyses (SEM/EDX and EBSD), data curation and wrote the original draft and the final review.

Paper IV: I co-authored this paper and contributed with the development of certain aspects of the corrosion exposure set-up, investigation and writing – review and editing of the manuscript.

Paper V: I am the principal author, and contributed with conceptualization, performed all the corrosion exposures, post-exposure analysis, data curation, and writing of the original draft and the final review.

Paper VI: I am the principal author, and contributed with conceptualization, performed some of the corrosion tests (laboratory exposures), analysed the samples from laboratory corrosion exposures, data curation, and writing of the original draft and review.

Paper VII: I am the principal author, and contributed with conceptualization, performed some of the corrosion exposures, performed some analyses (SEM/EDX and XRD), data curation, and writing of the original draft and review.

Related work not included in this thesis

A. Persdotter, T. Boll, V. Ssenteza, T. Jonsson, Insight into the influence of alloying elements on the secondary corrosion protection of Fe-base alloys by means of atom probe tomography, Corros Sci 235 (2024) 112175. https://doi.org/10.1016/j.corsci.2024.112175.

A. Agüero, P. Audigié, S. Rodríguez, M. Gutiérrez del Olmo, J. Pascual, V. Ssenteza, T. Jonsson, L.-G. Johansson, Rapid α-Al_2O_3 Growth on an Iron Aluminide Coating at 600 °C in the Presence of O_2, H_2O, and KCl, ACS Appl Mater Interfaces (2024). https://doi.org/10.1021/acsami.4c11719.

Acknowledgements

First and foremost, I would like to express my sincere gratitude to my supervisors; Dr. Torbjörn Jonsson, Assoc. Prof. Jesper Liske and Prof. Jan-Erik Svensson for granting me the opportunity to pursue my doctoral studies in the field of high-temperature corrosion. I am very thankful for all the support, time and invaluable discussions we have had throughout this journey. Your guidance has been truly inspirational and consistently keeping me on track. I am especially grateful for the open communication and the support you have provided, both in my professional work and in matters related to my family. Our trips to conferences have been both enjoyable and enriching.

Furthermore, I would like to extend my appreciation to Prof. Lars-Gunnar Johansson and Prof. Itai Panas for the insightful scientific discussions we have shared. These conversations have been very valuable for my growth as a researcher.

I am also grateful to all my colleagues at the Energy and Materials Division, both past and present, that have been with me during this journey. I appreciate the scientific and non-scientific discussions we have had. Fika times and after-work gatherings have always been fun! My heartfelt gratitude to Dolores Paz Olausson, Johan Eklund, Hampus Lindmark, Tommy Sand, Anton Chyrkin, Aina Edgren and Christine Geers for their valuable discussions and assistance with both practical and theoretical aspects of experimentation and microscopy. To Sandra Nayeri, thank you so much for always being available and for your tireless support with administrative matters.

I would also like to acknowledgement our industrial partners, Alleima AB, Kanthal AB and Vallourec SA, for your support in providing a wide range of materials and coatings used in this work. Thank you to the CMAL group for their technical support with microscopy. A special thank you to Laura Rioja-Monllor for the insightful discussions we have had about my research and for all the support during my time as a member of your PhD student network.

Finally, I am profoundly grateful to my family, parents, siblings, and parents-in-law, for all their support and encouragement. Most importantly, I extend my deepest gratitude to my wife and children for making this achievement possible. Thank you for your understanding and immense patience with me during this work. It has been a challenging journey, but you kept me grounded and motivated. My wife, Edlira, you have been the source of strength throughout this journey. Thank you for believing in me—I am forever grateful!

Vicent Ssenteza, Gothenburg (2025)

to my wife

Table of Contents

1 Introduction

1.1 Background

The increasing global demand for energy is a driving force for innovation and advances in energy infrastructure. As the world population increases and more energy-intensive industries emerge, the demand for energy increases. According to the Year 2024 report of the International Energy Agency (IEA) [1], global energy consumption in Year 2023 was 445 EJ (1EJ = 277.8 TWh), and this level is projected to rise steadily to over 530 EJ by Year 2050. Currently, fossil fuels such as coal, oil, and natural gas are the main sources of the energy supply (see Figure 1.1). However, the use of fossil fuels has led to increased emissions of greenhouse gases, such as CO_2 and N_2O, which are linked to global warming [2–4]. To combat climate change, there is an urgent need to find alternative energy sources that meet the energy demand and that have no or reduced impact on climate change.

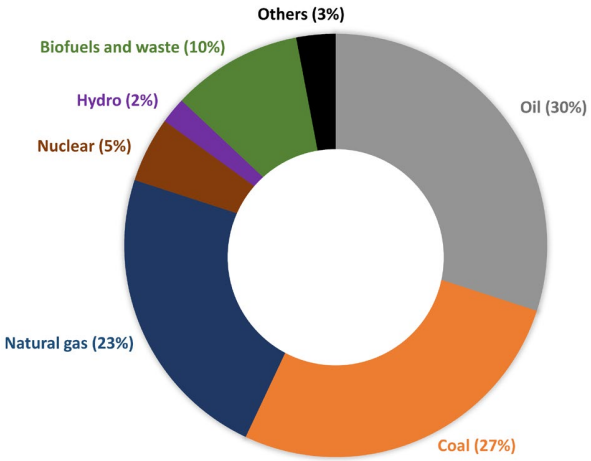

Figure 1.1: World total energy supply by source for electricity and heat generation, according to the International Energy Agency 2024 report [1].

One solution is to use renewable energy sources, such as wind energy, solar energy, bioenergy, geothermal energy, and hydropower. Currently, these renewable energy sources constitute about 15% of the total global energy supply, with biofuels and waste together constituting the largest contribution (10%). The combustion of biofuels derived from biomass and waste for combined heat and power (CHP) production has been incorporated successfully into various energy conversion systems around the world to meet the high energy demands. With the aim to improve boiler performance and reduce CO_2 emissions into the atmosphere during the combustion of biomass and waste, several advances have been made in the CHP technology. For example, the secondary air supply [5] and the integrated biomass multi-stage gasification system [6] have been installed to improve the conversion of fuels into heat and power. A more-recent development is the bioenergy with carbon capture and storage (BECCS) technology, which can be installed to remove CO_2 in

the post-combustion process [7]. This set-up provides the unique possibility to remove large amounts of CO_2 and facilitate the transition to negative emissions. However, the efficiency of electricity generation from the combustion of biomass and waste has remained relatively low, as compared with electricity generation from the combustion of fossil fuels. One challenge associated with electricity generation from the combustion of biomass and waste is the accelerated corrosion of metallic components of the boilers (e.g., the superheater tubes). It is well-established that the accelerated corrosion in the boiler environment is mainly caused by species, such as KCl, NaCl, HCl, and H_2O, which are formed during the combustion of biofuels and waste [8–26]. These species can break down the protective oxide scales of the alloys (i.e., primary protection), leading to the formation of fast-growing, multi-layered oxide scales that are less protective (i.e., secondary protection). The severe corrosion in the boiler leads to rapid material degradation, tube failures, and costly unplanned plant shut-downs.

Several counter-measures have been proposed to mitigate corrosion in biomass- and waste-fired boilers. One strategy is to reduce the steam temperature of the boiler, which leads to a lower material temperature and, thereby, reduced corrosion. However, reducing the steam temperature leads to lower electrical efficiency. Another approach is to use additives, e.g., ammonium sulphate, which mitigates the alkali chloride-induced corrosion through the capture of potassium (K) and sodium (Na) [27]. A promising solution is the use of more-corrosion resistant materials such as stainless steels (>10.5 wt% Cr), which may offer improved corrosion protection by re-forming the protective oxide scales after breakaway oxidation in harsh environments. Currently, low-alloyed steels are the preferred choice of materials due to their low cost and improved mechanical properties, such as creep strength [28]. A more-advanced material solution is to use metallic coatings, whereby an alloy with improved corrosion resistance is combined with a low-alloyed steel (substrate) with good mechanical properties. Among the many coating techniques developed over the last decades, overlay welding has been widely adopted for boiler applications due to its practical benefits with regards to on-site repairs and its relative ease of implementation [29]. It therefore becomes necessary to understand the corrosion behaviours of newly developed materials and coating systems and to be able to predict their life-times.

In order to provide material solutions to meet future demands related to combustion of biomass/waste, insights into the long-term corrosion mechanisms for the formation of good secondary protection are needed. This information may provide criteria for the selection of materials that enable boiler operations for high steam data. However, there are currently few well-controlled, long-term laboratory investigations into the detailed microstructural evolution of the oxide scales formed in alkali chloride-rich environments relevant to boiler applications. Figure 1.2 shows a summary of the published articles on high-temperature corrosion related to biomass and waste combustion plotted against exposure times. From the data, it can be concluded that the majority of the conducted laboratory studies have been relatively short in duration (up to 1000 hours), whereas field studies have been dominated by longer exposure times. The reason for this may be the high cost of laboratory exposures, such that the exposure time is kept to a minimum. For the initiation of the corrosion attack, short laboratory exposures are adequate, and corrosion mechanisms can be derived. However, if corrosion predictions and determination of the life-times of metallic components in full-scale power plants are the main features of interest, long-term studies are lacking. To date, most of the studies involving longer exposure times have only been performed with field exposures.

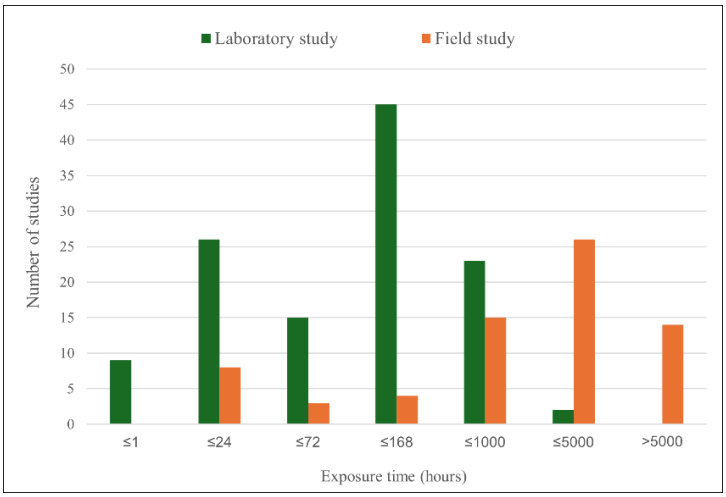

Figure 1.2: Diagram showing the distribution of studies (based on 190 research articles) that have investigated alkali chloride-induced high-temperature corrosion of materials and coatings for biomass- and waste-fired boiler applications.

Long-term field studies (≥1000 hours) in pilot plants and full-scale boilers are conducted to acquire knowledge about the extent of the corrosion attack rather than about the mechanism of the corrosion attack. Such long field exposures are enabled by the use of temperature-controlled corrosion probes, fixed installations, and a less-stringent requirement for control of the exposure conditions. On the other hand, laboratory investigations mostly entail short-term exposures in well-controlled systems and experimental conditions, resulting in controlled kinetics with reliable data. The challenge is how to utilise the pool of laboratory findings to gain further insights and predict corrosion behaviours in complex boiler environments.

1.2 **Aim**

The aim of this thesis is to develop and utilise long-term laboratory corrosion mechanisms in order to understand and predict the corrosion of materials and coatings used for applications in biomass- and waste-fired boilers. The strategy addresses two primary research questions:

> **Research question 1.** What are the mechanisms that control the formation of good/poor secondary protection on FeCr(Ni), NiCr and FeCrAl(Si) alloys during long-term laboratory exposures to KCl at 600°C?
>
> **Research question 2.** How can long-term corrosion kinetics under laboratory conditions be used to understand the mechanisms and predict oxidation behaviour in complex boiler environment?

The approach adopted in this thesis has been to conduct high-temperature corrosion investigations in the laboratory by developing a state-of-the-art experimental set-up in which corrosive species (KCl) could be present on the sample surface during long exposures. The corrosion studies involved exposing FeCr(Ni), NiCr and FeCrAl(Si) alloys (commercial, model bulk materials and overlay weld coatings) to an environment that consisted of 5% O_2 + 20% H_2O + N_2 (Bal) + KCl(s)/KCl(g) at 600°C. In addition, field

studies were carried out in commercial biomass- and waste-fired boilers using corrosion probes, and materials from fixed installations were also examined. Characterisation of the corrosion products was performed using scanning electron microscopy (SEM) in combination with energy-dispersive x-ray (EDX) spectroscopy, x-ray diffraction (XRD), electron back-scattered diffraction (EBSD) and transmission electron microscopy (TEM), on cross-sections prepared using gentle sample preparation techniques, such as broad ion beam (BIB) milling and focused ion beam (FIB) milling. Computational methods, e.g., thermodynamic calculations and kinetic-based simulations, were performed to predict the oxide phases and growth kinetics.

2 Combined heat and power plants

Combined heat and power (CHP) plants deploy various technologies to produce electricity and useful heat from a variety of fuels. The electricity/heat produced by these plants is integrated into home, district, and industrial heating systems. Many of the CHP plants are based on the Rankine cycle process in which steam from the boiler is re-heated at a constant pressure to create high-pressure steam that is above the saturation point. The steam expands in the gas turbine, which produces useful work and runs the generator that produces electricity [30]. The produced heat is recovered and can be supplied to a district heating system. Fuel feedstocks, such as coal, natural gas, biofuels, and waste, can be combusted. During the combustion process, the operating parameters related to steam temperature and pressure must be carefully selected so as to meet both the technical requirements and human safety regulations.

According to a report issued by the European Commission's Directorate-General, the number of installed CHP units has been steadily increasing across the European Union (EU) since 2005, which has led to an increased electricity supply for the Member States [31]. Currently, most CHP plants operate with super-critical (SC) steam conditions in the Rankine cycle (>374°C/221 bar). A few coal-fired plants operate with ultra-super-critical (USC) steam conditions (>600°C/270 bar). However, no commercial biomass-fired or waste-fired plants currently operate under USC steam conditions. The USC steam conditions yield higher efficiencies of electricity generation than the SC steam conditions. Depending on the type of fuel being combusted and the thermodynamic parameters of the process, different electrical efficiencies can be achieved. The electricity generation efficiencies are in the ranges of [32]: 27%–43% for coal; 31%–55% for natural gas; 23%–43% for oil; 25%–30% for biomass, and 20%-30% for waste.

Although the electrical efficiency derived from the combustion of biofuels is low, these fuels represent attractive options for meeting the increasing energy demands while reducing net greenhouse gas emissions. One challenge associated with the combustion of biofuels, which also affects the efficiency of electricity generation, is the severe corrosion of the metallic components of the boilers that occurs in the temperature range of 450°C–580°C (steam temperatures) [26]. This severe corrosive attack has been attributed to the presence of alkali salts that are created during the combustion of biofuels [9,11,20,21,23]. In general, the expected life-times of superheater materials are short. For example, a 16Mo3 steel or 13CrMo4-5 steel installed in a waste-fired boiler operating under normal conditions has a life-time of about 3 years [33]. Nonetheless, CHP plants based on the biofuel combustion technology are economically and environmentally viable. Therefore, it is worth exploring the potentials of biofuels as energy sources for the supply of small-scale and large-scale energy demands.

2.1 Biofuels and waste

Biofuels are fuels that are derived directly or indirectly from biomass, which originates from organic materials. The term ‘biomass’ covers a diversity of organic materials, which can be categorised into the following groups:

1. Solid biofuels (e.g., wood, agricultural products, waste etc.).
2. Liquid biofuels (e.g., biodiesel); and
3. Biogas (e.g., methane).

For CHP plants that are operating with biomass, solid biofuels are the most commonly used feedstocks, constituting about 70% of the total use of biomass for electricity generation [34]. Therefore, the focus of this study is on solid biofuels. Figure 2.1 provides a summary of the different sources of solid biofuels consumed in electricity-generating plants within the EU. In recent decades, wood feedstocks have become the main source of energy, whereby they are combusted directly in the forms of wood chips and fellings (e.g., tops, bark, stumps and branches) or indirectly in the forms of saw-milling residues and by-products from the pulp and paper industry.

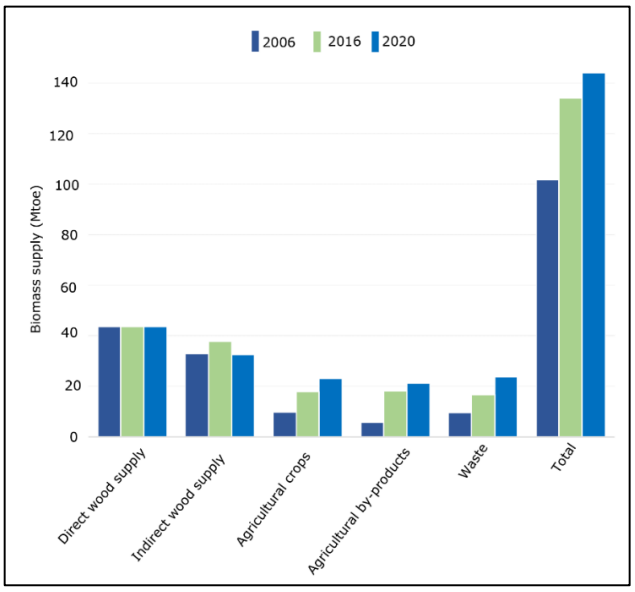

Figure 2.1: Sources of biomass for the production of electricity within the EU for Years 2006, 2016, and 2020. The data shown are based on progress reports from EU Member States and reported by the Joint Research Centre (JRC) [35].

Agricultural feedstocks, which include residues from agricultural harvesting and dedicated agricultural crops (e.g., straw and maize), show strong potentials as renewable fuels. There are many advantages linked to using agricultural feedstocks, such as good availability and low cost of production. The potential of agricultural feedstocks for CHP plants is evident today, with 15 large CHP plants in the EU operating on straw and less than 8% of the theoretical potential of agricultural straw currently being exploited [36]. This indicates that straw will continue to play an important role in the energy sector. Table 2.1 lists the chemical compositions of the various biofuels/waste in comparison to coal.

Burnable bio-waste materials, such as municipal solid waste (MSW), sludge, and waste from industrial processes may also be used as feedstocks in CHP plants. These materials are collected and transported to collecting sites where they are sorted and distributed to the power plants. However, waste streams pose additional challenges for the combustion technology, as they exhibit diverse fuel characteristics and fractions (e.g., plastics, rubber, and electronics), which contain high levels of alkali salts and heavy metals.

Thus, the operating parameters for the boilers must be carefully chosen to ensure human safety and high conversion rates, while minimising corrosion and emissions of air pollutants.

Table 2.1: Compositions of the various species in selected solid biofuels [37].

Fuel source	**Ash** (wt%)	**H_2O** (wt%)	**Cl** (wt%)	**S** (wt%)	**C** (wt%)	**K** (mg/kg) dry	**Na** (mg/kg) dry
Wood	0.6	15.9	0.03	<0.5	51.2	680	30
Straw	8.6	10.4	0.59	<0.5	48.8	11634	610
Sewage Sludge	19.4	64.3	0.43	<0.5	51.2	1652	1725
MSW	6–25	12–40	0.45–1.0	<0.5	54	60–200	40–100
Coal	11.8	8.1	0.25	1.4	79.4	1287	1142

2.2 Biomass-fired and waste-fired boilers

Multiple factors influence the design and construction of the boilers in CHP plants. These factors include combustion temperature, pressure, capacity, material, and fuel type. The main types of boilers used for biomass and waste combustion are grate-fired boilers and fluidised bed boilers.

Grate-fired boiler

Figure 2.2 depicts a moving grate-firing system at the Avedøre power plant in Denmark as an example. In this system, biomass or waste feedstock is fed above the grate using a rotary rake system. The grate then moves with a specific motion to ensure appropriate mixing of the fuel. Pre-heated primary air is supplied from beneath the grate to drive the ignition of the fuel. To ensure complete combustion of the organic material and to reduce emissions, extra air is supplied in the secondary air supply system through air nozzles that are situated above the grate. The resulting ash is removed at the bottom through a vibrating motion of the grate. Grate-fired boilers have high levels of efficiency and can be used for the combustion of diverse biofuels [38].

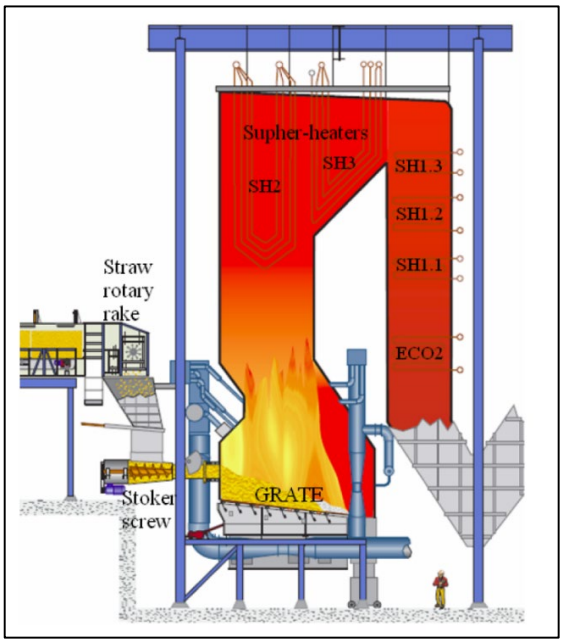

Figure 2.2: schematic of the moving grate boiler at Avedøre power plant [38].

Fluidised bed boilers

The fluidised bed combustion (FBC) technology uses a bed material, e.g., natural sand that becomes fluidised when air is passed through it at high velocity. In this system, fuel particles are suspended in hot bed materials under pressurised air that is supplied from beneath (primary air duct) and from the side (secondary air duct) (Figure 2.3). In general, there are two types of fluidised bed boilers: circulating fluidised bed (CFB) boilers; and bubbling fluidised bed (BFB) boilers. The advantage of CFB over BFB is its high efficiency, as the unburned fuel particles can be re-circulated into the combustion chamber for further combustion. Currently, most of the large CHP plants are based on the CFB technology.

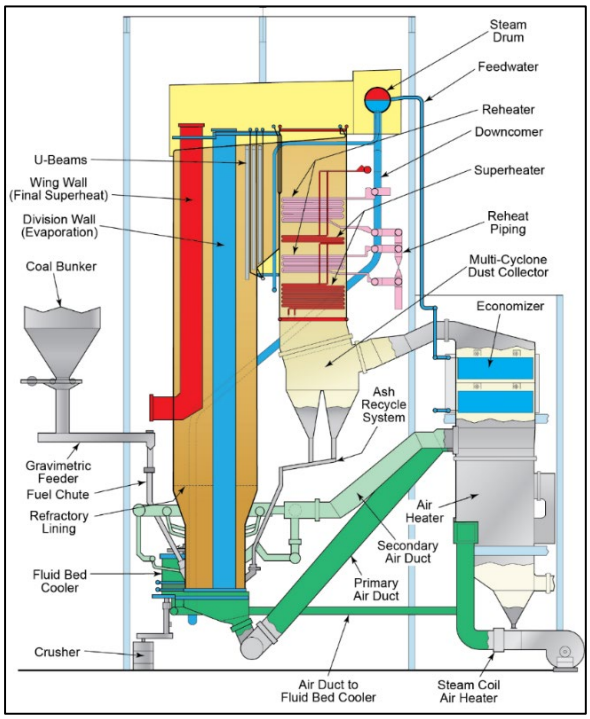

Figure 2.3: Schematic of the Fluidised bed boiler. Courtesy of The Babcock & Wilcox Company [39]

In comparison to a grate-fired boiler, a fluidised bed boiler ensures better mixing of the fuel, which results in high combustion efficiencies. Stringent control of the temperatures across the heating chamber makes it possible to combust completely fuels with challenging characteristics, such as high moisture contents and high ignition values. However, the main disadvantage of the fluidised bed boiler is its sensitivity to fuels that can cause agglomeration of the bed. Bed materials such as natural sand can interact with alkali species in the fuel to form molten alkali alumino-silicate and alkali silicate compounds that stick to the bed particles and promote agglomeration. The problem of bed agglomeration may be mitigated by using more-suitable bed materials. For example, in a study that investigated the interactions between ash components and bed materials, it was found that bed agglomeration could be reduced by using ilmenite, which effectively captures alkali species during fuel combustion without forming a melt [40].

3 High-temperature alloys

Alloy is a term that is used to describe a metallic substance that comprises several elements that form a compound. Alloys can be classified based on their content of alloying elements or the type of oxide scales that form when exposed to an oxidising environment. When developing high-temperature alloys, it is essential to consider their corrosion properties, as enhanced corrosion resistance increases the material life-time. In addition, the mechanical properties, such as tensile strength and creep strength should be taken into consideration. During alloy production, elements such as chromium, aluminium, molybdenum, silicon, tungsten, and cobalt may be added to improve the corrosion resistance, mechanical properties, or both. While the focus of this thesis is on the corrosion properties of these alloys (whether bulk materials or coatings), their mechanical properties remain an important consideration. The next section provides an overview of high-temperature alloys, classified according to their chemical compositions and the types of oxides they may form.

3.1 Alloy classification based on content of alloying elements

Low-alloyed steels contain small amounts of alloying elements. Typically, these alloys contain less than 2.5 wt% chromium [41]. Low-alloy steels are usually inexpensive and exhibit good mechanical properties, which makes them good candidate materials for applications where they act as load bearers, for example in steam boilers. However, in alkali-rich environments and at high temperatures, these materials suffer accelerated corrosion, which shortens their life-times.

Stainless steels should contain at least 10.5 wt% chromium and a maximum of 1.2 wt% carbon [42]. The chromium content contributes to the formation of a chromium-rich oxide scale, which forms a protective oxide scale. Stainless steels include:

Martensitic stainless steels:

These Fe-Cr-C steels are produced by rapidly cooling (quenching) austenite, whereby carbon gets trapped in the iron lattice and martensite is created. During the quenching process, the face-centred cubic (FCC) structure is transformed into a body-centred tetragonal (BCT) structure. Martensitic steels possess good mechanical properties, such as high creep strength, tensile strength, and toughness.

Ferritic stainless steels

Ferritic stainless steels have the BCC structure and may contain chromium in the concentration range of 11–30 wt%, with very little or no nickel [43]. These steels exhibit better corrosion resistance than low-alloyed steels in aggressive environments. Moreover, they possess favourable mechanical properties, such as high yield strength, which are desirable for the boiler components, e.g., superheater tubes.

Austenitic stainless steels:

Austenitic stainless steels have the FCC structure. Typically, these steels contain >18 wt% chromium and a minimum of 8 wt% nickel to stabilise the FCC structure [43]. These materials exhibit high levels of corrosion resistance in several harsh environments. In addition, this steel class exhibits other desirable properties, such as high weldability (which makes it easy to apply them as a coating), and improved strength and creep resistance (desirable for high-temperature applications).

Nickel-based alloys typically contain nickel as the principal element (in the range of 35–80 wt%) and have the FCC structure. These alloys exhibit superior corrosion resistance and good mechanical properties, and can be applied in various aggressive environments or in high-temperature systems. In addition to Ni, various alloying elements, such as chromium, molybdenum, copper, titanium, aluminium, and cobalt, may be incorporated into the alloy matrix to confer specific properties. In general, nickel-based alloys are much more expensive than the previously described alloy classes. Despite their high cost, many of these materials, such as Alloy 625, Alloy 600 and Alloy 800, are employed as components in regions of the boiler that experience severe corrosion and erosion, e.g., the superheaters and loop seals.

3.2 Alloy classification based on oxide scale formation

3.2.1 Iron-oxide formers

Iron oxide-forming alloys, e.g., low-alloyed steels, are materials designed to form iron oxides on their surfaces when exposed to oxidising environments. These alloys form in particular wüstite (FeO - above 570°C [44]), magnetite (Fe_3O_4), and hematite (Fe_2O_3). The iron oxide-forming alloys have numerous industrial applications, where cost-effectiveness and moderate performance are sufficient, as in construction, railways, etc. However, for applications in high-temperature or aggressive environments, these alloys become less-effective and suffer accelerated corrosion, which reduces their life-times.

3.2.2 Chromia-forming alloys

Chromia-forming alloys are able to form chromium-rich oxide scales, $(Fe,Cr)_2O_3$ or Cr_2O_3, during high-temperature oxidation. The formation of $(Fe,Cr)_2O_3$ or Cr_2O_3 requires that the alloy has a sufficient amount of chromium in the alloy matrix to facilitate formation of the scale on the surface. In boiler environments and in the intermediate temperature range, i.e., ~400°C–600°C, stainless steels (≥10.5 wt% Cr) typically form $(Fe,Cr)_2O_3$ scales. However, in these aggressive environments, the chromia-rich oxide scale is broken down through alkali-chromate formation [45], which limits its protective capability.

3.2.3 Alumina-forming alloys

Alumina-forming alloys are designed to form a protective layer of aluminium oxide (alumina) on their surfaces when exposed to high-temperature and oxidising environments. Typically, these alloys form protective alumina scales at temperatures >900°C, which means that they can be used in heating elements,

furnaces, and turbine components [46]. In the case of alumina-forming FeCrAl alloys, it has recently been shown that the corrosion behaviours of these alloys can be improved by the addition of silicon at 600°C [47–49].

3.3 Alloys used in this study

3.3.1 Bulk materials

The martensitic stainless steel SVM12 (also known as Super VM12) was studied both as a bulk material and as a substrate for overlay weld coatings. This steel exhibits excellent mechanical properties, such as high creep rupture strength, which are achieved through the addition of tungsten (1.50–2.50 wt%), niobium (0.02–0.10 wt%), and vanadium (0.15–0.30 wt%) [50]. These properties are further enhanced by the long-term stability of the martensitic microstructure, which is maintained by the incorporation of small amounts of boron. While martensitic steels can experience microstructural degradation at high temperatures via transformation into sub-grain microstructures and subsequent coarsening of the sub-grains, the addition of small amounts of boron to this alloy retards these degradation processes and preserves the material's integrity [51]. The martensitic microstructure of SVM12 displayed in Figure 3.1 was generated through treatment at 1100°C for 30 minutes, followed by air cooling. This was followed by a tempering treatment at 770°C for 2 hours, with a final step of air cooling to stabilise the martensitic microstructure.

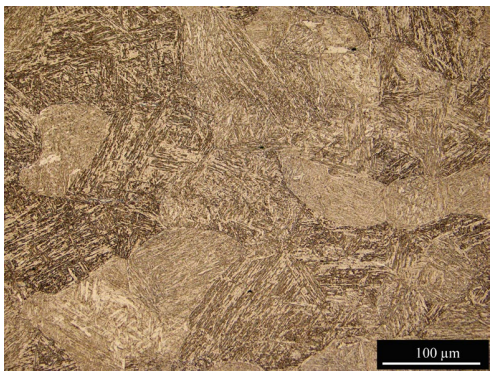

Figure 3.1: SEM image of the unexposed martensitic microstructure of the stainless steel SVM12.

The ferritic FeCrAl alloys were studied as bulk materials and overlay weld coatings, so as to compare the corrosion behaviours of these materials and assess their potential applications in harsh environments. Although the abilities of the FeCrAl alloys to form protective α-alumina scales are reduced at temperatures <900°C, it is still interesting to investigate their corrosion properties at intermediate temperatures relevant to boiler operation (around 600°C). The use of FeCrAl alloys, either as composite tubes or as overlay weld coatings, would reduce material costs compared to the nickel-based alloys that are currently being used in certain boiler sections. For a comparison of the material costs, see Figure 3.2.

The chromia-forming alloys (Alloy 27Cr33Ni3Mo and Alloy 625) were studied because they contain high concentrations of chromium, which may lead to the formation of more-protective chromium-rich scales that mitigate corrosion in harsh environments. From the mechanical perspective, these alloys contain

molybdenum, which has been shown to improve hardness, tensile strength, and elongation to failure [52,53]. Although nickel-based alloys are expensive, they are still used in many boiler parts that are exposed to conditions of severe corrosion.

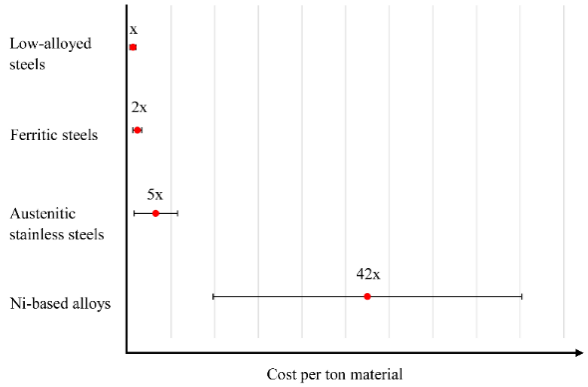

Figure 3.2: Comparison of the costs of the different material classes used as metallic boiler components. The horizontal bars indicate the range of prices within the material class. The term *'x'* is an index of price, as obtained at the time of writing of this thesis [54].

3.3.2 Coatings

In harsh environments, e.g., in biomass- and waste-fired boilers, the use of corrosion-resistant coatings offers a good alternative for mitigating corrosion, which would otherwise reduce the life-times of the metallic components of the boilers. A high-temperature corrosion-resistant coating can be applied onto a low-cost, low-alloyed steel that possesses good mechanical properties. This combination extends the life-times of the boiler components and enhances boiler performance. To be successful, a coating must exhibit good adhesion and low porosity and be compatible with the substrate. Several coating systems have been developed and applied in different parts of the boiler, including:

1. Thermal spray coatings
2. Laser-cladded coatings
3. Overlay weld coatings

The thermal spraying technique, which was first developed in 1882 [55], was demonstrated in 1937 to be an effective method to protect steel boiler tubes from high-temperature corrosion [56]. Since then, this technique has been developed and can be applied in various ways. Figure 3.3 shows the various thermal spray processes currently used to apply coatings, the most common of which are the high velocity oxygen fuel (HVOF) and high velocity air-fuel (HVAF) methods for the application of high-temperature coatings. The principle of the thermal spray technique is that the material feedstock is melted in the combustion chamber using a heat source and then accelerated towards a substrate, to which it becomes mechanically bonded. Thermal spraying has several advantages, such as a fine-coating microstructure, low porosity, and low heat input. In general, the coating thickness is in the micrometre range, although depending on the spraying technique used, it can reach a few millimetres in thickness.

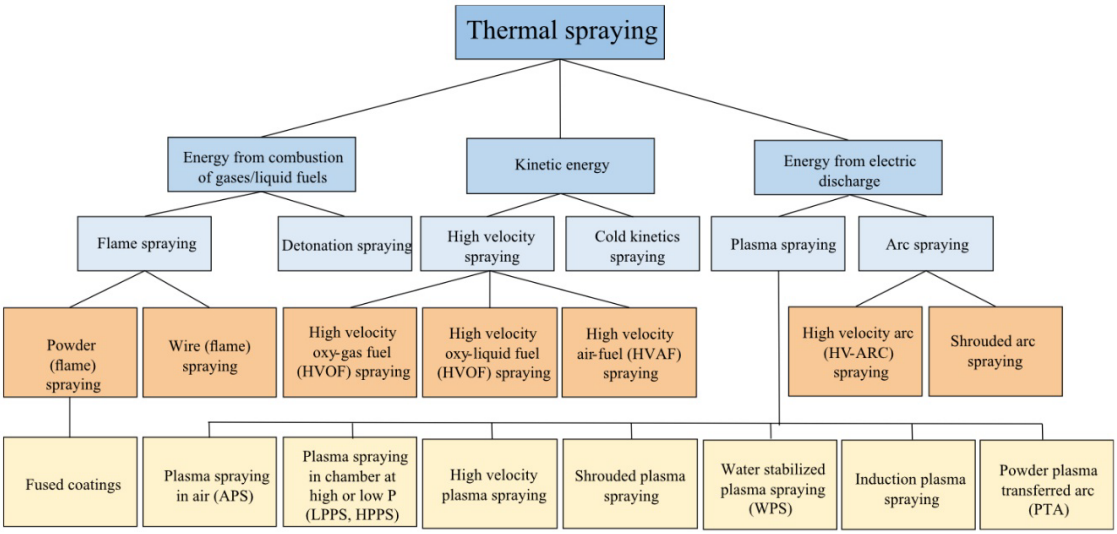

Figure 3.3: Thermal spray techniques [55]

It is worth noting that the various thermal spray techniques can lead to very different coating properties. For example, the HVAF technique produces higher-quality coatings with lower porosity than the HVOF technique, due to the low combustion temperature achieved from the air-fuel mixture and higher speed.

The laser-cladding technique uses the energy of a laser to melt the feedstock and bind it to the substrate. The microstructure of the resulting coating is characterised by low porosity and high level of adherence to the substrate, with thicknesses in the range of several micrometres to a few millimetres. Due to the high impact of the substrate during metallurgical bonding, the risk of dilution is usually high with this technique, and this may affect the mechanical properties of the coating [57].

Overlay welding is another technique that is widely used to produce high-temperature corrosion-resistant coatings. The principle of overlay welding is that a filler material is directly welded onto the substrate. This creates a layered microstructure that is thick and metallurgically bonded to the substrate. Depending on the application, the weld thickness can vary in the range of 6–50 mm. Although overlay welding provides a coating that can withstand harsh environments, dilution and an uneven surface finish can lead to accelerated corrosion of the coating [58]. For applications as boiler components (superheaters), filler materials with superior corrosion-resistance properties are used, e.g., Ni-based alloys, and the substrate possesses improved mechanical properties, e.g., high creep strength.

In this study, coatings produced through overlay welding were tested for their high-temperature corrosion resistance in a KCl-rich environment. The overlay weld coatings were produced using a mech-MIG welding machine with Pulse Multi Control and applying the technique of Fronius, with built-in arc control. The wire (filler material) was melted and re-solidified on the substrate in a single layer, which resulted in coatings with uneven surfaces and with total thicknesses of approximately 7.5–8.5 mm (as shown in Figure 3.4).

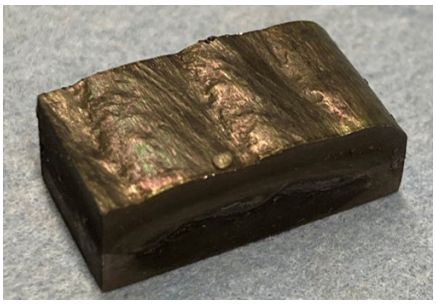

Figure 3.4: A photograph of the as-received overlay weld coating.

4 High-temperature corrosion of metals

The high-temperature corrosion (HTC) process involves a chemical reaction that occurs between a metal and its surroundings. This phenomenon pertains to materials in processes that are operating at high-temperatures, such as gas turbines, heating elements, boilers, and mineral processing plants. In general, most metals are thermodynamically unstable and will undergo reactions during high-temperature corrosion processes such as carburisation, sulphidation, nitridation, and oxidation, leading to the formation of solid reaction products, i.e., corrosion products [44]. In this thesis, the focus is on the high-temperature oxidation of metals.

4.1 Oxidation of metals

The process of metal oxidation is of great interest for the design and development of corrosion-resistant materials for applications in harsh environments. Oxidation is the reaction between a metal and oxygen, involving the transfer of electrons from the metal to oxygen which leads to the formation of a metal oxide. A general reaction can be represented as:

$$2M + O_2 \rightarrow 2MO \tag{4.1}$$

where M is the metal, O is oxygen, and MO is the resulting metal oxide.

The spontaneous occurrence of the reaction [Eq. (4.1)] is governed by the thermodynamics of the system.

4.1.1 Thermodynamics

The thermodynamics of metal oxidation provide insights into the energies and spontaneity of the oxidation reactions. The thermodynamic feasibility of an oxidation reaction is dictated by the change in Gibbs free energy (ΔG), given by the equation [Eq. (4.2)]. For a reaction to be spontaneous at constant temperature and pressure, the ΔG value must be negative.

$$\Delta G = \Delta H - T\Delta S \tag{4.2}$$

where ΔH is the change in enthalpy (heat content of the system), T is the temperature, and ΔS is the change in entropy (disorder).

If $\Delta G < 0$, the oxidation reaction is thermodynamically favoured and can occur spontaneously. For example, in the reaction shown in [Eq. (4.1)], the formation of metal oxide (MO) will spontaneously proceed if there is a negative ΔG value.

For every alloying element, ΔG may be calculated at different oxygen partial pressures and temperatures using equation [Eq. (4.3)].

$$\Delta G = \Delta G^{o} + RT\ln(pO_2) \quad (4.3)$$

where ΔG^{o} is the Gibbs free energy under standard conditions, R is the gas constant, T is the temperature, and pO_2 is the oxygen partial pressure. The calculated values of ΔG can be plotted against temperature for each individual oxide and represented in a graph, i.e., the Ellingham diagram, as shown in Figure 4.1. This diagram shows the stability of the various oxides. With respect to temperature and pO_2, oxides that lie closer to the top of the diagram are less stable than those that are lower down in the diagram. For example, at 600°C (green line), Al_2O_3 lies below Cr_2O_3, which means that Al_2O_3 is more thermodynamically stable than Cr_2O_3 and may form at lower pO_2.

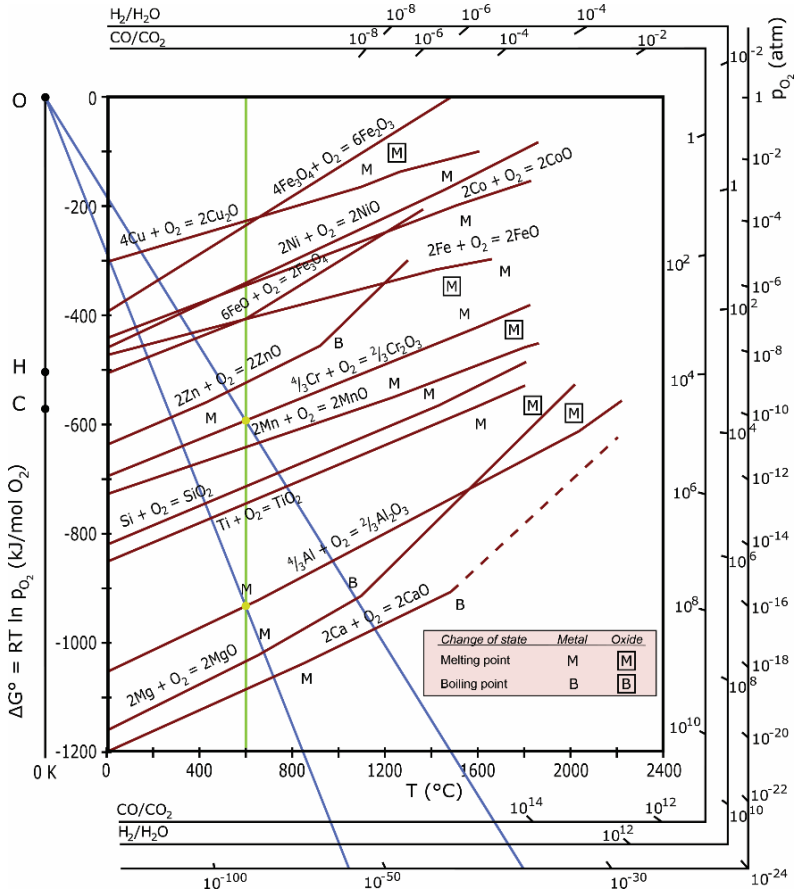

Figure 4.1: Ellingham diagram of Gibbs free energy versus temperature for some elements.

In alloy development, thermodynamic equilibrium calculations can be used to design alloys that are able to form specific oxides at a given temperature and oxygen partial pressure. In addition, equilibrium calculations are useful for understanding the forces driving the oxidation processes of coatings where inter-diffusion of alloying elements from the substrate is expected. Bigdeli et al. [59] have described new strategies for modelling the high-temperature corrosion of iron-based alloys using the Calphad Approach. In their study, different decomposition temperatures for the protective corundum structure of the sub-systems were calculated for: Fe-Al-O, Fe-Cr-O, and Cr-Al-O, see Figure 4 in [59]. However, equilibrium calculation provides only one part of the information, as information regarding the diffusion (both through the oxide and in the alloy) is needed to reach a full understanding and predict oxidation.

4.1.2 Kinetics

The kinetics of oxidation is the keystone of corrosion protection. In the case of a dense adherent scale, the kinetics concerns the mobility of species through the scale and the overall growth behaviours of the oxide scales. Already in the early 20th Century, several mechanisms were proposed to explain the processes of scale growth and transportation of species through the scale. These mechanisms have been summarised by Mott and Cabrera [60], and are illustrated in Figure 4.2.

The oxidation kinetics may be described as a linear behaviour, expressed with the linear rate equation [Eq. (4.4)]. In this case, the rate-limiting step can be a surface or a phase boundary process or a reaction, such as the adsorption of oxygen to the metal surface.

$$X = k_l * t \tag{4.4}$$

where X is the scale thickness, k_l is the linear rate constant, and t is the time.

The linear law is mostly valid for thin films and the oxidation rate is proportional to time.

However, as the scale thickness increases, the diffusion of ions through the scale becomes significant. Wagner [61] has proposed that the oxidation kinetics in thick scales is governed by the diffusion of cations and anions across the scale, resulting in a parabolic growth rate [Eq. (4.5)]. Ions diffuse through defects such as grain boundaries and dislocations, via a vacancy diffusion mechanism. This means that when a vacancy is present, an ion will jump into the vacant site and the vacancy will take the position of the ion. The ion will then jump into the next available vacancy and the process will continue. During the oxidation of an alloy, the growth of the scale follows a diffusion-controlled process that is determined by the diffusivity of the different ions through the scale.

$$X^2 = k_p * t + C \tag{4.5}$$

Where X is the scale thickness, k_p is the parabolic rate constant, t is the time, and C is the integration factor.

Wagner's model assumes that:

- The growing scale is compact and well-adherent to the metal surface;
- The rate-controlling process is the diffusion of ions and electrons through the scale;
- The thermodynamic equilibrium is established at the metal/scale and scale/gas interfaces; and
- The solubility of oxygen in the alloy is negligible.

The growth of the oxide scale may also be described using the cubic law, represented by [Eq. (4.6)]. In this case, the scale growth rate decreases faster than predicted by the parabolic kinetics. The cubic kinetics is observed in oxidation processes that involve diffusion-controlled growth of an oxide scale with additional constraints, such as the influence of microstructural changes, grain boundary diffusion, or phase transformations. Modelling studies on the effect of grain boundary diffusion on the oxidation of Ni-Cr alloys at high temperatures have demonstrated that grain boundaries in oxide scales act as diffusion short circuits, which strongly affect the oxidation kinetics [62,63].

$$X^3 = k_c * t + C \tag{4.6}$$

where X is the scale thickness, k_c is the cubic rate constant, t is time, and C is the integration factor.

Scale growth kinetics may also be governed by the logarithmic law, which states that scale growth is fast initially but decreases rapidly with time. This law applies to thin films at lower temperatures (<300°C), and the rate determining step in the reaction is suggested to be the tunnelling of electrons through the oxide scale [44]. This behaviour is represented by [Eq. (4.7)].

$$X = k_{log}(t + t_0) + C \tag{4.7}$$

where X is the scale thickness, k_{log} is the logarithmic rate constant, t is time, and C is the integration factor.

During long exposures, especially in harsh environments, the rate laws described above are not stringently followed. This is because the thick scale may experience spallation and cracking, in which case the oxidation kinetics becomes a combination of these laws. Breakaway oxidation is a phenomenon that leads to transformation of the kinetics under a given corrosion regime. During breakaway process, the scale experiences enhanced growth and transforms from a slow-growing parabolic kinetics and protective scale (primary protection) to a fast-growing kinetics and less-protective parabolic growth rate (secondary protection). Such transitions in kinetics may be explained by some combination of the laws, e.g., parabolic-cubic growth or super-/sub-parabolic growth.

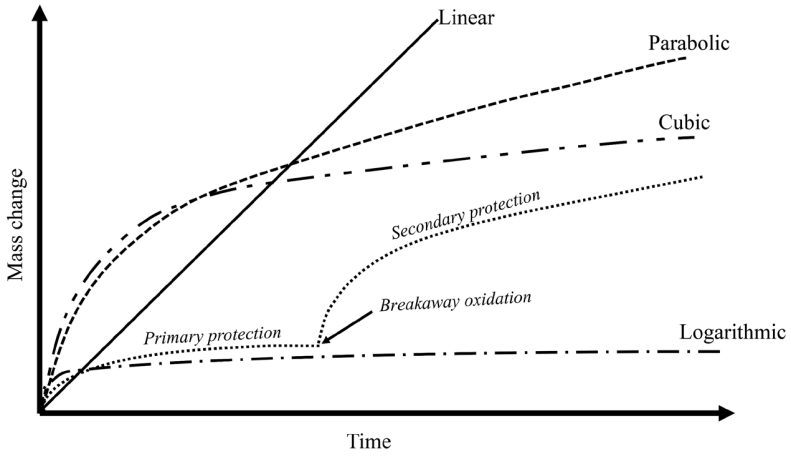

Figure 4.2: Graphical representation of the different laws applying to oxidation kinetics.

4.2 Corrosion regimes

Corrosion protection in this context refers to an oxide scale on the metal surface that acts as a barrier between the metal surface and the external environment. During oxidation/corrosion, the system may be regarded as being in different corrosion-protection modes (also known as 'corrosion regimes'), i.e., primary protection and secondary protection. These concepts were introduced by [49,64] to expand knowledge within HTC, and they have facilitated the study and simulation of the corrosion behaviours of different alloys after breakaway oxidation. These corrosion-protection modes are described further in the following sections.

4.2.1 Primary protection

High-temperature alloys rely on the formation of a protective scale to protect the alloy against further corrosion. Depending on the specific alloying elements, which include Fe, Ni, Cr, Mo, Si, and Al, an alloy can form protective oxide scales, such as chromia (Cr_2O_3) and alumina (Al_2O_3), which are adherent, thermodynamically stable and exhibit slow diffusion of ions at high-temperatures (up to about 800°C for chromia [65] and 1200°C for alumina [66]). However, for the temperature used in this thesis (600°C), stainless steels typically form mixed oxides, e.g., chromium-rich $(Fe,Cr)_2O_3$ scale and chromium/aluminium-rich $(Fe,Cr,Al)_2O_3$ scale, which exhibit similar corrosion properties as Cr_2O_3 /Al_2O_3.

The growth and protectiveness of Cr_2O_3 and Al_2O_3 scales at different temperatures and in different environments are of interest to many corrosion scientists. During exposure to O_2, the alloy undergoes transient oxidation, whereby solid solutions and simple mixed oxides are initially formed, which subsequently transform into single-phase continuous layers [67,68]. Alloys that contain high levels of chromium (e.g., stainless steels) quickly form the dense Cr_2O_3 (or a Cr-rich $(Cr,Fe)_2O_3$) scale and can sustain this scale, as there is a constant supply of chromium to the scale. However, the stability and protectiveness of the Cr_2O_3 scales are limited to temperatures <1000°C due to volatilisation to gaseous $CrO_2(OH)_2$ [69].

For alumina-forming alloys, the protective α-Al_2O_3 scale is normally formed at temperatures >900°C [70]. Below these temperatures, it is mainly the metastable alumina phases (γ-Al_2O_3, θ-Al_2O_3 and δ-Al_2O_3) that are formed [71]. These metastable alumina oxides offer lower levels of protection than α-Al_2O_3. However, in a recent study, the formation of a fast-growing and less protective α-Al_2O_3 scale on an iron aluminide coating was reported at a much lower temperature (600°C) in KCl-containing environments [72]. The authors attributed the formation of α-Al_2O_3 on the coating at such lower temperatures to hydrolysis of $AlCl_3$ generated in the corrosion process.

4.2.2 Breakaway oxidation

The Cr_2O_3 and Al_2O_3 scales remain protective within their respective temperatures ranges as long as structural stability is maintained. However, during exposure in corrosive environments, such as in biomass-fired and waste-fired boilers, these scales rapidly undergo a transformation in which the oxide composition is altered, leading to the formation of a fast-growing and less-protective scale. This type of scale transformation is known as ‘breakaway oxidation’ (separating primary and secondary regimes). Oxidation processes that involve breakaway oxidation exhibit changes in oxidation kinetics, entailing a rapid increase in mass gain, and excessive metal loss. Various explanations have been put forward in the literature for the occurrence of breakaway oxidation. One of these is the inability of the alloy to supply sufficient alloying elements, e.g., chromium, to the corrosion front so as to form and maintain the protective scale. This is evident from the rapid oxidation observed in low-alloyed steels [64], as well as chromium-evaporation from the Cr_2O_3 scale [69].

4.2.3 Secondary protection

Secondary protection, which refers to the corrosion regime after breakaway oxidation, is considered important for stainless steels at medium-high temperatures e.g., 600°C. The scales formed during this corrosion regime generate complex microstructures and normally exhibit increased oxidation kinetics. Since different elements have different affinities for oxygen and have different mobilities through the different oxide phases, the resulting scales are multi-layered as shown in Figure 4.3. These scales are often characterised by an outward-growing and an inward-growing part [20,64,73]. The interface between these layers has been interpreted as the original metal/scale interface before breakaway and is represented by a dashed line in the schematic illustration in Figure 4.3. The direction of scale growth is determined by ion diffusion through the scale, i.e., the outward-growing scale results from the outward diffusion of cations, while the inward-growing scale results from the inward-diffusion of anions.

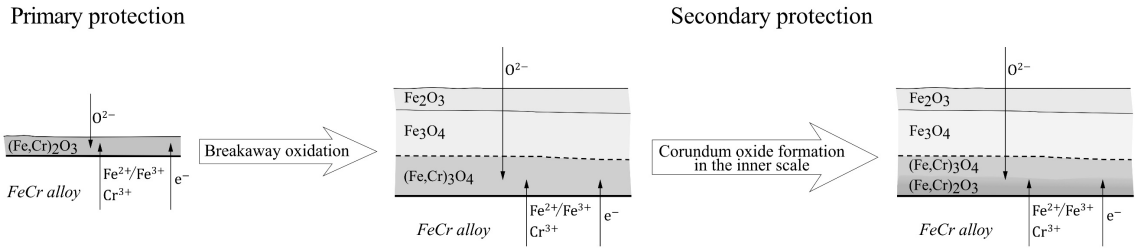

Figure 4.3: Schematic illustration of the different corrosion protection modes for a chromia-forming alloy. The different oxide layers are presented in grey level resolution.

Within the initial stages of the secondary corrosion regime, alloys have been shown to exhibit different corrosion behaviours, i.e., varying degrees of corrosion resistance [64]. The sequence of oxide formation is dictated by the thermodynamics and the different diffusion rates, with Fe-ions exhibiting faster mobility than Cr- and Al-ions [74,75]. Iron-based chromia-forming alloys form iron-rich oxides in the outward-growing scale and a chromium-rich spinel-type oxide in the inward-growing scale. Similar oxide microstructures are exhibited by the alumina-forming alloys, with the inward-growing scale forming chromium/aluminium-rich spinel-type oxide. During the course of oxidation for longer durations, these alloys may form chromium/aluminium-enriched oxides in the inner scale, which results in gradual formation of a more-protective chromium/aluminium-rich corundum-type oxide (also known as a healing layer) [64,76]. The addition of other alloying elements, such as Si, has been reported to promote the formation of a more chromium/aluminium-rich inward-growing scale that exhibits a more-protective behaviour [49,77].

The concept of secondary corrosion protection becomes more relevant for materials that are exposed to harsh conditions for long operating times at intermediate temperatures (~600°C). The oxide microstructures formed after breakaway will in this case determine the life-time of the material. This thesis contributes with insights into the long-term corrosion behaviours of high-temperature alloys in harsh environments.

4.3 Corrosion mechanisms

Several factors contribute to the oxidation process of metals, such as environment and temperature. Studies of corrosion mechanisms have traditionally focused on the initial stages of oxidation or short-term corrosion processes, i.e., within the primary corrosion regime. This thesis focuses on the corrosion behaviour after breakaway (secondary corrosion regime).

In the following sections, HTC mechanisms relevant to the combustion of biomass/waste will be described.

4.3.1 Chromate formation

In the presence of alkali-containing species, e.g., KCl, the protective scale (Cr_2O_3 or $(Cr,Fe)_2O_3$) on stainless steels is broken down according to [Eq. (4.8)] to form K_2CrO_4 and release HCl, as proposed by Pettersson et al. [8]. During this process, the scale is depleted of chromium, which impairs its protective properties. Figure 4.4 shows K_2CrO_4 particles on the surface of a stainless steel sample after exposure to a KCl-rich laboratory environment for 8000 hours. In alkali chloride-rich environments, e.g., biomass- and waste-fired boilers, alloys suffer accelerated corrosion due to continuous chromate formation which reduces the life-time of the material given that the primary protective scale is impossible to sustain. Several studies have reported the formation of chromate during alkali chloride-induced high-temperature corrosion investigations (see for example, [78,79]). The rate of K_2CrO_4 formation has been reported to be fast, occurring within hours [80–82], and the number of K_2CrO_4 particles increases in the vicinity of high concentrations of the alkali salts [82,83].

$$\frac{1}{2}Cr_2O_3(s) + 2KCl(s) + H_2O(g) + \frac{3}{4}O_2(g) \rightleftharpoons K_2CrO_4(s) + 2HCl(g) \qquad (4.8)$$

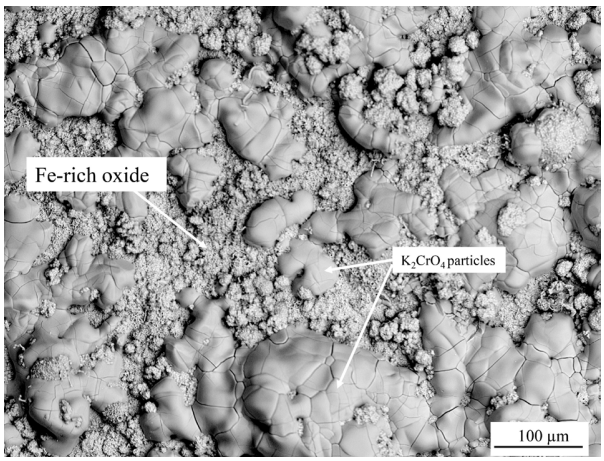

Figure 4.4: SEM-SE image showing K_2CrO_4 particles on the surface of a stainless steel sample after exposure to a KCl-rich environment.

For many stainless steels, it is the chromium-rich mixed oxide $(Fe,Cr)_2O_3$ rather than Cr_2O_3 that is destroyed via K_2CrO_4 formation according to [Eq. (4.9)], thereby forming non-protective Fe_2O_3. The breakdown of

the protective scale via chromate formation has also been reported for alloys that have been exposed to K_2CO_3, which shows that phenomenon is not limited to alkali chloride species [15,84].

$$\frac{1}{2}(Fe_{1-x}Cr_x)_2O_3(s) + 2xKCl(s) + \frac{3x}{4}O_2(g) + xH_2O(g) \rightleftharpoons xK_2CrO_4(s) + \frac{1}{2}(1-x)Fe_2O_3(s) + 2xHCl(g) \quad (4.9)$$

Since alloys suffer breakaway oxidation through chromate formation and experience rapid degradation in boiler environments, understanding the long-term corrosion properties of oxide scales formed in the post-breakaway regime, i.e., secondary corrosion regime, becomes important.

4.3.2 Chlorine-induced corrosion – chlorine cycle

Another proposed corrosion mechanism that is referred to in the boiler environment is the active oxidation mechanism (also known as the chlorine cycle), which was initially proposed by McNallan et al. [85] and further developed by Grabke [86]. This mechanism highlights the catalytic role of chlorine in the metal oxidation process. The mechanism follows three steps: initiation, propagation, and termination. In the initiation step, chlorine is proposed to be released from chlorine-containing species, e.g., through the oxidation of HCl [(Eq. 4.10)]. According to the mechanism, the formed chlorine gas is transported through the oxide scale and reacts with the alloying element, leading to the formation of volatile metal chloride at the scale-metal interface, according to [(Eq. (4.11)]. At high temperature, the vapour pressure of these metal chlorides is high, and the gaseous metal chlorides diffuse outwards. Upon reaching regions with higher oxygen partial pressures, the metal chloride is converted to its corresponding oxide, according to [(Eq. (4.13)]. This final step also leads to the release of chlorine gas, which either evaporates or is transported back to the metal-scale interface, such that the cycle repeats. In this mechanism, chlorine accelerates corrosion due to its catalytic nature, whereby it continuously recycles to form more metal chlorides that convert to oxides.

$$2HCl(g) + \frac{1}{2}O_2(g) \rightleftharpoons Cl_2(g) + H_2O(g) \quad (4.10)$$

$$M(s) + Cl_2(g) \rightleftharpoons MCl_2(s) \quad (4.11)$$

$$MCl_2(s) \rightleftharpoons MCl_2(g) \quad (4.12)$$

$$2MCl_2(g) + O_2(g) \rightleftharpoons 2MO(s) + 2Cl_2(g) \quad (4.13)$$

However, the chlorine cycle mechanism raises the question as to how only the $Cl_2(g)$ and $MeCl_x(g)$ is allowed to diffuse through the oxide scale whereas $O_2(g)$ is not. If oxygen would diffuse through the scale via the same transport paths as chlorine, i.e., pores and cracks, that would reduce the possibility of metal chloride formation at the metal/scale interface, since the oxygen partial pressure would increase across the scale. Another questionable aspect of the chlorine cycle mechanism is the fate of chlorine in an environment that is rich in water vapour, such as the biomass/waste-boiler environment. In the presence of water vapour, the reaction in [Eq. (4.10)] would be reversed and instead the reaction expressed by [Eq. (4.14)] would occur.

$$2H_2O(g) + 2Cl_2(g) \rightarrow 4HCl(g) + O_2(g) \quad (4.14)$$

For these reasons, a different mechanism based on an electrochemical process has been proposed.

4.3.3 Chlorine-induced corrosion – electrochemical approach

The electrochemical approach suggested by Folkeson et al. [87], involves a redox reaction in which molecular chlorine dissociates at the scale-gas interface to form chloride ions [Eq. (4.15)]. Simultaneously, cations are created at the metal-scale interface via oxidation [Eq. (4.16)], and this generates an electron current. In the case of biomass combustion, where there is a high HCl content, chloride ions are released via the deprotonation of HCl, according to [Eq. (4.17)], and there is reduction of oxygen at the cathode.

$$Cl_2(g) + 2e^- \rightarrow 2Cl^-(ads) \quad (4.15)$$

$$Me(s) \rightarrow Me^{n+} + ne^- \quad (4.16)$$

$$2HCl\ (ads) + \frac{1}{2}O_2\ (ads) + 2e^- \rightarrow H_2O\ (g) + 2Cl^-(ads) \quad (4.17)$$

In contrast to the active oxidation mechanism, the transport of chlorine through the scale is via Cl^-. The monovalent Cl^-, in contrast to the divalent O^{2-}, is also expected to diffuse faster through the oxide scale.

4.3.4 Chromic acid formation

Water vapour may also react with the protective chromia layer, according to [(Eq. (4.18)], leading to the formation of chromic acid $CrO_2(OH)_2$ [88]. The continuous formation and evaporation of chromic acid depletes the scale of chromium, leading to the formation of a poorly protective secondary scale. The effect of water vapour on the corrosion of metals has been investigated in many studies (see for example, [89,90]. It has been suggested that the formed chromic acid is removed from the metal surface through evaporation, which constantly shifts the equilibrium of the reaction to the right. The rate of chromium evaporation increases with temperature and gas flow [91].

$$\frac{1}{2}Cr_2O_3(s) + H_2O(g) + \frac{3}{4}O_2(g) \rightleftharpoons CrO_2(OH)_2(g) \quad (4.18)$$

The effect of water vapour on metal oxidation has also been attributed (among other suggestions) to its involvement in reactions at the metal surface that change the oxidation mechanism [83,92]. These studies suggest that $H_2O(g)$ is the main source of oxygen, and that it promotes internal oxidation of chromium in FeCr alloys.

5 Experimental procedures

The experimental activities are described in two parts: Set-up development and Corrosion tests both in the laboratory and field, as illustrated in Figure 5.1.

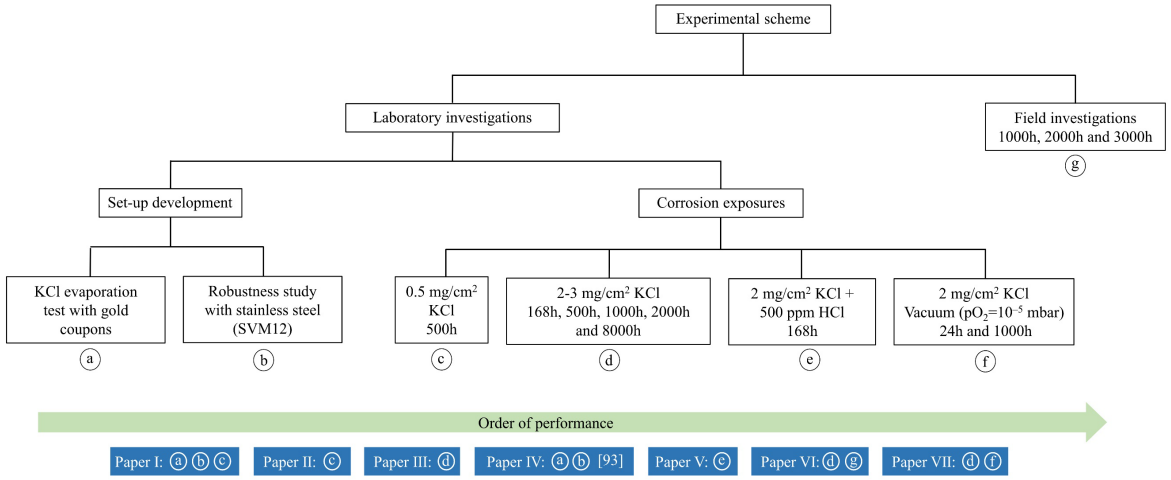

Figure 5.1: Experimental activities carried out in this thesis. The order of performance is shown by the green arrow, and the respective publications are listed in the blue-coloured panes. Addition experimental work was performed for paper IV [93].

5.1 Set-up development

5.1.1 KCl evaporation test

In this work, an experimental set-up was developed and optimised in the laboratory to minimise KCl evaporation and, thereby, enable long-term corrosion testing involving the application of salt to the sample surface at 600°C. For this purpose, KCl evaporation tests were performed using three (24-carat) gold coupons, in order to avoid surface reactions. The effect of gas flow on KCl evaporation was investigated at two gas flows: 0.1 cm/s and 0.5 cm/s. In addition, an alumina boat filled with KCl(s) was placed up-stream of the samples to saturate the incoming gas with KCl(g) before passing over the samples. Prior to exposure, the gold samples were sprayed with varying amounts of KCl (range, 0.2–0.9 mg/cm^2). The samples were then left to dry in a desiccator for 24 hours and re-weighed before exposure. The gold samples were then exposed to an environment that consisted of 5% O_2 + 20% H_2O + N_2 (Bal) in a three-heating-zone silica tube furnace (Figure 5.2). The temperature in all three heating zones was set to 600°C and calibrated using a thermocouple type K, allowing a total heating zone of about 30 cm (Figure 5.3).

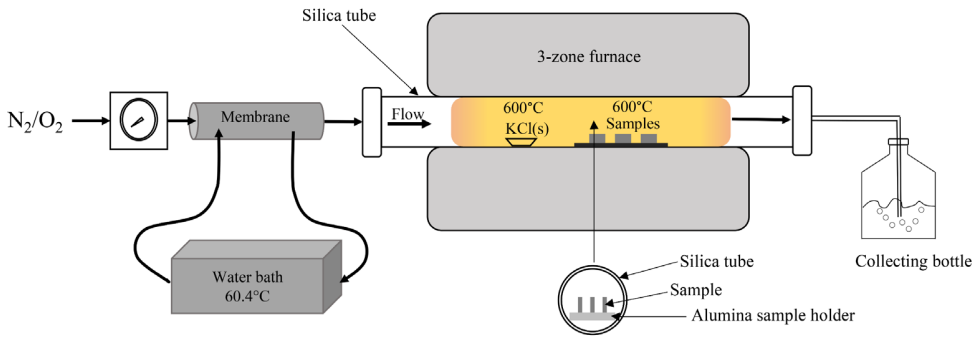

Figure 5.2: Schematic of the experimental set-up used for the investigations in this thesis.

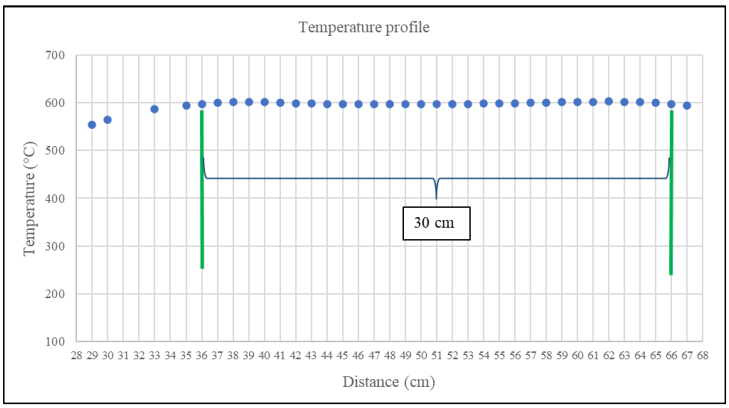

Figure 5.3: Measured temperature profile after calibration prior to the sample exposures.

5.1.2 Robustness study

In order to validate the robustness of the set-up, a 168-hour exposure was carried out using 18 coupons of the SVM12 material. The coupons were prepared by grinding the surfaces with 800-grit SiC paper and the edges with 500-grit SiC paper. The samples were then de-greased using an ultrasonic bath that contained acetone, followed by cleaning with ethanol. KCl salt was pre-deposited onto the samples by spraying a solution that consisted of 80 vol% ethanol and 20 vol% distilled water saturated with KCl. During spraying, warm air was passed over the samples to enable faster drying of the salt. Samples were weighed in between the spraying, to ensure that the desired amount of KCl was deposited. The samples were then incubated in a desiccator for 24 hours and re-weighed just before exposure.

5.2 Laboratory corrosion tests

5.2.1 Materials

The corrosion behaviours of various alumina-forming and chromia-forming alloys were investigated using the newly developed set-up described in Section 5.1. The alloys were studied as bulk, as well as overlay

weld coatings to compare their corrosion behaviours. Table 5.1 shows the chemical compositions of the tested materials. The newly developed martensitic stainless steel SVM12 was supplied by Vallourec SA and tested both as bulk material and as the substrate for the overlay weld coatings. The ferritic FeCrAl alloys were supplied by Kanthal AB. The austenitic stainless steel 27Cr33Ni3Mo and the nickel-based Alloy 625 were supplied by Alleima AB. The bulk materials were received as coupons with dimensions of 20×10×2 mm, while the overlay weld had the dimensions of 20×10×8 mm. A detailed description of how the overlay welding process was conducted can be found in Section 3.3.2.

Table 5.1: Chemical compositions of the alloys studied in this thesis.

Material	Chemical composition (wt-%)								
	Fe	**Si**	**Mn**	**Mo**	**Cr**	**Al**	**Ni**	**C**	**Others**
SVM12	Bal.	0.6	0.8	0.6	12.0		0.4	0.16	W=1.50-2.50 Co=1.50-2.50 V=0.15-0.30
Kanthal® EF101	Bal.	1.25	0.10		12.4	3.7		0.02	RE
Kanthal® EF100	Bal.	0.3	0.2		10.1	4.0	<0.5	0.02	RE
Kanthal® APMT	Bal.	0.7	0.4	3.0	21.0	5.0		0.08	RE
Alloy 27Cr33Ni3Mo	Bal.	0.8	2.0	3.0	25-31		27-36	0.1	RE
A625	4.29	0.2	0.35	9.0	21.0	0.19	63.0	0.1	RE
Fe10CrAl	Bal.				10	3			C, N, Zr
Fe15CrAlSi	Bal.	2			15	3			
Fe20CrAlSi	Bal.	2			20	3			

5.2.2 Sample preparation and furnace exposures

All the materials tested in their bulk versions were prepared according to the sample preparation procedure described in Section 5.1.2. The overlay weld coatings did not undergo any sample preparation prior to exposure. Four sets of corrosion tests, labelled *c*, *d*, *e*, and *f* in Figure 5.1, were performed in the laboratory environment by utilising the newly developed experimental set-up describe in the sub-chapter 5.1, as follows:

Laboratory corrosion test (c): 0.5 mg/cm^2 KCl was pre-deposited on the samples (both bulk materials and overlay weld coatings), which were then exposed for 500 hours at 600°C.

Laboratory corrosion test (d): 2 mg/cm^2 KCl was pre-deposited on the samples (both bulk materials and coatings) and the exposure was carried out for 168, 500, 1000, 2000, and 8000 hours at 600°C. In the case of samples exposed for up to 8000 hours, 3 mg/cm^2 KCl was pre-deposited on the samples.

Laboratory corrosion test (e): 2 mg/cm^2 KCl was pre-deposited on the samples (only bulk materials) and the exposure was carried out for 168 hours at 600°C. In addition, 500 ppm HCl was introduced into the furnace system from a gas mixture of 5% HCl-95% N_2 and was regulated using a mass flow controller.

Laboratory corrosion test (f): In this exposure, 2 mg/cm^2 KCl was pre-deposited on the samples which were inserted in 16-mm quartz tubes and evacuated up to 10^{-5} mbar. The sealed quartz capsules were then introduced into the tube furnace at 600°C and the exposure was carried out for 24 hours and 1000 hours.

All the laboratory corrosion tests were performed isothermally, and the samples were weighed before and after the exposures using a Sartorius™ scale with a resolution of 1µg.

5.3 Field corrosion tests

5.3.1 Materials

The materials investigated in the field were machined into rings with an inner diameter of 3.3 cm and a thickness of roughly 2 mm. No further sample preparation was performed on the ring samples prior to exposure (for the sample ring, see Figure 5.4 a). Four coatings from different material classes were used, namely: a marginal chromia-former (SVM12); a FeCrAl (Kanthal® APMT); a lean FeCrAl (Kanthal® EF101); and a Ni-based coating (A625) (for chemical composition, see Table 5.1).

5.3.2 Exposures

The field exposures were carried out in the superheater regions of three different commercial boilers. The tests were conducted using an air-cooled probe with two temperature zones. The temperature in these zones was controlled using thermocouples and maintained at 600°C in both zones. Figure 5.4 b shows a schematic drawing of the probe with temperature zones marked 1 & 2.

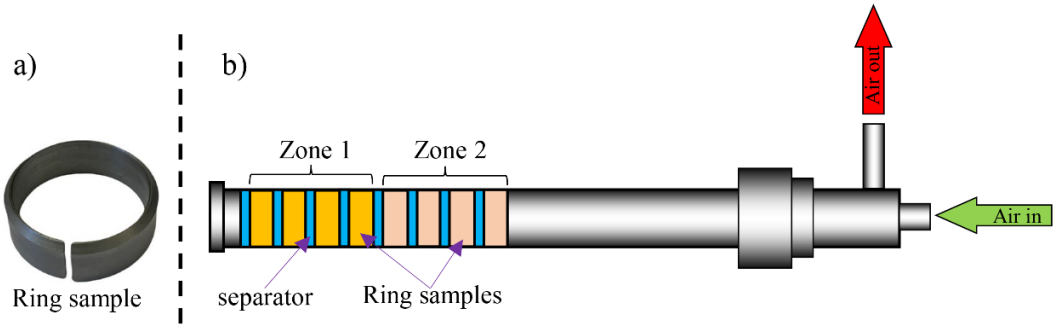

Figure 5.4: Air-cooled probe used for the field corrosion tests.

The marginal chromia-former (SVM12) and the FeCrAl (Kanthal® APMT) were exposed for 3000 hours in a bubbling fluidised bed (BFB) boiler designed for the Dalkia Facture SCA paper factory in Biganos (France). The boiler's steam production capacity is 47.15 kg/s at 10 bar(a) and the steam temperature is 520°C, with feedwater at 180°C. The solid fuel mixture designed for this boiler includes paper factory waste (bark, chips, paper mill sludge), forestry waste (treetops, branches, stumps), industrial wood waste (bark,

sawdust, chips), and municipal wood residues (municipal pruning waste and branches). Natural gas is used as the starting and support fuel.

The lean FeCrAl (Kanthal® EF101) alloy was exposed for 2000 hours in another BFB boiler (ASV06) located at the Asnaes power station in Kalundborg, Denmark. The ASV06 boiler uses wood chips as fuel and produces steam at a pressure and temperature of 100 bar and 540°C, respectively. The boiler has a nominal thermal heat input of 140 MJ/s.

The Ni-based alloy (A625) was exposed for 1,000 hours in a waste-fired grate boiler with a thermal capacity of 27 MW. It produces steam that is used for electricity production and district heating. The Line 4 of the CHP plant is located at the AffaldPlus plant in Næstved and it has a nominal capacity of 8 t/h. The steam pressure is 54 bar, and the steam temperature is 405°C.

6 Analytical techniques

A combination of analytical techniques was used in this work to characterise the corrosion products and to investigate the microstructures of the oxide scales formed on the different materials and coatings. The main working principles of the different techniques are described in the following sub-chapters.

6.1 Cross-section preparation - broad ion beam milling

Broad ion beam (BIB) milling is a powerful tool for preparing cross-sections for analysis with SEM. The milling produces wide and smooth surfaces, making it possible to observe and characterise the minute features of the sample. For this process, a sample is introduced into the chamber, fastened to a stage below a mask, which protects the sample (except the edge to be milled) from direct collision with the incoming beam, and the milling process proceeds in a vacuum. During BIB milling, ions are produced from an ion source (Ar) and accelerated towards the sample surface. As the ions interact with the sample surface, atoms are ejected from the sample surface, resulting in a smooth cross-section. Figure 6.1 illustrates the difference between an ion-milled region and a mechanically polished region of the same sample. Since the milled section is large, a representative region may be selected for further analysis. In this work, two BIB milling systems were used: the Leica EM TIC 3X for cross-section milling, operated at 8 kV; and the Gatan PECS II system for planar milling, operated at 6 kV.

Prior to ion-milling, the cross-sections are prepared by cutting the sample and polishing (up to 0.5 μm) using the Leica EM TXP target surfacing system.

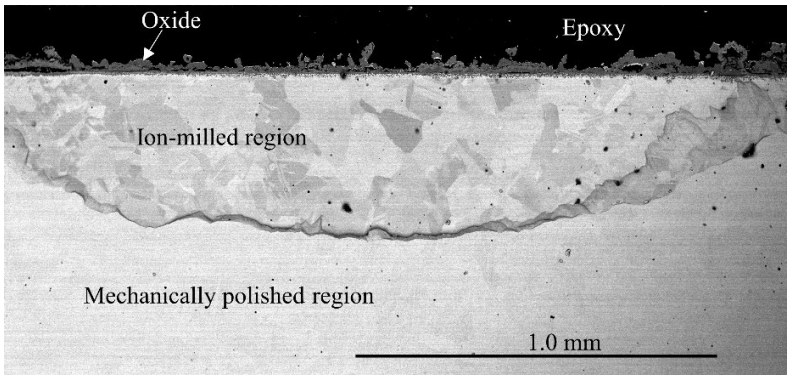

Figure 6.1: SEM-BSE cross-sectional image showing ion-milled and mechanically polished regions of the same sample.

6.2 Light optical microscopy

Light optical microscopy (LOM) utilises the ability of the lens to bend photons generated from a light source and focus it on the studied specimen. Typically, the resolution of LOM is about 200 nm, as it is limited by the wavelength of visible light [94]. In this study, LOM was used to check the sample surfaces

during specimen preparation. In addition, LOM was used to acquire low-magnification images of cross-sections of the samples after exposure, to reveal the oxide thicknesses (Figure 6.2). However, to observe smaller features, a technique with higher spatial resolution, such as scanning electron microscopy (SEM), must be used.

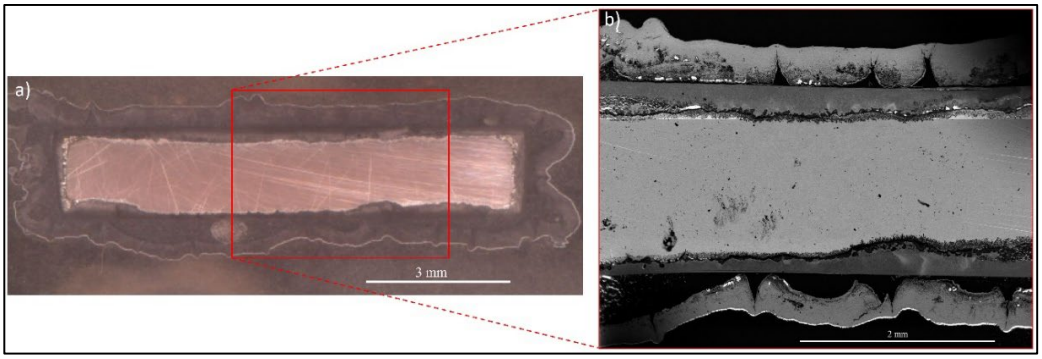

Figure 6.2: Images of the cross-section of a sample after exposure for 2000 hours. a) Low-magnification image acquired by light optical microscopy, revealing the entire oxide scale. b) High-magnification SEM-BSE image, revealing detailed features of the scale.

6.3 Scanning electron microscopy

For more-detailed characterisations of corrosion products, scanning electron microscopy (SEM) was used. SEM, which uses electrons to create an image with high spatial resolution, can be used for several purposes, for example, to acquire information about the morphology, topology, chemical composition, and crystallographic structure. A schematic of the SEM instrument is presented in Figure 6.3. The working principle of SEM is that electrons are generated by an electron source (electron gun) at the top and are accelerated to energies in the range of 0.1–30 keV. A system of electro-magnetic lenses converges the electron beam into a narrow probe. The focused beam is then swept across the sample using scanning coils, thereby generating signals that can be converted into images by the detectors [95].

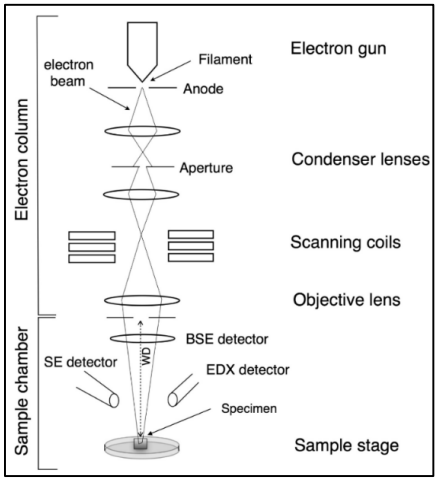

Figure 6.3: Schematic of a scanning electron microscope, showing the different components and optics [95].

Once the electrons interact with the sample, several types of signals are generated. In this work, three signals have been used: a) secondary electrons; b) back-scattered electrons; and c) characteristic x-rays. The magnitude of each signal generated delivers information about the material, which in turn depends on several other factors, such as the accelerating voltage, type of material, and angle of incidence. Different signals originate from the sample from different depths, as shown in Figure 6.4. A higher accelerating voltage results in a larger interaction volume and reduced spatial resolution.

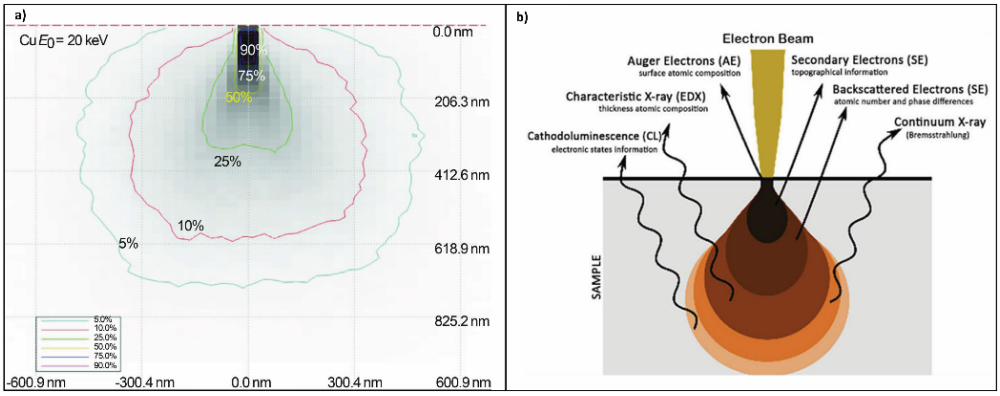

Figure 6.4: Interaction volume depicting the energy disposition when the electron beam of the SEM interacts with the sample surface. a) Based on a CASINO Monte Carlo simulation and reported by [95]. b) The different signals emitted within the interaction volume.

Secondary electrons

Secondary electrons (SE) are low-energy electrons (<50 eV) that are emitted when the incident beam inelastically interacts with the sample surface. The SEs can only escape from regions that are close to the surface, which makes them surface-sensitive. As the electron beam scans across the surface, more SEs are emitted from high-angled areas of the object, giving rise to an edge effect. This enhanced SE escape along the edges can be utilised to generate information about the topography of the sample.

Back-scattered electrons

Back-scattered electrons (BSE) are generated from a larger interaction volume, due to the higher energy of the electron generated by elastic interactions of electrons with the nuclei of the atoms in the sample. Atoms with higher atomic numbers or denser regions generate more scattered electrons. During imaging with the BSE detector, regions that contain elements with high atomic numbers/denser regions will, therefore, appear brighter. This principle can be exploited to acquire information about the composition of the sample. Furthermore, electron channelling contrast imaging (ECCI) in SEM may be utilised to obtain the crystallographic orientations in the sample. The principle behind ECCI is that when the crystal lattice is oriented appropriately in relation to the electron beam, electrons channel through the lattice planes, causing varying intensities of the back-scattered electrons [96]. The images produced reveal structural features such as grain boundaries/orientations (see example in Figure 6.5). In this thesis, the images acquired using ECCI were used to measure the oxide grain sizes.

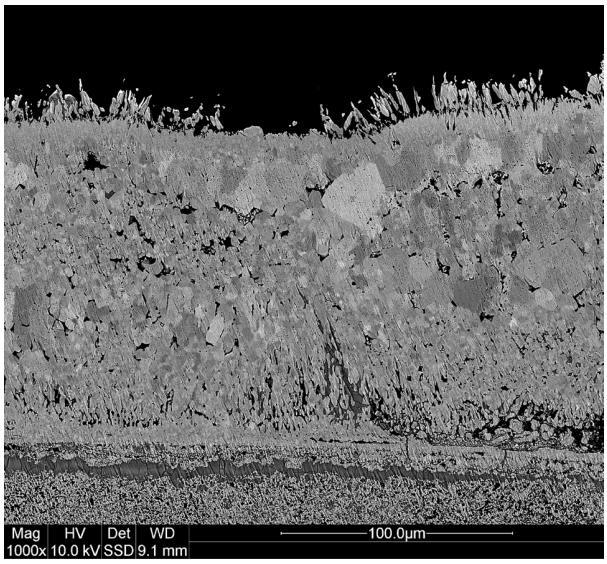

Figure 6.5 SEM-BSE image showing the different grains in the oxide.

The FEI Quanta 200 Environmental Scanning Electron Microscope (ESEM) equipped with energy-dispersive x-ray (EDX) detector was used to characterise the corrosion products. The accelerating voltage was in the range of 8.5–12 kV for imaging with the BSE detector and 20 kV for the chemical analyses. Prior to imaging, the samples were cut using a Leica EM TXP instrument and cross-sections were prepared using the Gatan PECS II BIB milling system.

Characteristic X-rays

X-rays escape from deeper regions within the interaction volume (Figure 6.4b). When high-energy primary electrons interact with the inner shells of the atom, electrons are ejected from their original shells, leaving the atom in an excited state with a missing inner shell electron. Upon relaxation, an electron from the outer shell fills the vacant electron position and energy is emitted in the process. The emitted energy is characteristic for the atom involved in the process and gives information about the nature of the element. X-rays are used for both qualitative analyses, i.e., elemental mapping, and quantitative analyses, i.e., to uncover the elemental content of the sample. The precision of measurement may be influenced by the number of x-ray counts detected. Higher count rates and longer acquisition times reduce statistical noise, which is important for obtaining more-precise and reliable measurements. Besides, one of the challenges in energy-dispersive x-ray (EDX) spectroscopy is the overlap of characteristic x-ray peaks in the spectrum. This overlap occurs when x-ray peaks from two or more elements are close in energy and cannot be easily distinguished, which can compromise the accuracy and precision of the elemental identification and quantification. For example, sulphur (S Kα) and molybdenum (Mo Lα) have overlapping peaks at ~2.30 keV. To mitigate the effects of overlap, several strategies can be deployed, e.g., using high-resolution detectors that can better separate the closely spaced peaks, or using reference standards with known compositions to help distinguish between overlapping elements by providing a benchmark for the peak intensities and positions.

6.4 Electron back-scatter diffraction

Electron back-scatter diffraction (EBSD) is an SEM-based technique that allows the collection of crystallographic information from the sample. In this work, EBSD was used to identify the crystalline phases within the oxide scales and the bulk. The EBSD technique utilises electron channelling contrast imaging with the EBSD detector. The working principle is that the electron beam interacts with a tilted sample (~70°) and is diffracted by lattice planes at different depths within the sample. Depending on the orientations of the lattice planes, BSEs of varying intensity are detected and captured as images with different grey-scale levels using a CCD camera. The diffraction patterns from the lattice planes of the crystal are represented as Kikuchi bands on a phosphor screen. A schematic of the EBSD set-up is shown in Figure 6.6a. The arrangement of the Kikuchi bands in the EBSD pattern is a geometric representation of the orientation of the lattice planes within the crystal, which means that they can be used to obtain crystallographic information about the material, e.g., phases. An example of indexed Kikuchi bands for the hematite crystal structure is shown in Figure 6.6b. Phase identification in the present work was performed using the TESCAN GAIA3 dual-beam instrument operated at 20 kV on ion-milled cross-sections.

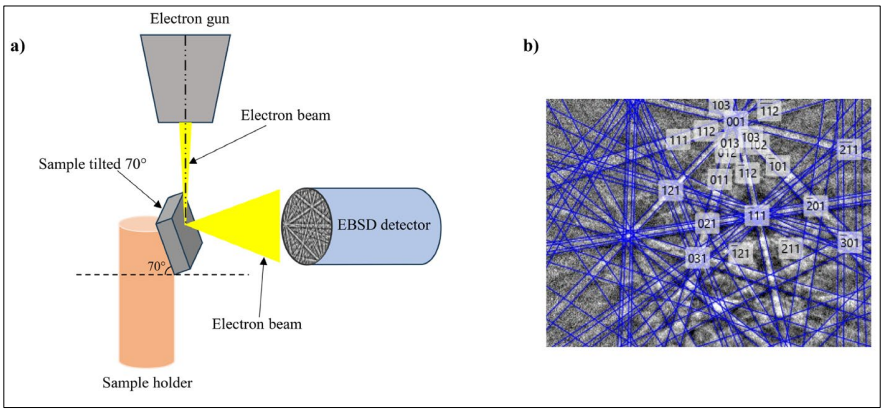

Figure 6.6: a) Schematic of the EBSD set-up. b) Kikuchi bands of indexed hematite phase.

6.5 Transmission electron microscopy

Transmission electron microscopy (TEM) offers very high resolution and can be used for the imaging and chemical analysis of various materials. The principle of scanning TEM (STEM) is similar to that of SEM in that electromagnetic lenses are used to focus an electron beam onto a sample surface. In contrast to SEM, the samples to be analysed by STEM must be very thin (<100 nm) [97]. The TEM is operated with high-energy electrons (about 80–300 keV) that pass through the sample. For this study, the TEM analysis was performed by Dr. Imran Hanif. The FEI Titan 80–300 STEM equipped with the field emission gun, an Oxford X-sight EDX detector, and a high-angle annular dark field (HAADF) detector was used. The instrument was operated at 300 keV. Prior to the analysis with STEM, the samples were prepared using a dual-beam Versa 3D Focused Ion Beam (FIB) milling machine to produce thin lamellae. A detailed description of the FIB sample preparation can be found elsewhere [11].

6.6 X-ray diffraction

X-ray diffraction (XRD) is a quantitative and qualitative analytical technique that is used to acquire structural information about a material, such as the crystalline phases and degree of crystallinity. The XRD technique is based on constructive interference of an x-ray beam with the crystalline material. The principle of XRD is that poly-chromatic x-rays produced in a cathode tube are filtered to obtain a mono-chromatic beam, which then interacts with the lattice planes of the crystalline material. This interaction leads to elastic scattering of the x-ray beam, which upon constructive interference creates a diffraction pattern that can be displayed in a diffractogram. The core principle of XRD is Bragg's law, which explains how constructive interference occurs when x-rays are scattered by a crystalline lattice, as given by [(Eq. 6.1)].

$$n\lambda=2d\sin\theta \qquad (6.1)$$

where:

n is an integer (order of diffraction),

λ is the wavelength of the incident x-rays,

d is the spacing between crystal planes, and

θ is the angle of incidence of the x-ray beam.

Constructive interference leads to observable diffraction patterns when this condition is met.

In this thesis, the Bruker D8 Discover diffractometer was used with a Mo radiation source. The Mo radiation source was selected so as to produce more-intense radiation, so as to achieve greater penetration of the thick oxide scales formed by the alloys during long exposures.

6.7 Average grain size measurement

The average grain sizes of the oxides formed by the alloys were obtained from SEM-BSE cross-sectional images of milled samples using the average grain intercept (AGI) method described in the ASTM E112-12 standard [98]. In this method, several test lines are drawn over a region of interest, and the number of intersections between the lines and the grain boundaries is noted. For example, in Figure 6.7, Line 1 intersects the grain boundaries seven times (green dots). A similar procedure is performed for all the lines.

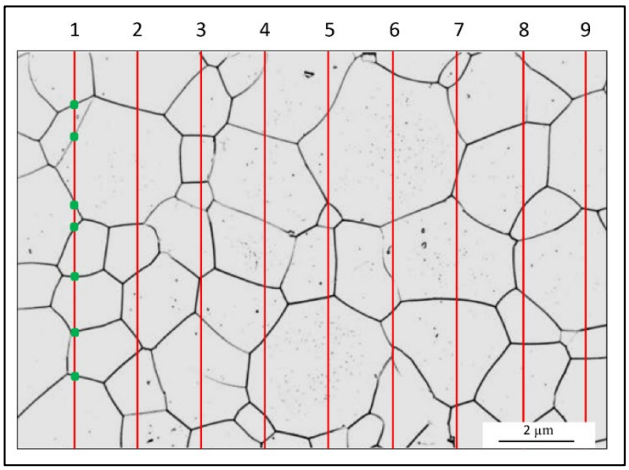

Figure 6.7: The intersect method used for determining the average grain sizes for oxides and steels.

The average grain size (N) is determined by calculating the ratio of the intercepts to line length using the equation [(Eq. 6.2)]:

$$N = \frac{n * p}{\sum x - 1} \qquad (6.2)$$

where *n* is the number of lines, *p* is the length of the test line, and *x* is the number of intersects.

It should be noted that although parallel vertical lines were used for this purpose in this work, randomly oriented test lines may also be used to obtain grain size. The choice of orientation of the test lines depends on the anisotropy of the grains, i.e., the degree of grain elongation. In general, parallel test lines are preferable for equiaxed grains, while randomly oriented test lines are preferable for elongated grains (to reduce grain anisotropy effects).

6.8 Computational modelling and simulation

Thermodynamic equilibrium calculations were performed using the Thermo-Calc 2023a software with the oxide database TCOX12, to calculate the stable oxide phases formed by the different alloys. The fraction of stable phases was plotted against the oxygen partial pressure. For the kinetic simulation, the Dictra software in Thermo-Calc was used. The calculations and simulations were performed by Dr. Sedigheh Bigdeli.

7 Results and Discussion

The aim of this thesis is to develop and utilise long-term laboratory corrosion mechanisms in order to understand and predict the corrosion of materials and coatings used for applications in biomass- and waste-fired boilers. For this purpose, a well-controlled long-term corrosion test set-up was developed, and the corrosion behaviour/mechanisms of several chromia- and alumina-forming alloys were investigated under laboratory conditions and in commercial boilers. As mentioned in the *Introduction* section, stainless superheater steels are expected to undergo breakaway corrosion, whereby the primary protection $(Fe,Cr)_2O_3$ is quickly transformed into secondary protection, i.e., fast-growing and less-protective Fe-rich oxides. In order to understand the long-term corrosion properties of materials, a combination of well-controlled long-term laboratory exposures and field investigations is necessary.

In this chapter, the results of the corrosion investigations will be discussed in two sections. The first section is concerned with the development of the experimental set-up used for the laboratory corrosion investigations, as well as with the initial set-up tests with a stainless steel SVM12. In the second section, the results of the corrosion investigations are discussed. The focus is on the long-term corrosion behaviours of the FeCr(Ni), NiCr and FeCrAl(Si) alloys, the mechanisms driving the corrosion, the influence of alloy microstructure, and the impact of increased chlorine load on the oxide scales formed after breakaway corrosion. In addition, the results of the laboratory corrosion investigations are utilised to understand and predict the progress of alloy corrosion in boiler environments.

The focus of the research is on the following research questions:

> **Research question 1.** What are the mechanisms that control the formation of good/poor secondary protection on FeCr(Ni), NiCr and FeCrAl(Si) alloys during long-term laboratory exposures to KCl at 600°C?
>
> **Research question 2.** How can long-term corrosion kinetics under laboratory conditions be used to understand the mechanisms and predict oxidation behaviour in complex boiler environment?

7.1 Laboratory set-up for long-term corrosion investigations

7.1.1 Conditions to mimic the boiler environment

To study the corrosion mechanisms of alloys in complex boiler environments, it is necessary to design an experimental procedure that mimics the key corrosive species in the boiler environment at a relevant temperature. In this work, the focus material temperature is 600°C, i.e., in the expected material temperature range for state-of-the-art biomass-fired boilers with 560°C/300 bars steam data (e.g., the wood pellet fired boiler at Avedøre power plant, Unit 2). Regarding the chemical environment, various studies have shown

that alkali chloride species (particularly KCl), HCl and H_2O are key species for accelerating the high-temperature corrosion of superheater steels in commercial boilers. These species induce breakaway corrosion, leading to accelerated corrosion and a rapid scale transition to the secondary protection. The breakaway corrosion mechanisms are described in detail in Section 4.3. However, the impact on the progression of secondary protection is less known. Thus, the investigations in this thesis were carried out at 600°C in the presence of 5% O_2 + 20% H_2O + N_2 (Bal) + KCl(s)/KCl(g), while the impact of adding HCl was investigated in **Paper V**. To investigate the influence of KCl(s) on the secondary corrosion protection at 600°C for an extended period, KCl(s) needs to be present at the sample surface throughout the exposure period. The different techniques used for applying KCl(s) to the samples' surfaces are described in **Paper I**. The high evaporation rate of KCl(s) at 600°C is a known challenge associated with investigations of KCl-induced corrosion [99], which explains why most previous studies investigating KCl-induced corrosion have involved short-term exposures [9,76,87,100,101]. To address this challenge, a set-up was developed that involved pre-deposition of KCl(s) onto the samples before exposure, together with a low gas flow rate, and placing a KCl(s) source upstream of the samples, so as to minimise the evaporation rate of KCl from the sample surfaces. These various parameters of the set-up were investigated and validated using gold coupons and are documented in **Paper I** and in the Licentiate thesis [102].

7.1.2 Robustness of the set-up

In order to achieve long-term exposures for a large material matrix, the set-up needs to limit KCl evaporation from the sample surfaces and also enable exposure of multiple samples without the risk of sample position-dependent results. KCl evaporation may limit the number of samples in each exposure, as a well-controlled gas flow rate must be maintained while the samples are placed in parallel positions (see Figure 5.2). Thus, the position-dependence of the experimental set-up was investigated by exposing 18 samples of the stainless steel (SVM12) to 5% O_2 + 20% H_2O + N_2 (Bal) + KCl(s)/KCl(g) for 168 hours at 600°C. Gravimetric analysis revealed that all the SVM12 samples exhibited mass gains in the range of 4.7–6.8 mg/cm^2, with an average mass gain of 6.1 mg/cm^2 and a spread of ±0.7 mg/cm^2 (Figure 7.1). The spread in mass gain data can be attributed to the occurrence of oxide spallation for certain samples as they cooled following the exposure. The phenomenon of scale spallation on alloys exposed to a KCl-containing environment has previously been reported [103]. The variation observed among the non-spalled samples in the present set-up is considered to be natural variability and is within the expected range. Thus, regardless of sample position, all the samples exposed in this set-up experienced a similar corrosion attack. The high mass gain indicated that breakaway oxidation had been induced and that the alloy had transitioned into the secondary corrosion regime as excepted. The presence of KCl(s) throughout the exposure period was confirmed by SEM/EDX during the post-exposure analysis (see Figure 7.2). The new set-up forms the foundation for longer exposures.

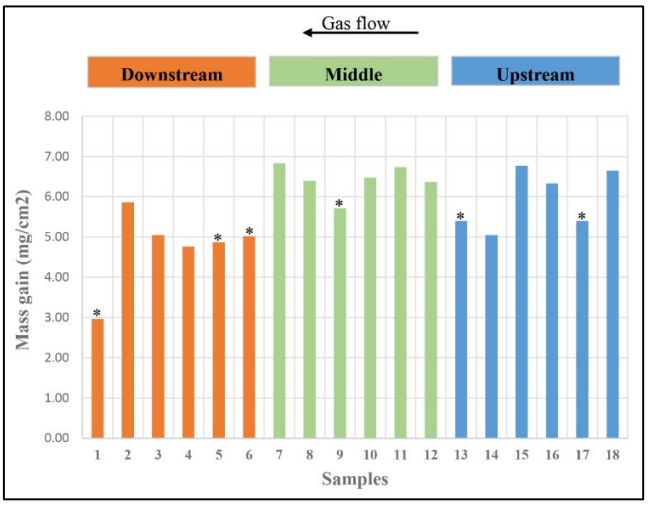

Figure 7.1: Mass gains for 18 samples of SVM12 after exposure to 5% O_2 + 20% H_2O + N_2 (Bal) + KCl(s)/KCl(g) for 168 hours at 600°C. The asterisks (*) indicate samples that experienced spallation.

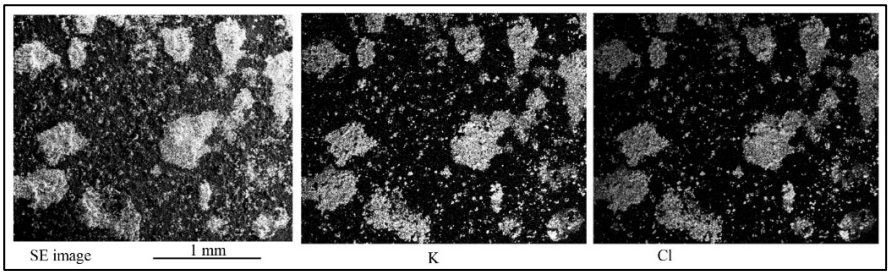

Figure 7.2: SEM image showing the presence of unreacted KCl particles on SVM12 sample, after exposure to 5% O_2 + 20% H_2O + N_2 (Bal) + KCl(s)/KCl(g) for 168 hours at 600°C.

7.2 Long-term alkali chloride-induced high-temperature corrosion

This section discusses investigations of the secondary protection of several alloys in the presence of KCl for 500 hours of exposure. The results were obtained utilising the experimental set-up introduced in Section 7.1 and are connected to Research question 1.

> **Research question 1:** What are the mechanisms that control the formation of good/poor secondary protection on FeCr(Ni), NiCr and FeCrAl(Si) alloys during long-term laboratory exposures to KCl at 600°C?

7.2.1 Corrosion behaviours, mechanisms and alloy microstructures

The FeCr, NiCr and FeCrAl alloys included both bulk materials and coatings of similar composition. In each case, 0.5 mg/cm^2 KCl(s) was pre-deposited on the samples before exposure to 5% O_2 + 20% H_2O + N_2 (Bal) + KCl(s)/KCl(g) at 600°C for 500 hours. The results of this investigation are documented in **Papers I** and **II.**

The extent of the corrosion attack in the presence of KCl(s) for 500 hours was evaluated based on the average oxide thickness and microstructure. Oxide thicknesses were measured on large ion-milled SEM-BSE cross-sectional images using ImageJ software. Several measurements were obtained from representative regions that lacked signs of spallation, and the average values were calculated, as presented in Figure 7.3. The variation in thickness across the region is presented as a range. Oxide thickness was selected because it depicts the actual extent of the corrosion attack, in contrast to mass gain measurements, which reflect the general corrosion behaviour of the material.

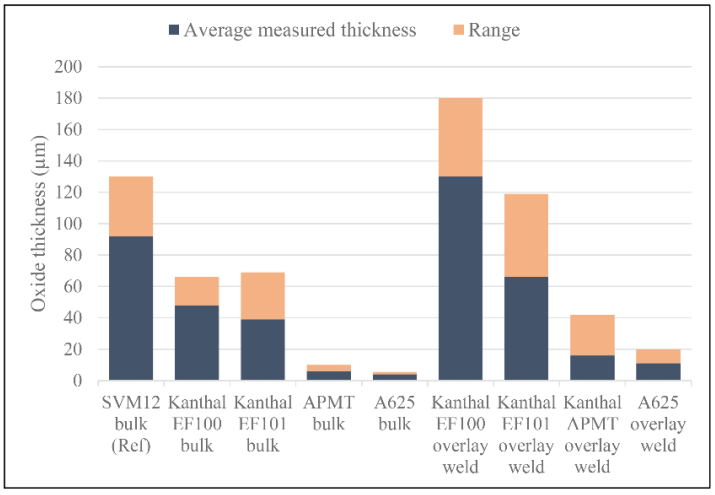

Figure 7.3: Oxide thicknesses of the bulk materials and overlay weld coatings after exposure for 500 hours to 5% O_2 + 20% H_2O + N_2 (Bal) + KCl(s)/KCl(g) at 600°C.

All the cross-sections were investigated in detail using SEM, and the crystalline corrosion products were characterised with XRD. Figure 7.4 shows the SEM-BSE cross-sectional image of the corrosion attack on the un-coated SVM12 sample, displaying the microstructure. The oxide scale can be divided into an outward-growing layer composed of iron-rich oxide and an inward-growing layer composed of a mixed spinel oxide, indicating ion diffusion-controlled scale growth. Similar oxide microstructures have been reported for short-term exposures in previous studies (see, for example [22,104]). At the surface of the sample, un-reacted KCl particles are visible. The scale contains cracks, which are attributed to the sample preparation. This is based on the observation that the oxide scale thickness remains largely uniform throughout the sample. If the cracks had formed during the exposure, the alloy would have been subjected to accelerated corrosion in the areas surrounding the cracks.

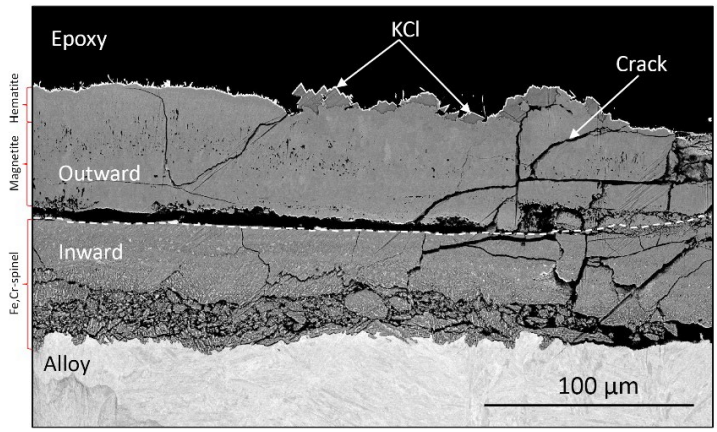

Figure 7.4: SEM-BSE cross-sectional image of SVM12 after exposure to 5% O_2 + 20% H_2O + N_2 (Bal) + KCl(s)/KCl(g) for 500 hours at 600°C.

The microstructural investigation revealed that all the alloys experienced a similar type of corrosion attack, resulting in the formation of outward- and inward-growing oxide scales (Figure 7.5). However, from the oxide thickness measurements and microstructural analyses, it is clear that the corrosion performances of the various alloys are influenced by the alloying elements and bulk/coating microstructures. From the SEM/EDX results, it can be concluded that enrichment of chromium/aluminium in the inner scale improves the corrosion resistance of certain alloys. Based on corrosion resistance, the investigated materials could be ranked (with increasing corrosion resistance) as follows: Kanthal® EF100 < Kanthal® EF100 < Kanthal® EF101 < APMT < A625. In this environment, Kanthal® EF100 fails to form a protective chromium/aluminium-rich inner scale and suffers accelerated corrosion, as evidenced by the measured oxide thickness. Besides, the overlay weld coating Kanthal® EF100 suffers a severe grain boundary attack, which reaches a depth of 75–108 µm. The good secondary protection exhibited by A625 is attributed to chromium enrichment of the inner scale, which may act as a barrier and prevent ions from diffusing through the scale, thereby mitigating further corrosion. Underneath the metal/scale interface, A625 forms a 4-µm-thick, fine-grain region (FGR), which may contribute fast diffusion pathways for chromium to the scale. Another key aspect is that the protective chromium-rich oxide formed in the secondary protection is separated from the KCl(s) on the surface by the iron/nickel oxide formed after breakaway.

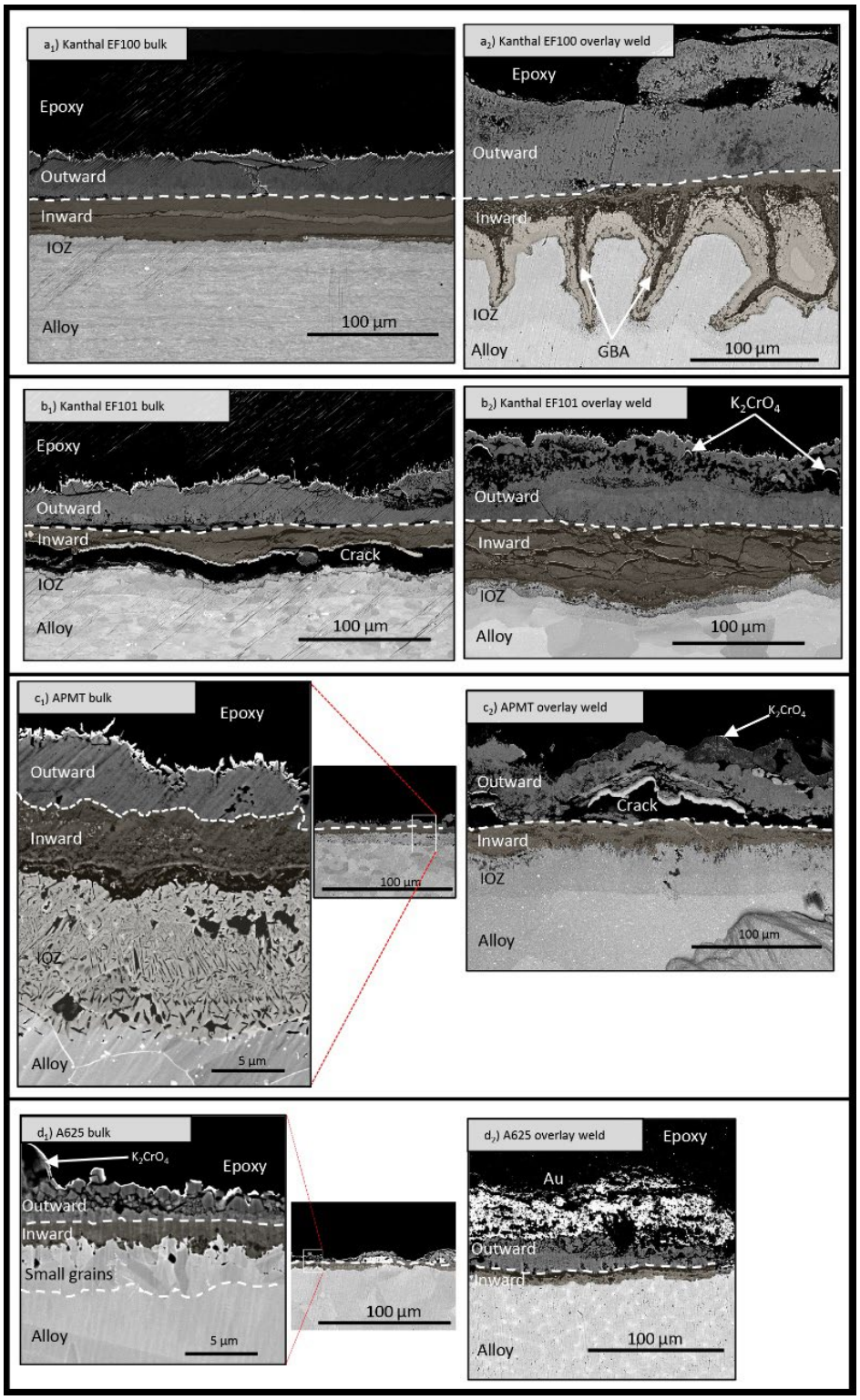

Figure 7.5: SEM-BSE cross-sectional images of the bulk materials and overlay weld coatings after exposure to 5% O_2 + 20% H_2O + N_2 (Bal) + KCl(s)/KCl(g) for 500 hours at 600°C. The samples were sprayed with 0.5 mg/cm^2 KCl prior to exposure.

It should be noted that the corrosion resistance differs between the bulk materials and the overlay weld coatings of similar composition (see Figure 7.3 and Figure 7.5). To investigate why the bulk materials exhibit better corrosion resistance than the overlay weld coatings of similar composition, a detailed microstructural investigation was performed on the Kanthal® EF101 bulk material and the overlay weld coating. The results of this study are documented in **Paper II.**

The SEM analysis of the unexposed bulk and overlay weld coating of Kanthal® EF101 revealed differences in the alloy microstructures, whereas the compositions were similar. As shown in Figure 7.6, the alloy grain sizes differed between the two cases, being in the ranges of 11–40 µm (bulk) and 20–70 µm (overlay weld coating). This discrepancy is attributed to differences in the manufacturing processes.

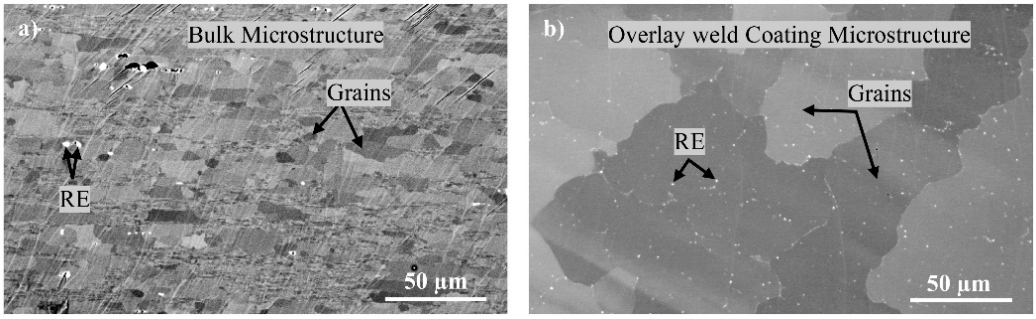

Figure 7.6: SEM-BSE images of ion-milled Kanthal® EF101 before exposure: a) bulk material; b) overlay weld coating.

Since the outward-growing, iron-rich oxides are very similar under the current experimental conditions, it was hypothesized that the corrosion resistance is influenced by the microstructure and composition of the inward-growing scale. Therefore, a detailed microstructural investigation using STEM/EDX was conducted on the complex inward-growing scales of the bulk and coated samples. The results from the TEM analysis revealed that the bulk sample formed an approximately 1-µm thick, chromium-rich oxide at the metal/scale interface accompanied by a 2-µm thick chromium-depleted zone beneath the scale (see highlighted region in the line scan in Figure 7.7). The inner scale contained a high concentration of trivalent ions (Cr and Al), exceeding 67.7% cationic ions, which represents the maximum concentration of divalent and trivalent ions in a spinel structure [105]. This indicates that the alloy has formed a slow-growing, corundum-type oxide at the metal/scale interface.

In comparison, the overlay weld coating formed a thinner, chromium-rich oxide layer (approximately 500 nm) accompanied by a 1-µm deep chromium-depletion zone, as indicated by the highlighted region in the line scan in Figure 7.7. The superior corrosion resistance displayed by the bulk material, as compared to the overlay weld coating, is attributed to the faster formation of a protective chromium-/aluminium-rich oxide layer at the metal/scale interface. The ability to form this protective scale more rapidly may be a consequence of the smaller grains in the bulk alloy, as compared to the overlay welded material (see Figure 7.6), which would facilitate rapid chromium diffusion to the scale. This is in line with earlier reports indicating that the formation of a protective scale depends on the diffusivity and activity of chromium/aluminium in the bulk [64].

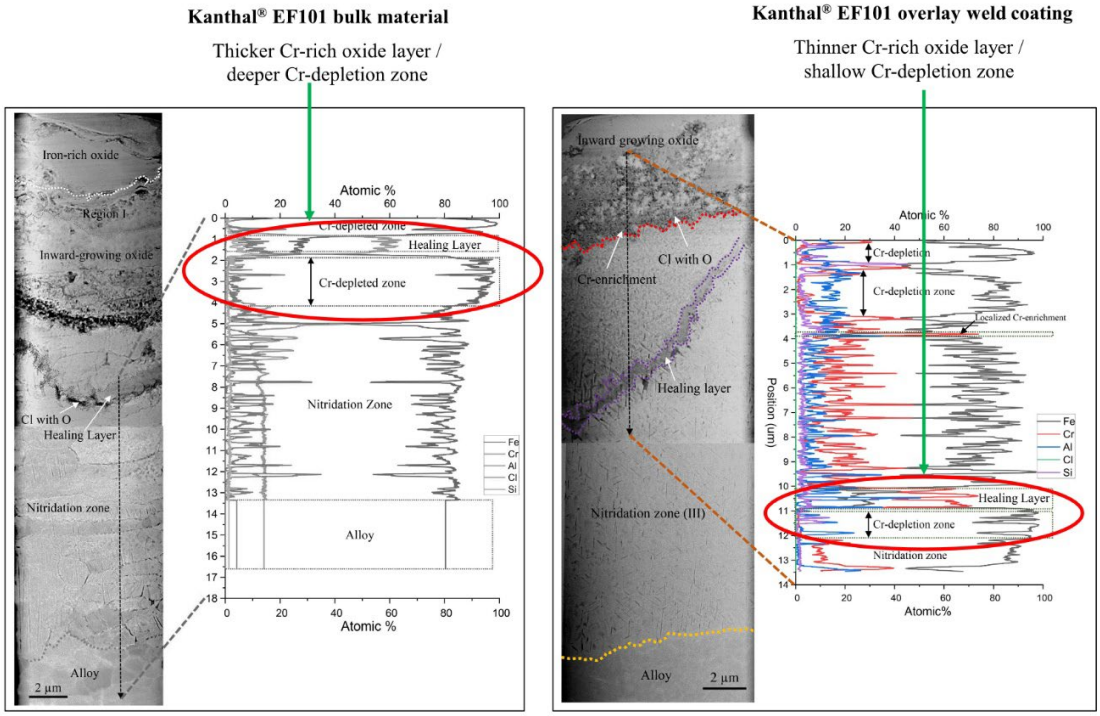

Figure 7.7: HAADF-STEM image of bulk and overlay weld coating of Kanthal® EF101 lamella, and STEM/EDX line-scan showing elemental distribution in the lower regions of the inward-growing scales.

In summary, the results from these initial corrosion investigations, together with the detailed TEM bulk/coating microstructural analysis, clearly demonstrate that the investigated alloys experience breakaway corrosion and transition to a secondary corrosion regime. Within the secondary corrosion regime, the alloys exhibit varying corrosion resistance levels linked to the alloy compositions and microstructures. However, further insights into the oxidation kinetics, the impacts of alloying elements, and the evolution of oxide scales within the secondary corrosion regime are needed to understand fully the long-term corrosion performances of these alloys in harsh environments.

7.2.2 Microstructural evolution of oxide scales within secondary corrosion regime

In this section, new insights into the long-term kinetics and evolution of oxide scales formed after breakaway in alkali chloride-rich environments will be discussed. This information makes is possible to understand which factors contribute to the formation of good/poor secondary protection. For this investigation, alloys representing different material classes that may be used for applications in harsh boiler environments were selected. Laboratory corrosion tests were performed in an environment that consisted of 5% O_2 + 20% H_2O + N_2 (Bal) + KCl(s)/KCl(g) at 600°C for 168 hours, 1000 hours and 8000 hours. Moreover, model alloys were exposed for 2,000 hours and are included in the kinetics/evolution discussion because their behaviours in a very similar environment, albeit for shorter durations (up to 168 hours), have been published previously [19,49,105]. This provides the opportunity to systematically study their oxidation kinetics, as well as the impacts of alloying elements on the secondary protection, since all of these alloys experience breakaway oxidation prior to 168 hours of exposure in this environment. For all the

exposures, 2 mg/cm^2 KCl was pre-deposited on the sample surfaces to induce breakaway oxidation and to ensure that KCl(s) was present on the surface throughout the exposure. The results of this investigation are documented in **Papers III**, **IV** and **VII**.

The oxidation kinetics results are based on the average oxide thicknesses obtained from SEM-BSE images of ion-milled cross-sections of the samples. Thickness measurements were taken from representative regions that showed no signs of spallation. Figure 7.8 shows that all the tested alloys display thicknesses that are expected to form within the secondary corrosion regime (i.e., after breakaway) already after 168 hours of exposure, as the primary protection regime is estimated to be short, as reported in for similar alloys [64]. This was also the case for the model alloys [105]. The SVM12 alloy exhibits the fastest oxidation kinetics, while alloy 27Cr33Ni3Mo exhibits the slowest oxidation kinetics of the alloys exposed for 168, 1000 and 8000 hours. These oxidation kinetics patterns clearly show that oxide scale growth after breakaway oxidation may be categorised as: fast-growing scales, representing poor secondary protection (SVM12 and Fe10CrAl); and slow-growing scales, representing good secondary protection (APMT, alloy 27Cr33Ni3M, Fe15CrAlSi and Fe20CrAlSi), in the presence of KCl(s).

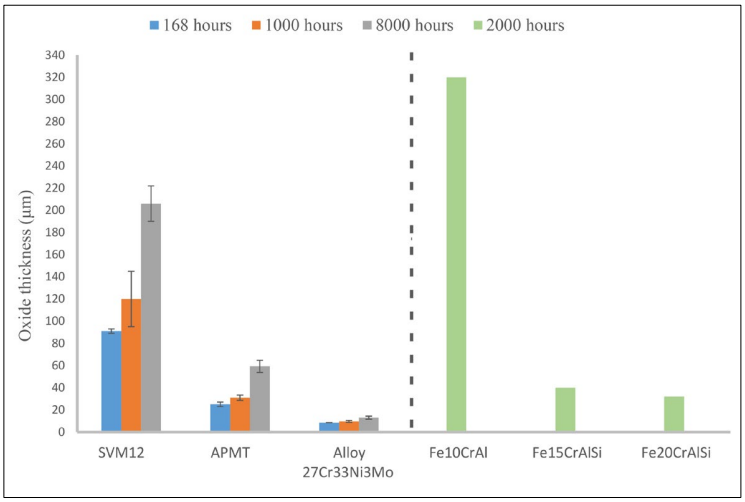

Figure 7.8: Average oxide thicknesses of the tested alloys after exposure to 5% O_2 + 20% H_2O + N_2 (Bal) + KCl(s)/KCl(g) for 168 hours, 1000 hours, 2000 hours and 8000 hours at 600°C.

To gain further insights into the protective characteristics of these oxide scales, a microstructural investigation was conducted using SEM/EDX, SEM/EBSD and XRD, and the results are discussed for each alloy below.

Martensitic stainless steel – SVM12 (Fe-12Cr)

Figure 7.9 shows that the 12-wt% Cr SVM12 alloy forms thick oxide scales, i.e., measuring 91 µm after 168 hours and about 206 µm after 8000 hours of exposure. The scales consist of outward-growing layers (region I) and inward-growing layers (region II). Potassium chromate is detected at the top of the scale and, in some cases, embedded in the outward-growing scale. The outer scales are composed of iron oxides, identified as hematite and magnetite, and the inner layers are composed of iron-chromium spinel-type oxide. The growth kinetics and dense oxide microstructures indicate a diffusion-controlled scale growth

that is enabled by the different diffusivities of cations through the spinel [74], in combination with chromate formation prior to breakaway oxidation. Very small amounts of Cl could be detected in the inner scale. After 168 hours, metal chlorides could be detected at the metal/scale interface. However, the formation of a dense oxide scale above the metal chlorides indicates that the active oxidation mechanism cannot be responsible for this scale growth. After 8000 hours, the alloy experiences low level of chromium enrichment closer to the metal/scale interface (region III). However, this chromium enrichment has no/limited impact on the scale growth rate for this alloy in this exposure time.

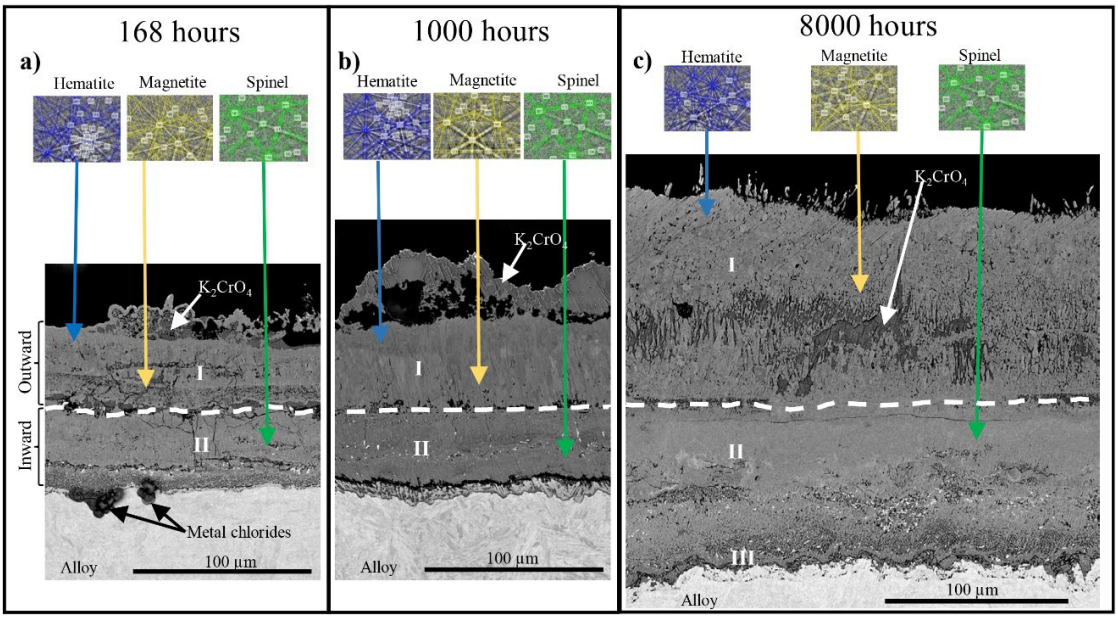

Figure 7.9: SEM-BSE cross-sectional images of SVM12, showing the evolution of the oxide microstructure after exposure to 5% O_2 + 20% H_2O + N_2 (Bal) + KCl(s)/KCl(g) for: a) 168 hours; b) 1000 hours; and c) 8000 hours at 600°C.

Ferritic FeCrAl alloy - APMT (Fe-21Cr-5Al-3Mo)

The ferritic FeCrAl alloy APMT displays slower oxidation kinetics than SVM12, and forms thin oxide scales, i.e., with thicknesses of 25 µm, 31 µm, and 59 µm after 168 hours, 1000 hours, and 8000 hours, respectively (Figure 7.10 a–c). Potassium chromate is detectable on the surface in all the exposures, and oxide microstructures consisting of iron-rich outward-growing layers (hematite on top of magnetite) and inward-growing Fe,Cr,Al spinel-type oxides are observed for all the exposed samples. Chromium and aluminium enrichment can be observed at the metal/scale interface, which over time results in formation of a corundum-type oxide, indicating the formation of a more-protective secondary protection. These oxide scale growth as well as possible phase transformation are attributed to the high chromium activity in the bulk, together with the addition of aluminium. The beneficial effects of these alloying elements have been previously reported [64,105,106]. The experimental findings for the long-term oxidation behaviour of APMT are in good agreement with the thermodynamic calculations, which predict the formation of both spinel phase and a larger fraction of the corundum phase in the regions with a lower oxygen partial pressure (see Figure 6 in **Paper III**). Underneath the scale, the alloy forms nitridation zones (NZ), as indicated by the presence of N and Al. The process of alloy nitridation may have negative consequences for both

corrosion and mechanical properties of the alloy. This is because nitridation may bind aluminium, which could otherwise be required for the re-formation of a more-protective oxide scale.

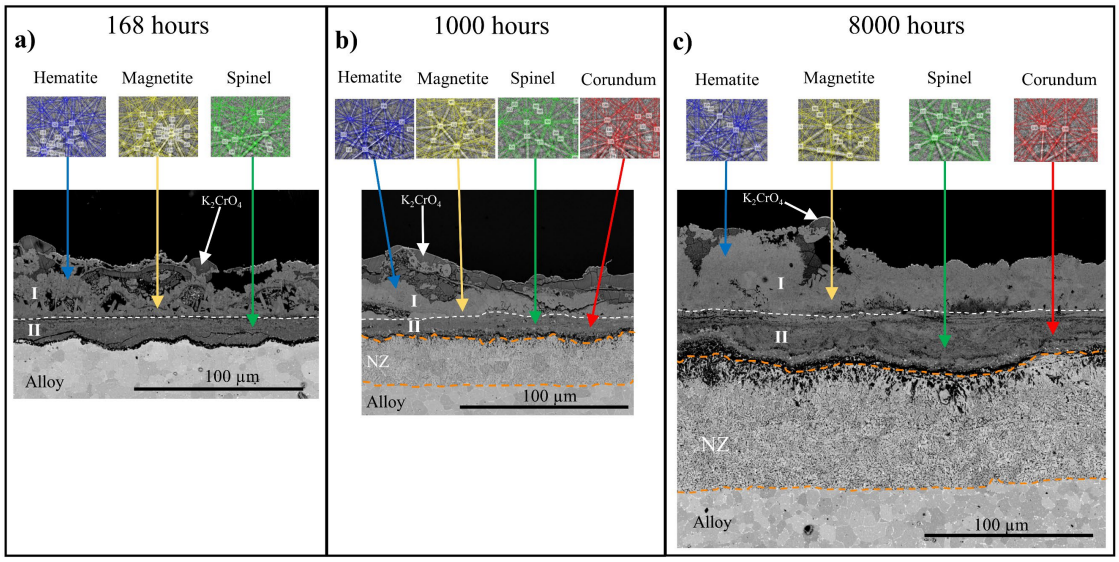

Figure 7.10: SEM-BSE cross-sectional images of APMT, showing the evolution of the oxide microstructure after exposure to 5% O_2 + 20% H_2O + N_2 (Bal) + KCl(s)/KCl(g) for: a) 168 hours; b) 1000 hours; and c) 8000 hours at 600°C.

Austenitic stainless steel - Alloy 27Cr33Ni3Mo

Alloy 27Cr33Ni3Mo exhibits the slowest oxidation kinetics and forms the thinnest oxide scales after 8000 hours of exposure, as compared with SVM12 and APMT. The oxide scale consists of an outward-growing scale and inward-growing scale (Figure 7.11), with dense oxide scales indicating a diffusion-controlled growth mechanism, in combination with chromate formation prior to breakaway oxidation. After breakaway, the scales are initially composed of an iron/nickel-rich spinel in the outer layer and a chromium-rich spinel in the inner layer. However, as the oxidation progresses, the inner scale becomes enriched with chromium, and a more-protective chromium-rich corundum-type oxide is formed. The formation of a protective chromium-rich corundum-type oxide within the secondary corrosion regime leads to the slow oxidation kinetics exhibited by this alloy after long-term exposures.

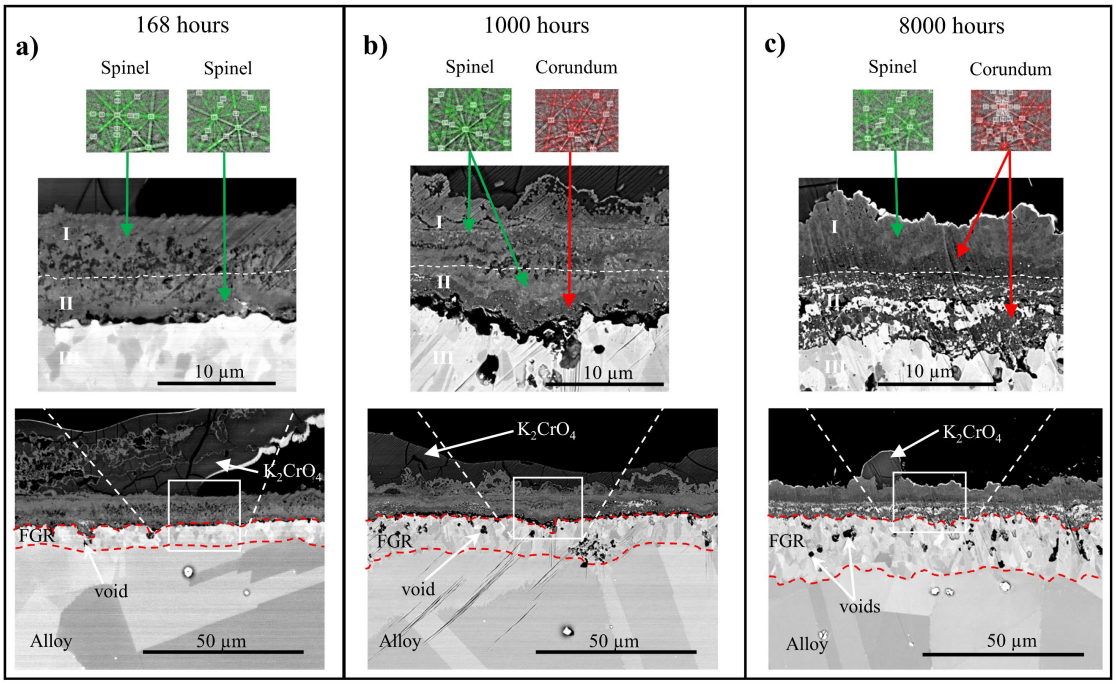

Figure 7.11: SEM-BSE cross-sectional images of Alloy 27Cr33Ni3Mo, showing the evolution of the oxide microstructure after exposure to 5% O_2 + 20% H_2O + N_2 (Bal) + KCl(s)/KCl(g) for: a) 168 hours; b) 1000 hours; and c) 8000 hours at 600°C.

The inner chromium-rich corundum-type oxide formation and possible oxide phase transformation were further investigated using DICTRA simulations of Cr_2O_3 oxide, in order to compare the formed oxide with an expected primary oxide growth [107]. Figure 7.12 shows that the corundum phase (obtained from experimental data) increases faster than the simulated Cr_2O_3 oxide scale, indicating that the fraction of corundum in the inner scale increases as oxidation progresses. This is probably due to a combination of phase transformation from the spinel oxide and formation of corundum oxide at the metal/scale interface. This type of oxide phase transformation has been reported in cases with the same experimental conditions after 2000 hours of exposure [93].

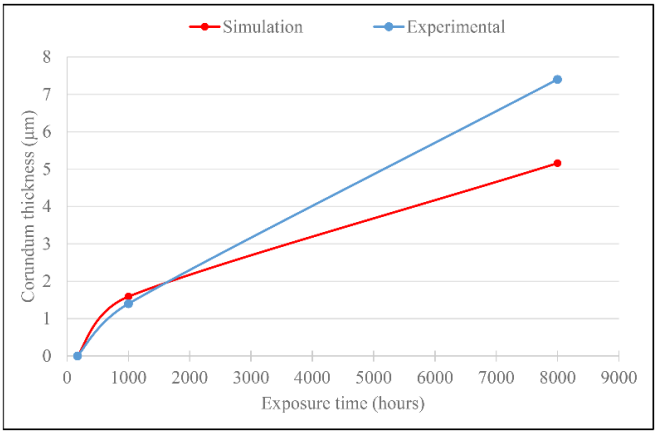

Figure 7.12: Growth kinetics of the chromium-rich, corundum-type oxide in the inward-growing scale of Alloy 27Cr33Ni3Mo (red - simulated kinetics; blue - experimental kinetics).

An interesting feature exhibited by alloy 27Cr33N3Mo during exposure was the formation of a fine grain region (FGR) in the alloy below the metal/scale interface, as indicated in Figure 7.11. These alloy fine grains are considered to play a significant role in the re-formation of the protective chromium-rich, corundum-type oxide on this alloy. The increased number of grain boundaries offers more diffusion pathways for ions to the scale and improves the corrosion behaviour [108,109]. For this reason, a detailed microstructural investigation on the formation and evolution of the FGR was carried out, the results of which are documented in **Paper VII**.

Figure 7.13a shows that the kinetics of the FGR follows what initially might be interpreted as parabolic growth. However, a plot of the depth of grain refinement against the square root of exposure time reveals that the data-points for the longest exposure times deviate from a strictly parabolic behaviour, as shown in Figure 7.13b. Thus, the kinetics of the FGR may be explained by the superparabolic-cubic kinetics, which accounts for grain boundary density in relation to scale growth, i.e., the consumption of chromium and formation of larger and larger grains towards the FGR/bulk interface (Figure 7.14). Accordingly, the FGR follows a parabolic behaviour in the earlier stages and shifts to a cubic behaviour in the later stages of oxidation.

SEM/EDX analysis of the samples exposed for 8000 hours reveals that the FGR is accompanied by chromium depletion and void formation along the alloy grain boundaries. The chromium depletion in the FGR indicates that the formation of these fine grains is correlated to the oxidation process/consumption of chromium.

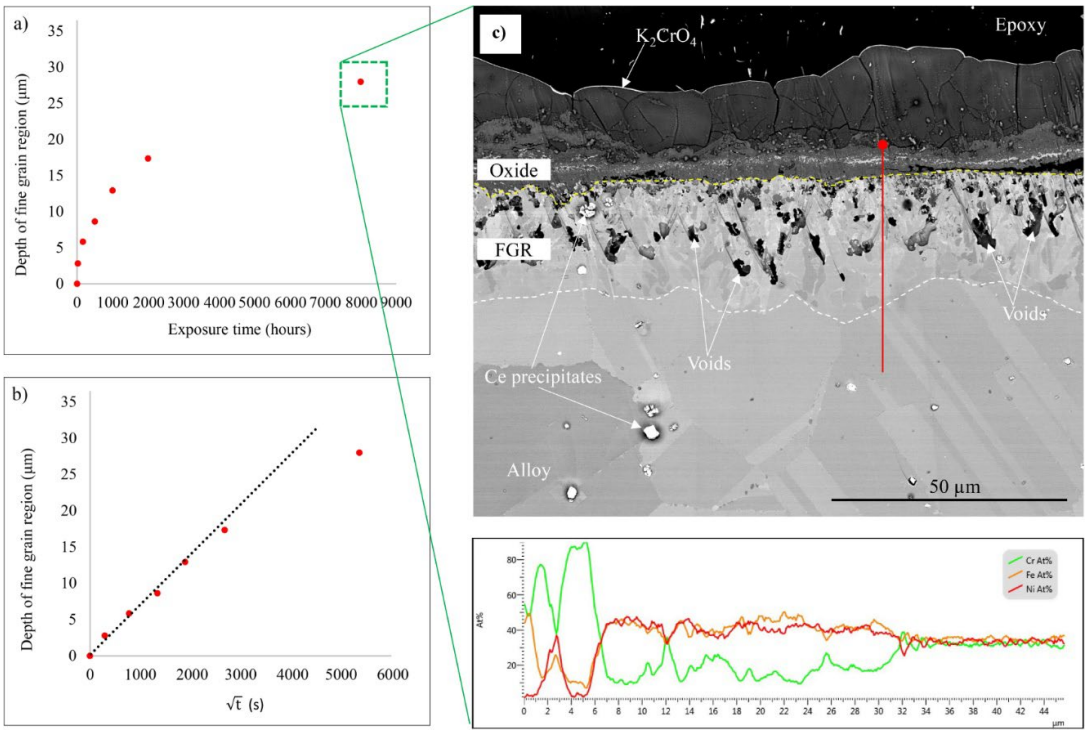

Figure 7.13: Sub-surface grain refinement in alloy 27Cr33Ni3Mo after exposure to 5% O_2 + 20% H_2O + N_2 (Bal) + KCl(s)/KCl(g): a) depth of grain refinement against exposure time; b) depth of grain refinement against square root of exposure time; c) SEM-BSE cross-sectional image revealing fine grains after 8000 hours of exposure and the corresponding line scan.

The EBSD-IPF image in Figure 7.14 shows that the fine grains are equiaxed and contain Σ3 twins with twin boundaries (highlighted with red lines). The kernel average misorientation (KAM) map, which shows local grain misorientation between pixels, reveals very low levels of misorientation in these fine grains. In general, the KAM is high in regions with high deformation due to high dislocation densities, whereas the low KAM values in the current fine grains indicate low deformation levels. The driving force for grain refinement in this alloy is suggested to be linked to the chemical potential caused by chromium oxidation. As chromium diffuses to the scale during oxidation, the alloy suffers gradual disintegration. During the disintegration process, new grain boundaries are initiated along easily accessible chromium pathways and are actualised by the continuous diffusion that materialises from the relaxation of vacancy-induced plane stresses.

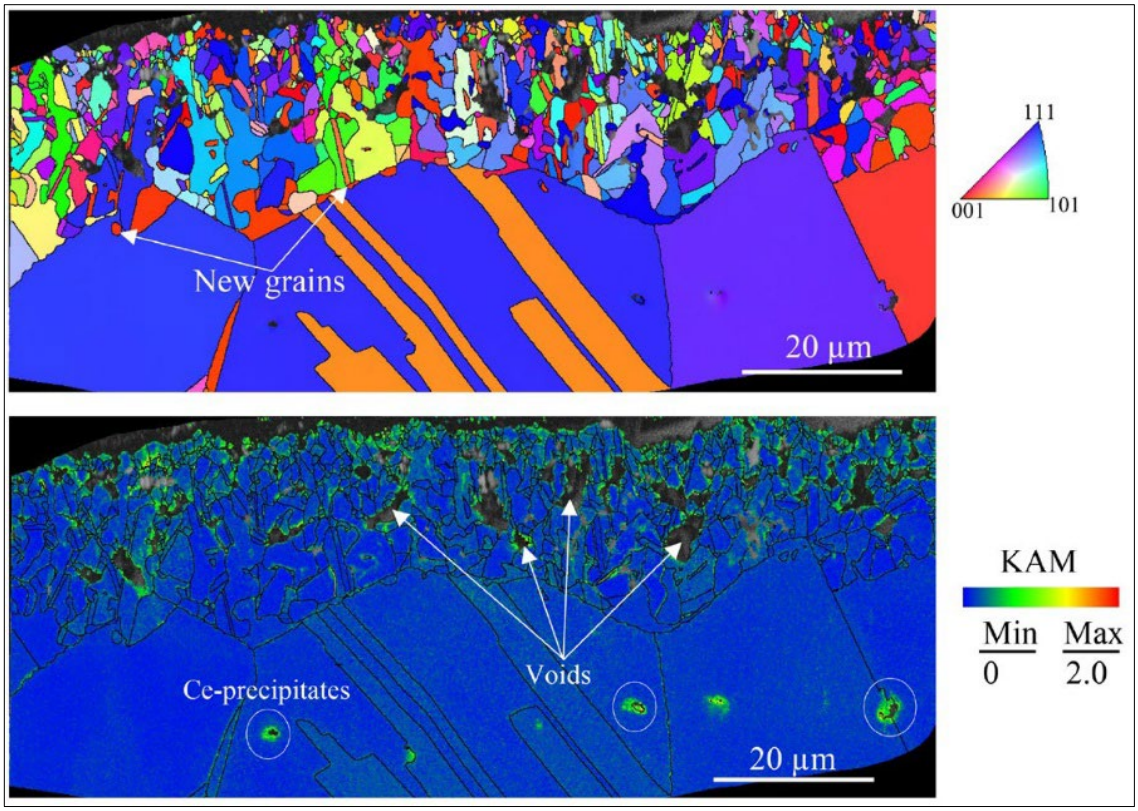

Figure 7.14: EBSD inverse pole figure (IPF) showing the fine grain microstructure and kernel average misorientation (KAM) map after exposure for 8000 hours.

It seems that the good secondary protection exhibited by alloy 27Cr33Ni3Mo after breakaway is a result of increased chromium diffusion to the scale, facilitated by the fine grain microstructure. Despite the beneficial effect of chromium enrichment of the scale, the extensive void formation due to the Kirkendall effect may undermine the structural integrity of the oxide scale when the material is exposed to a thermal or mechanical stress [110]. In long-term exposures, severe void formation could influence the corrosion behaviour of the alloys.

Ferritic FeCrAl model alloys (Fe10CrAl, Fe15CrAlSi and Fe20CrAlSi)

The ferritic FeCrAl model alloys were investigated to understand the impact of alloying elements on the formation of good/poor secondary protection during long-term exposures in the presence of KCl(s). Three FeCrAl model alloys, Fe10CrAl, Fe15CrAlSi and Fe20CrAlSi, were exposed to two environments, K_2CO_3 and $KCl+H_2O+O_2$, at 600°C for 2000 hours. The results of this investigation are documented in **Paper IV**. However, the focus in the thesis will be on the results obtained from the exposures conducted in $KCl+H_2O+O_2$.

Based on average oxide thickness measurements displayed in Figure 7.8, the three alloys exhibit varying degrees of corrosion resistance within the secondary corrosion regime, since breakaway is expected to occur very early in the exposures [64]. The alloys in order with increasing corrosion resistance are as follows: Fe10CrAl < Fe15CrAlSi < Fe20CrAlSi. After 2000 hours of exposure, the Fe10CrAl alloy forms an ~320 µm thick, multi-layered oxide scale, with a growth rate that is suggested to be governed by the diffusion of ions (Figure 7.15a). The outward-growing scale consists of hematite and magnetite, while the inward-growing scale is identified as Fe,Cr,Al spinel-type oxide. The poor secondary protection exhibited by this alloy may be associated with the microstructure of the inward-growing oxide. As shown in Figure 7.15b, the inward-growing scale of this alloy is characterised by extensive pore formation. The absence of rapid chromium replenishment to the scale, to form a protective chromium-rich inner scale, leads to a porous, iron-rich, inward-growing scale that is caused by internal oxidation and very fast diffusion paths.

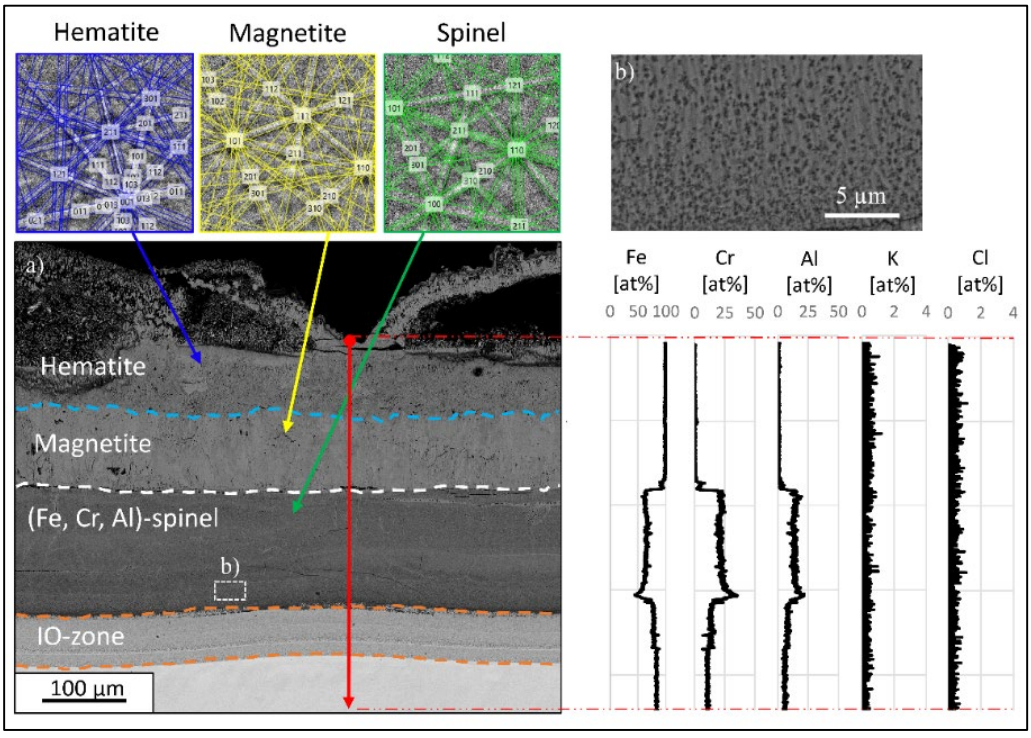

Figure 7.15: SEM-BSE images of the Fe10CrAl alloy after exposure to $O_2+H_2O+N_2$ and KCl at 600°C for 2000 hours.

The Fe15CrAlSi (Figure 7.16) and Fe20CrAlSi (Figure 7.17) alloys exhibit improved secondary protection, as evident from the formation of thinner oxide scales after exposure for 2000 hours. Both alloys form multi-layered oxide scales that consist of outward- and inward-growing scales. The outer scales are mostly iron-rich oxides (hematite and magnetite), while the inner scales are composed of both spinel- and corundum-type oxides. It should be noted that a higher concentration of corundum phase was detected along the entire inner scale of the Fe20CrAlSi alloy, as compared with the Fe15CrAlSi alloy.

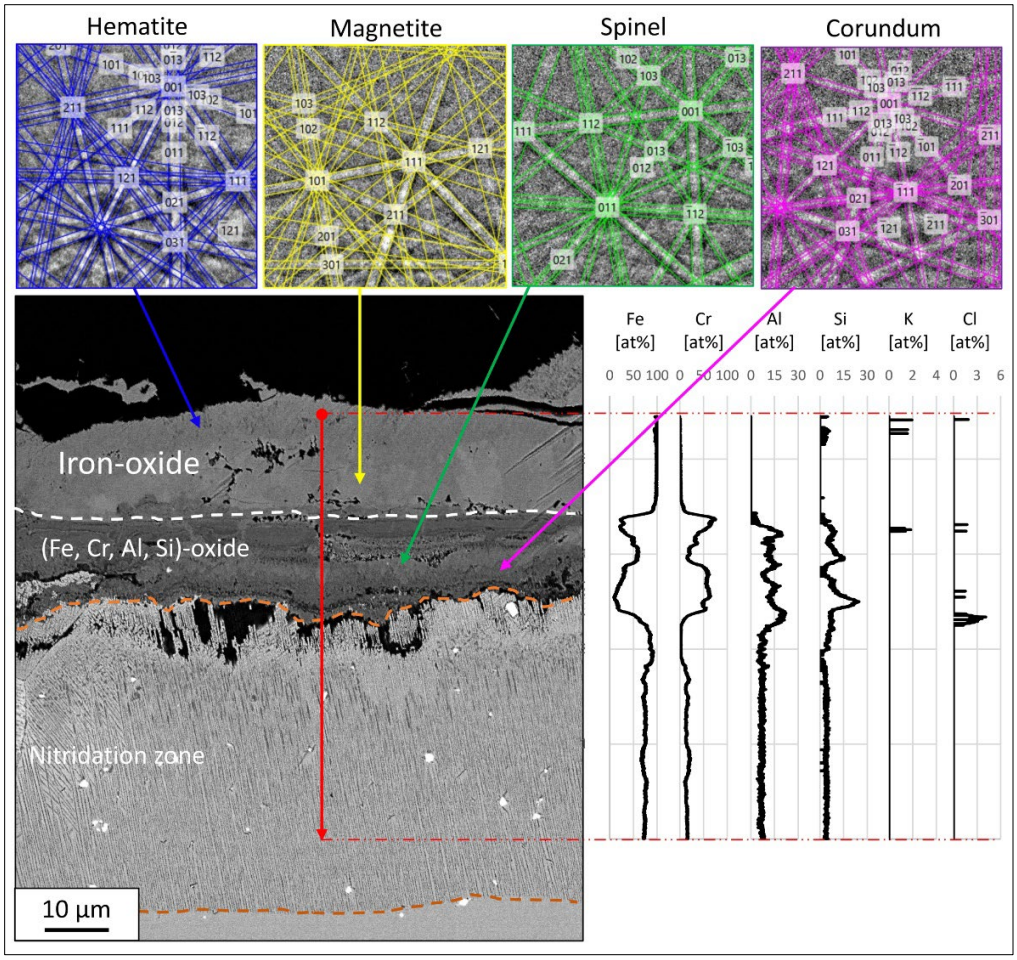

Figure 7.16: SEM-BSE image of the Fe15CrAlSi alloy after exposure to O_2+H_2O+N_2 and KCl at 600°C for 2000 hours.

Underneath the scales, these FeCrAl alloys form thick nitridation zones (see, for example, Figure 7.17). The occurrence of nitridation implies that the oxide scales formed on the alloys are permeable to nitrogen. From a corrosion perspective, the process of alloy nitridation may negatively influence the corrosion behaviour. This is because aluminium, which is beneficial for forming a protective oxide scale, is bound in the form of aluminium nitride (AlN).

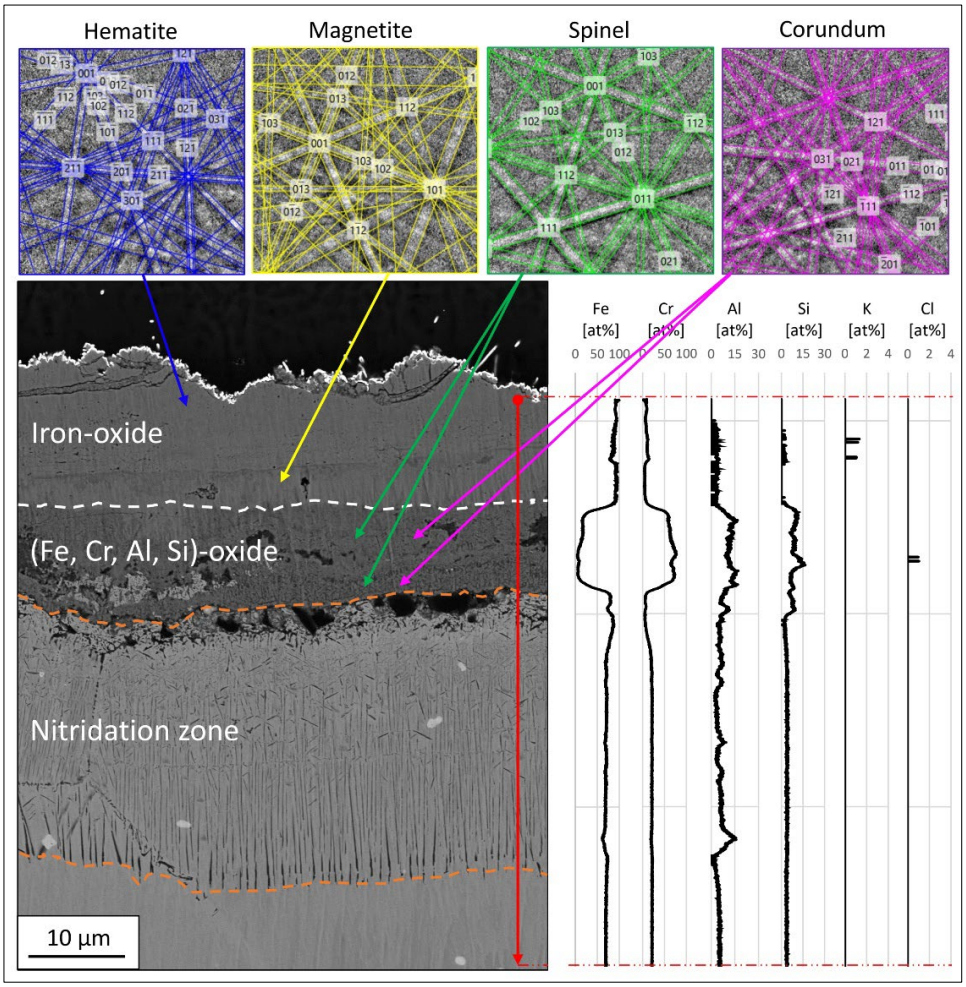

Figure 7.17: SEM-BSE image of the Fe20CrAlSi alloy after exposure to O_2+H_2O+N_2 and KCl at 600°C for 2000 hours.

The improved corrosion behaviours displayed by the Fe15CrAlSi and Fe20CrAlSi alloys during long-term exposure are associated with the increased chromium activity in the bulk, together with the minor addition of silicon. Several studies have reported the beneficial effect of adding chromium [64,106] and silicon [49,111] to high-temperature alloys. In this study, the beneficial effect of silicon on the corrosion resistance of Fe15CrAlSi and Fe20CrAlSi alloys is attributed to its ability to prevent internal oxidation (IO), which is otherwise observed in the Fe10CrAl alloy (see Figure 7.15). It has been proposed that the process of internal oxidation may be detrimental to the secondary protection [64].

In summary, the detailed microstructural analysis shows that the alloys form either fast-growing and less-protective, iron-rich oxide scales, i.e., poor secondary protection, or slow-growing and more-protective chromium/aluminium-rich oxide scales, i.e., good secondary protection. It is considered that the re-formation of a protective corundum-type oxide, which is influenced by the alloying elements and alloy microstructure, is crucial to improving the corrosion resistance properties of the alloys.

7.2.3 Impact of increased chlorine load on the oxide scales formed after breakaway

It is well-known that during biomass/waste combustion, the superheater materials are continuously exposed to alkali chloride species (mimicked by the KCl(s) in current set-up), as well as HCl. To investigate the impact of the combination of KCl(s)/KCl(g) and HCl on oxide scales formed within the secondary corrosion regime, three alloys (SVM12, APMT and alloy 27Cr33Ni3Mo) were exposed at 600°C for 168 hours to three environments: (i) 5% O_2 + 20% H_2O + N_2 (Bal.); (ii) 5% O_2 + 20% H_2O + N_2 (Bal) + KCl(s)/KCl(g); and (iii) 5% O_2 + 20% H_2O + N_2 (Bal) + KCl(s)/KCl(g) + HCl(g). The results of this study are reported in **Paper V**.

The gravimetric results in Figure 7.18 show the impacts of the different environments on the investigated alloys. The SVM12 alloy exhibits the largest mass gains in all the environments. The impact of the environment is very clear, and the presence of KCl increases the mass gain more than 3-fold compared with the H_2O exposure. With the addition of more Cl (in the form of HCl), the mass gain is more than 5-fold higher than the level seen in the case with only H_2O.

On the other hand, the APMT and 27Cr33Ni3Mo alloys exhibit much lower mass gains. In the absence of KCl (i.e., H_2O only), these alloys display very low mass gains and are in the range of thicknesses expected for the primary protection. In the presence of KCl, both alloys display increased mass gains, albeit much lower than the mass gains for SVM12 in the corresponding environments. It should be noted that the results indicate that an increased Cl load does not accelerate the corrosion in the secondary regimes of these alloys.

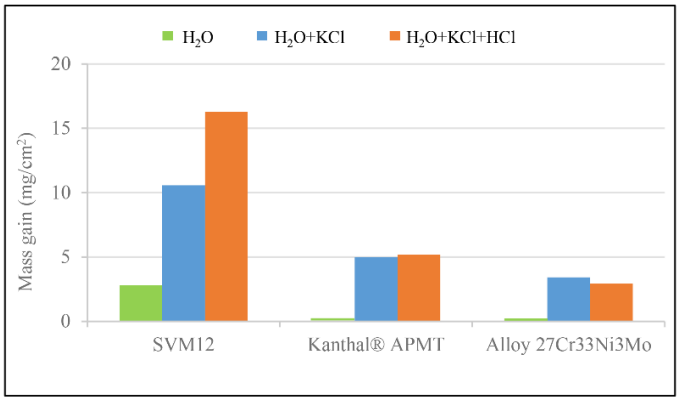

Figure 7.18: Mass gains (in mg/cm^2) for the SVM12, Kanthal® APMT and alloy 27Cr33Ni3Mo after 168 hours of exposure to H_2O, H_2O+KCl and H_2O+KCl+HCl at 600°C.

Figure 7.19 shows the SEM-BSE cross-sectional image of the oxide microstructure of SVM12, together with the corresponding elemental analyses (line scans and maps). This alloy forms dense oxide scales with measured thicknesses of 63 µm, 93 µm, and 123 µm in H_2O, H_2O+KCl, and H_2O+KCl+HCl, respectively. The scales consist of outward- and inward-growing oxide layers in all cases. White dashed lines have been drawn in the figure to highlight the outward-/inward-growing scale interfaces. According to the SEM/EDX analysis, the outward-growing scales are composed of Fe-rich oxides, while the inward-growing scales are mixed Fe,Cr oxides. In the high Cl load environment, i.e., H_2O+KCl+HCl, the inward-growing scale is double the thickness of the corresponding scale in the low Cl environment, i.e., H_2O+KCl.

The formation of thick and fast-growing iron-rich oxide scales by SVM12 clearly demonstrates that this alloy forms poor secondary protection in all the exposure environments. These dense oxide scales strongly indicate a diffusion-controlled growth mechanism that is governed by ion diffusion, which supports the notion that the addition of KCl accelerates both iron and oxygen diffusion, while the addition of HCl accelerates the inward diffusion of oxygen in the current set-up. The rapid inward-diffusion of oxygen limits the possibility to form a chromium-rich, good secondary protection and instead the scale exhibits signs of detrimental internal oxidation [112]. It should be noted that no evidence of active oxidation, which is driven by gas diffusion of $Cl_2(g)$ through the scale, could be observed. Instead, the results support a diffusion-driven mechanism and suggest that the role of the Cl ions is to increase the diffusion of ions, i.e., the electrochemical mechanism [87].

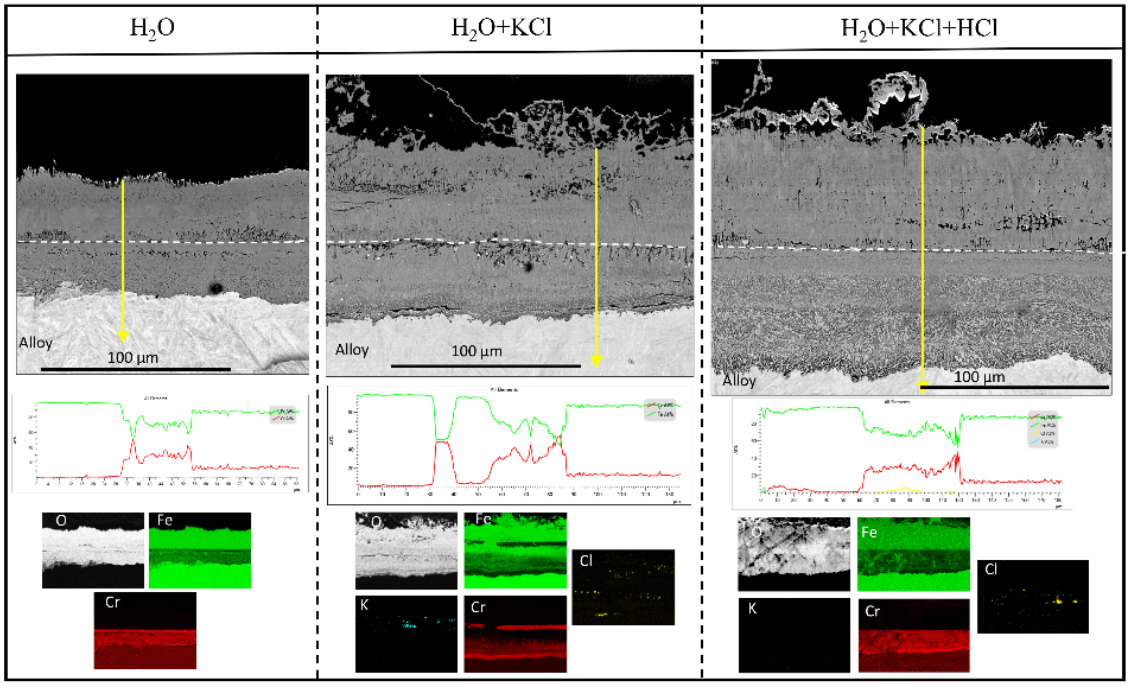

Figure 7.19: SEM-BSE cross-sectional images with EDX analysis for SVM12 after 168 hours exposure in H_2O, H_2O+KCl, and H_2O+KCl+HCl at 600°C.

In the cases of the APMT and 27Cr33Ni3Mo alloys, the microstructural investigation reveals that these alloys form thinner oxide scales in Cl-containing environments, as compared with SVM12, as shown in Figure 7.20. In the H_2O+KCl environment, the microstructures are characterised by the formation of large K_2CrO_4 particles at the surface. The inner scale formed on APMT is enriched for aluminium, while the inner scale formed on alloy 27Cr33Ni3Mo is enriched for chromium. Upon adding HCl, the EDX analysis do not show any indication of K_2CrO_4 on the sample. However, the primary protection is clearly destroyed, and the sample is in the secondary protection regime. It is suggested that the formed K_2CrO_4, during breakaway, is converted back to chromia and KCl(s) via reaction with HCl(g). This is evident on the chromium map for alloy 27Cr33Ni3Mo which reveals the presence of chromium in the outward-growing scale. Similar corrosion behaviour has been reported for a stainless steel exposed to KCl and SO_2 at 600°C [113]. The thin oxide scales are not only maintained but the results indicate that they are enriched for chromium such that it exceeds 67.7 at-% cations (maximum limit for the concentration of trivalent ions in

a spinel structure [114]). Such high chromium concentrations are only possible in a corundum-type oxide structure. The low mass gains exhibited by APMT and 27Cr33Ni3Mo in combination with the formation of thin chromium-rich oxide scales demonstrate that these alloys form good secondary protection in harsh environments. The impact of increasing Cl load on the good secondary protection is very limited in this set-up and for these exposure durations.

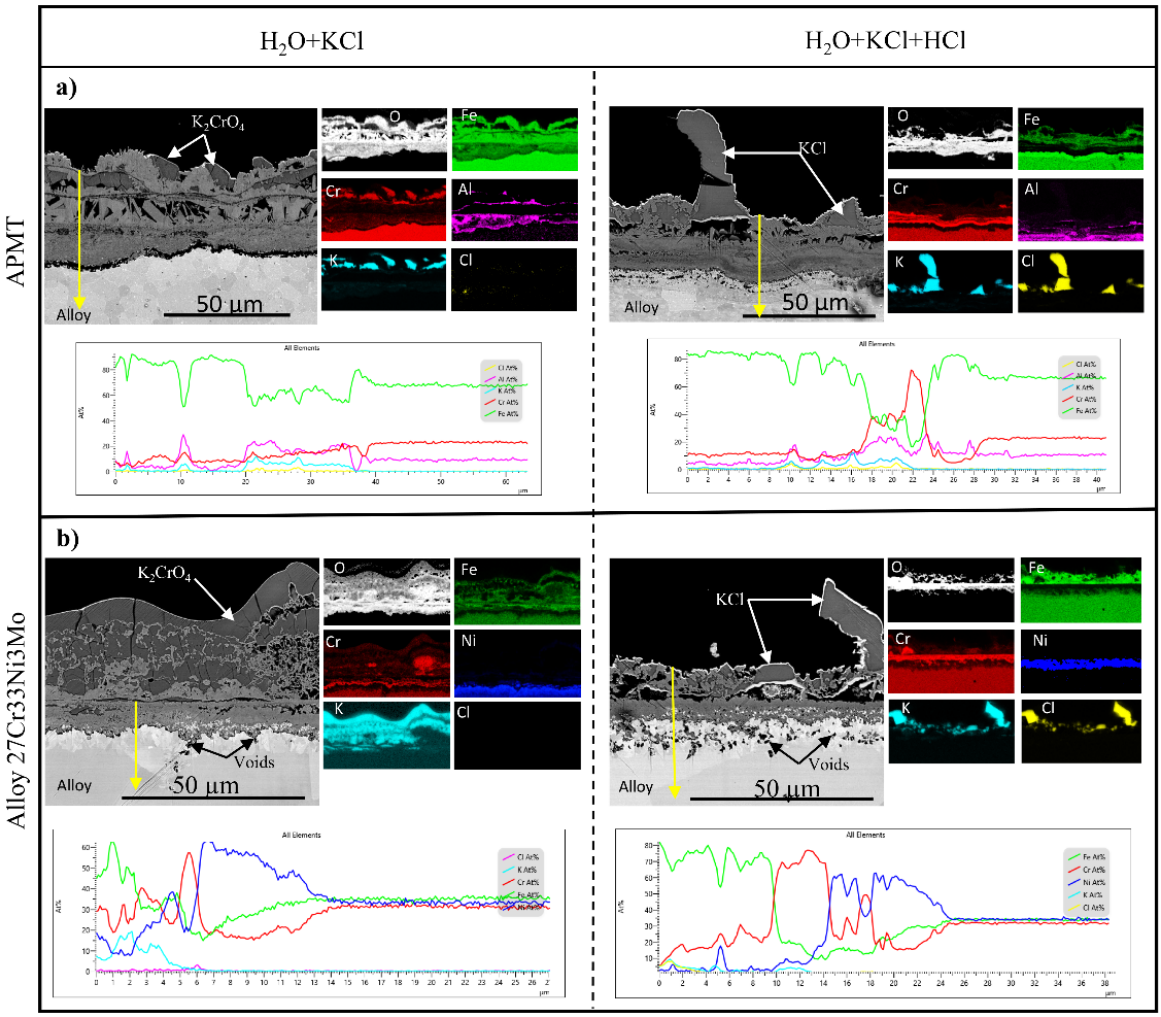

Figure 7.20: SEM-BSE cross-sectional images with EDX analysis for a) Kanthal® APMT and b) alloy 27Cr33Ni3Mo, after 168 hours of exposure in H_2O+KCl and H_2O+KCl+HCl at 600°C.

In summary, the results of the corrosion investigations performed on FeCr(Ni), NiCr and FeCrAl(Si) alloys demonstrate that the experimental set-up is effective in terms of providing reliable data that allow a better understanding of the secondary corrosion protection properties of these alloys in the presence of KCl(s). The results from the initial investigation (500 hours) show that the alloys exhibit corrosion behaviours that may be categorised as poor secondary protection, i.e., fast-growing iron-rich oxide scales, or good secondary protection, i.e., slow-growing chromium/aluminium-rich oxide scales. Within the secondary corrosion regime, scale growth is governed by the diffusion of ions through the scale in all cases, including in the high-Cl load environment. The long-term oxidation kinetics, together with the microstructural

evolution, show that the properties of the secondary protection are influenced by the alloying elements and the bulk microstructure. In particular, certain alloys can re-form the protective chromium/aluminium-rich corundum-type oxides in harsh environments. The increased Cl load leads to accelerated corrosion of the poor secondary protection, whereas the good secondary protection is more or less unaffected under the conditions of the current experimental set-up.

7.2.4 Long-term corrosion kinetics under laboratory conditions

The results obtained with KCl(s), which enables well-controlled long-term exposures in a laboratory environment, contribute to a better understanding and prediction of corrosion in more complex systems. In the case of the superheater alloys, an approach based on long-term corrosion kinetics, from laboratory exposures, can be deployed to assess and predict corrosion in a complex boiler environment. This approach is based on the propagation phase of the oxidation process, i.e., the secondary corrosion regime (after the breakaway), as it is expected that the stainless superheater steels undergo fast breakaway oxidation under these harsh conditions. The life-time of the materials will, therefore, be determined by their corrosion behaviours beyond breakaway. This will be elaborated below to address the second research question in this thesis.

> **Research question 2:** How can long-term corrosion kinetics under laboratory conditions be used to understand the mechanisms and predict oxidation behaviour in complex boiler environment?

To be able to predict oxidation behaviour in a complex boiler environment, long-term corrosion exposures were initially performed in a laboratory environment consisting of 5% O_2 + 20% H_2O + N_2 (Bal). + KCl(s)/KCl(g) at 600°C, for 168, 500, 1000 and 8000 hours. The investigated materials included four coatings from three material classes, i.e., a marginal chromia former (ferritic-martensitic stainless steel), two FeCrAl coatings (a lean FeCrAl with 12.4 wt-% Cr and a normal FeCrAl with 21 wt-% Cr) and a Ni-based coating. The chemical compositions of the investigated coatings are listed in **Paper VI**. The same materials were also exposed in three commercial boilers for 1000, 2000 and 3000 hours. For more details, see the *Experimental* section.

Figure 7.21 shows the oxidation kinetics obtained from the laboratory corrosion tests as measured oxide thickness vs exposure time. As shown, the oxidation kinetics of the coatings varies and can be ranked (from fastest oxide growth to slowest oxide growth) as follows: marginal chromia former > lean FeCrAl > FeCrAl > Ni-based coating. The marginal chromia former displays a rapid oxidation pattern that follows parabolic kinetics with very small deviations. The two FeCrAl coatings display intermediate oxidation kinetics. The Ni-based coating displays the slowest kinetics, with deviations from parabolic behaviour.

To correlate these oxidation kinetics to the corrosion behaviours in a boiler environment, the kinetics were re-plotted using [Eq. (7.1)] to obtain parabolic rate constants (k_p-values) for each coating, as shown in Figure 7.21b. By applying [Eq. (7.1)] and the derived k_p values, a theoretical oxide thickness (X) can be calculated for any given time. The calculated oxide thickness is compared with the measured oxide thickness from field exposures of the same duration in Table 7.1.

$$X = k_p * \sqrt{t} \qquad (7.1)$$

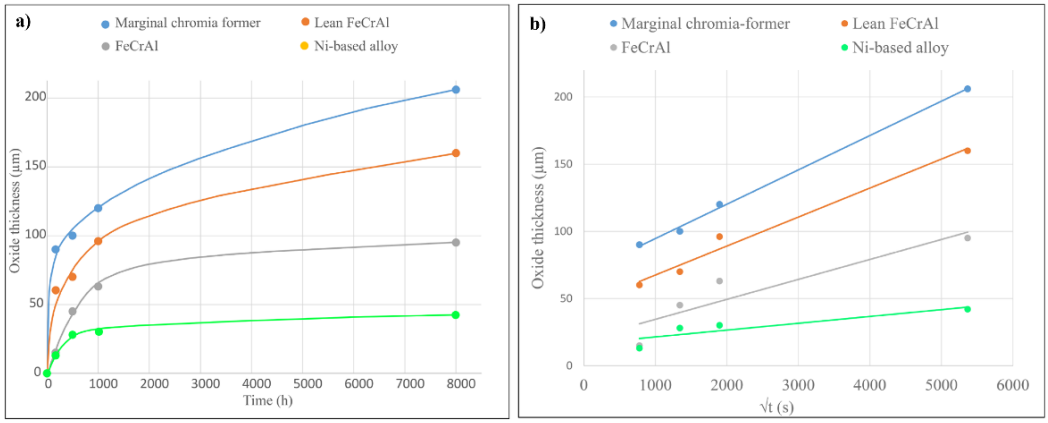

Figure 7.21: Oxidation kinetics based on oxide thickness measurements after exposure in a laboratory environment (5% O_2 + 20% H_2O + N_2 (Bal). + KCl(s)/KCl(g)) at 600°C. The oxide thicknesses of the samples tested in laboratory were measured from the SEM cross-sectional images using the ImageJ software.

Table 7.1 shows the calculated oxide thicknesses in the laboratory environment and the average measured oxide thickness in the boiler environment. The results show that the calculated/predicted thicknesses are in good agreement with the measured average thicknesses for the marginal chromia former, lean FeCrAl and FeCrAl. The Ni-based coating showed a large difference between the predicted thickness (25 µm) and the measured thickness (120 µm). This might be due to the effects of other corrosion processes that disrupt the normal oxidation of this coating. The oxide microstructures may provide additional insights into the corrosion behaviour and be used to explain any deviations from the predictions.

Table 7.1: Calculated oxide thicknesses using the derived k_p values, and the measured average oxide thicknesses upon field exposures.

Coating	**Laboratory environment** Calculated oxide thickness (µm)	**Boiler environment** Average measured oxide thickness (µm)	**Exposure time** (hours)
Marginal chromia former	148	150	3000
Lean FeCrAl	119	50 (inner)/100	2000
FeCrAl	69	70	3000
Ni-based coating	25	120	1000

7.2.5 Oxide microstructural investigation – laboratory vs. field

An investigation of the oxide microstructures was performed for both the laboratory- and field-exposed samples. Figure 7.22 shows the SEM-BSE cross-sectional images of the samples. In general, all the samples formed thick, dual-layered oxide scales that consisted of outward-growing and inward-growing scales. The dashed white lines are drawn to highlight the outward-/inward-growing scale interfaces. The microstructures are characterised by the formation of K_2CrO_4 particles at the surface and, in some cases, also within the oxide scale.

The oxide scales formed on the marginal chromia former under laboratory conditions are dense and strongly adherent to the metal. The elemental analyses show that the outward-growing layers are iron-rich oxides, while the inward-growing scales are iron- chromium oxides. A similar microstructure was observed for the field-exposed sample, indicating the existence of a diffusion-controlled growth mechanism in both cases, which would explain the good agreement between the calculated and measured oxide thicknesses.

The FeCrAl alloys exhibit intermediate corrosion resistance and form dense oxide scales in both the laboratory and boiler environments. Notably, the FeCrAl coating develops a thinner oxide scale than the lean FeCrAl variant. This variation in corrosion performance is likely due to the alloying elements, where the higher chromium content in the FeCrAl alloy plays a critical role in promoting the formation of a more-protective oxide scale. Indeed, SEM/EDX analysis shows that the inward-growing oxide in FeCrAl contains up to 70 at-% chromium after 8000 hours of exposure, as compared to 55 at-% chromium in the lean FeCrAl sample. This level of formation would be expected to change the oxidation kinetics over time, explaining the deviations from parabolic kinetics and the calculated value.

In the case of the Ni-based coating, the formation of large K_2CrO_4 particles was observed at the surface. According to the SEM/EDX analysis, the thin oxide scales formed under laboratory conditions are very chromium-rich, indicating the formation of a good secondary protection. This again deviates from strictly parabolic kinetics, as this more-protective scale is expected to form after some time. The sample exposed in the waste-fired boiler for 1000 hours forms a much-thicker oxide scale (about 120 µm) compared with the predicted thickness, i.e., 25 µm. This large discrepancy may be explained by the absence of the protective layer at the metal/scale interface, as observed on the sample exposed under laboratory conditions. The chemical analysis of the deposit over the Ni-based coating from the boiler revealed the presence of a higher Cl concentration, although this was not the case for the sample exposed to KCl(s)/KCl(g) in the laboratory. The high levels of Cl in the environment, in combination with the high flue gas temperature (almost 900°C in the boiler) could impact the corrosion process of the material. The formation of several K_2CrO_4 layers indicates that the corrosion process re-starts several times, thereby restraining the material from re-forming a protective scale.

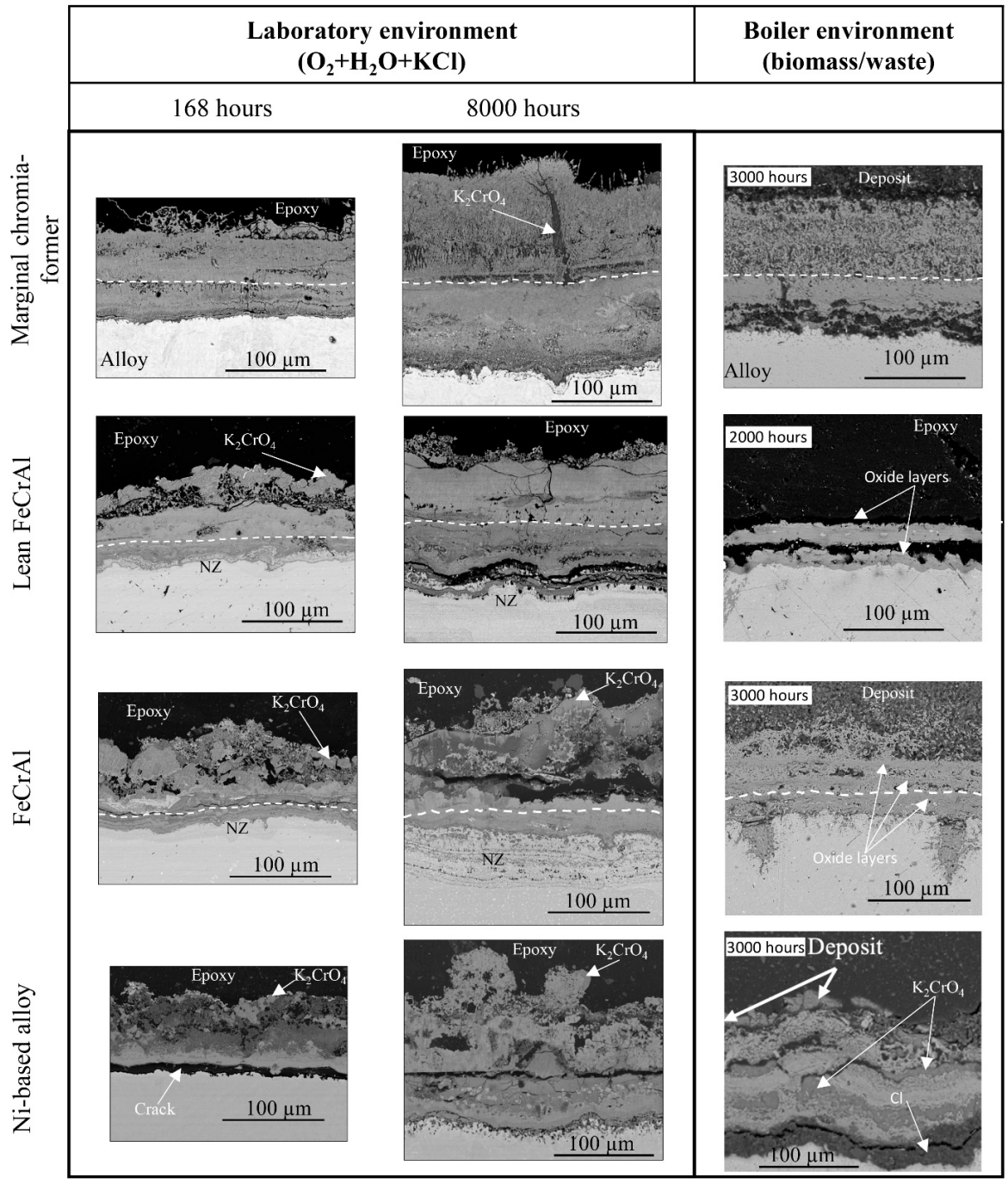

Figure 7.22: SEM-BSE cross-section images showing the oxide microstructure after exposure in laboratory environment (O_2+H_2O+KCl) and biomass- and waste-fired boiler environment at 600°C.

In summary, the results of this study demonstrate that long-term corrosion kinetics under laboratory conditions can be utilised to improve the understanding of mechanisms and predict the oxidation behaviours of materials exposed in the complex boiler environment. The parabolic rate constant (k_p) derived from laboratory exposures becomes a tool that enables prediction of the oxide thickness in the boiler, and the oxide scale microstructure provides insights into the possible corrosion mechanisms. The calculated/predicted oxide thicknesses under laboratory conditions were in good agreement with the measured oxide thicknesses of some of the samples exposed in the boiler, and the deviations could be explained through the microstructural investigation.

8 Summary and Final remarks

The aim of this thesis was to investigate corrosion mechanisms in long-term laboratory exposures, to enable better predictions of the progress of corrosion in materials and coatings used for boiler applications. Various aspects are explored, including the development of a set-up for long-term corrosion investigations, the corrosion mechanisms for both bulk materials and coatings, the influence of alloying elements, the impact of alloy microstructure and exposure environment. A summary of the findings and final remarks are presented below.

8.1 Experimental set-up for long-term corrosion testing

The approach in this work has been to perform well-controlled, long-term corrosion investigations by designing an experimental set-up that mimics the key corrosive species in biomass-fired and waste-fired boilers in a systematic way. The exposures were carried out at 600°C in the presence of 5% O_2 + 20% H_2O + N_2 (Bal) + KCl(s)/KCl(g) (+HCl). Since KCl(s) has a high evaporation rate at 600°C, a KCl source was introduced upstream of the samples to saturate the gas and reduce evaporation of the KCl from the sample surfaces. This set-up was shown to be reliable, based on the robustness test using 18 samples of the stainless steel SVM12. The reliability of the set-up is a key requisite for performing long-term laboratory corrosion investigations in an effective way. The obtained results show that the position of the samples has a very limited impact. The corrosiveness of the selected chemical environment is evident from the high mass gains of the SVM12 samples, which indicate that the alloy undergoes breakaway oxidation and transitions to a secondary protection regime.

8.2 Long-term alkali chloride-induced high-temperature corrosion

The long-term alkali chloride-induced high-temperature corrosion of various alloys was investigated to address the following primary research questions.

> **Research question 1.** What are the mechanisms that control the formation of good/poor secondary protection on FeCr(Ni), NiCr and FeCrAl(Si) alloys during long-term laboratory exposures to KCl at 600°C?

All of the investigated alloys suffer rapid breakaway corrosion in the presence of water vapour and KCl, with the primary protection transforming into secondary protection. The dominant breakaway mechanism is identified as the reaction with alkali in all cases, and the resulting oxide scale is in all cases governed by ion diffusion. No signs of active oxidation (i.e., diffusion of Cl_2(g) and gaseous metal chlorides through the scale) are observed. Instead, parabolic kinetics is often established, which indicates that ion diffusion through the scale controls the corrosion rate. Within the secondary corrosion regime, the alloys exhibit different levels of corrosion resistance in the presence of KCl(s). The formed oxide scales can be classified as: poor secondary protection, i.e., a fast-growing iron-rich oxide scale; and good secondary protection, i.e.,

a slow-growing chromium/aluminium-rich oxide scale. Alloys such as SVM12, Kanthal® EF100 and Fe10CrAl exhibit poor secondary protection, which is attributed to the low chromium/aluminium/silicon activity in the bulk. Furthermore, the poor secondary protection on SVM12 is negatively impacted by increased Cl activity in the environment.

In contrast, Kanthal® EF101, APMT, alloy 27Cr33Ni3Mo, A625, Fe15CrAlSi and Fe20CrAlSi alloys exhibit good secondary protection in the presence of KCl(s). These alloys exhibit low mass gains and re-form the protective chromium/aluminium-rich corundum-type oxide in the inward-growing scales (i.e., a healing layer). Such scale growth is facilitated by the high activities of alloying elements such as chromium, aluminium and silicon in the bulk. In addition, it is considered that the alloy microstructures contribute to the improved corrosion performances of the alloys by facilitating faster diffusion of elements. This is demonstrated by the alloy 27Cr33Ni3Mo and Kanthal® EF101 bulk material, which exhibit faster formation of the chromium/aluminium-rich oxide scales due to fine grain alloy microstructures. In the presence of an increased Cl load, the good secondary protection of these alloys is unaffected. Instead, these alloys experience greater chromium enrichment in the scale, which improves their corrosion performances.

> **Research question 2.** How can long-term corrosion kinetics under laboratory conditions be used to understand the mechanisms and predict oxidation behaviour in the complex boiler environment?

This thesis aims to improve understanding of the alkali chloride-induced corrosion that occurs in the boiler environment by enabling assessments of long-term, laboratory-based corrosion kinetics, together with oxide microstructural analyses. The results were used to examine the corrosion behaviours of alloys that were exposed in complex commercial boilers. The parabolic rate constant (k_p) from laboratory exposure kinetics was used to predict the oxide thickness in the boiler environment. The oxide thickness predicted using laboratory oxidation kinetics was in good agreement with the measured oxide thickness for most of the alloys exposed in the boiler. In those cases, in which there was deviation in the predictions, oxide microstructural analyses provided insights into a different corrosion behaviour. Such a deviation was observed for the Ni-based coating, where the sample exposed in the boiler environment formed a much thicker oxide scale than was predicted. The findings of this investigation demonstrate that parabolic rate constants derived from long-term laboratory corrosion kinetics can be useful for predicting corrosion in the complex boiler environment.

8.3 Final remarks

The selection of materials is a critical factor in advancing the use of biomass and waste fuels in combustion processes for heat and power generation. This thesis provides valuable insights into the complex interactions between combustion environments and the materials employed, highlighting the importance of understanding material degradation, so as to develop advanced material solutions. By examining the long-term corrosion behaviours and scale growth mechanisms, it is demonstrated that alloys these alloys are expected to undergo breakaway corrosion in alkali chloride-rich environments and the key to enhanced corrosion resistance is the ability to form/sustain a good secondary protection. By addressing the challenges of high-temperature corrosion associated with the combustion of these fuels, key parameters such as material life-time and electrical efficiency can be significantly improved. The incorporation of materials with improved corrosion resistance and extended life-spans into combustion systems will not only increase

energy outputs but will also mitigate environmental impacts. Thus, through careful consideration of the effects of alloying elements and alloy microstructural features, alloys can be designed and developed to achieve enhanced performance in boiler environments.

9 Outlook

The focus of this thesis has been on improving the understanding of high-temperature corrosion properties of materials and coatings used for boiler applications. The exposure conditions were chosen with the consideration to enhance electrical efficiency in CHP plants. As reported in other studies [115,116], raising the outlet steam temperature/pressure to 600°C/240 bar increases the power output and electrical efficiency by up to 4% in a biomass-fired boiler from the current level of 560°C/300 bar (state-of-the-art steam data). However, raising the steam temperature would increase the material temperature to slightly above the steam temperature, subjecting the material to a more-corrosive environment. The results of this thesis provide the foundation for further research on developing alloys that enable boiler operations at higher temperatures and pressures.

This work may open up future research avenues on the following topics:

1. LIFE-TIME PREDICTION MODELLING

Future advances in methods for predicting material life-times could extend the service life-times of boiler components and ensure the reliability of biomass-/waste-fired power plants. One key area of development could be the integration of advanced computational models and machine learning algorithms to predict material degradation under real-life boiler operating conditions. Such systems could continuously refine the predictions, provide more-precise estimations of component life-times, and identify early signs of material failure. Moreover, calculations could be adopted to gain further insights into the relationships between steam data and material systems. Thus, alloys could be tailored and designed to operate under targeted conditions.

2. TRIGGERING PROTECTIVE OXIDES AFTER BREAKAWAY

Certain alloys have been shown to be capable of re-forming the protective chromium/aluminium-rich oxide scales after breakaway (i.e., healing layer). While the scale growth and formation of such protective oxide scales can indeed occur during long-term exposures, it would be advantageous to have these protective layers achieved more rapidly, especially during the early operational phase of the boiler. Research into the specific parameters, such as temperature ramps, pressure cycles, and steam quality adjustments, could facilitate enhancement of the corrosion resistance of the alloy. Moreover, insights into the protective properties and breakaway mechanisms of such oxide scales would be of great importance.

3. ROLES OF OTHER ALLOYING ELEMENTS

The beneficial effects of alloying elements, e.g., chromium and aluminium, on the high-temperature corrosion of alloys is well-established, especially in short-term laboratory studies. However, it is relevant to explore the roles of other elements, in particular molybdenum, to understand their effects in the post-breakaway corrosion regime. This is especially important because molybdenum is used in several alloys that have been developed for high-temperature applications. Further research into the effect of molybdenum on alkali chloride-induced high-temperature corrosion of steels, particularly in synergy with other alloying elements, could help reshape alloy design strategies.

References

[1] International Energy Agency, World Energy Outlook 2024, Paris, 2024. https://www.iea.org/reports/world-energy-outlook-2024 (accessed November 18, 2024).

[2] B.R. (eds.) H.-O. Pörtner, D.C. Roberts, M. Tignor, E.S. Poloczanska, K. Mintenbeck, A. Alegría, M. Craig, S. Langsdorf, S. Löschke, V. Möller, A. Okem, Climate Change 2022: Impacts, Adaptation, and Vulnerability. Contribution of Working Group II to the Sixth Assessment Report, Cambridge, 2022. https://doi.org/doi:10.1017/9781009325844.

[3] K.F. Myers, P.T. Doran, J. Cook, J.E. Kotcher, T.A. Myers, Consensus revisited: quantifying scientific agreement on climate change and climate expertise among Earth scientists 10 years later, Environmental Research Letters 16 (2021) 104030. https://doi.org/10.1088/1748-9326/ac2774.

[4] N. Oreskes, The Scientific Consensus on Climate Change, Science (1979) 306 (2004) 1686. https://doi.org/10.1126/science.1103618.

[5] C. Yin, S. Li, Advancing grate-firing for greater environmental impacts and efficiency for decentralized biomass/wastes combustion, Energy Procedia 120 (2017) 373–379. https://doi.org/10.1016/J.EGYPRO.2017.07.220.

[6] D.S. Gunarathne, P. Mellin, W. Yang, M. Pettersson, R. Ljunggren, Performance of an effectively integrated biomass multi-stage gasification system and a steel industry heat treatment furnace, Appl Energy 170 (2016) 353–361. https://doi.org/10.1016/J.APENERGY.2016.03.003.

[7] C. Gough, P. Upham, Biomass energy with carbon capture and storage (BECCS or Bio-CCS), Greenhouse Gases: Science and Technology 1 (2011) 324–334. https://doi.org/10.1002/ghg.34.

[8] J. Pettersson, H. Asteman, J.-E. Svensson, L.-G. Johansson, KCl Induced Corrosion of a 304-type Austenitic Stainless Steel at 600°C; The Role of Potassium, Oxidation of Metals 64 (2005) 23–41. https://doi.org/10.1007/s11085-005-5704-3.

[9] J. Pettersson, C. Pettersson, H. Asteman, J.-E. Svensson, L.-G. Johansson, A pilot plant study of the effect of alkali salts on initial stages of the high temperature corrosion of alloy 304L, Materials Science Forum 461–464 (2004) 965–972.

[10] S. Kiamehr, K. V Dahl, M. Montgomery, M.A.J. Somers, KCl-induced high temperature corrosion of selected commercial alloys; KCl-induced high temperature corrosion of selected commercial alloys, (2015). https://doi.org/10.1002/maco.201408213.

[11] J. Phother-Simon, I. Hanif, J. Liske, T. Jonsson, The influence of a KCl-rich environment on the corrosion attack of 304 L: 3D FIB/SEM and TEM investigations, Corros Sci 183 (2021) 109315. https://doi.org/10.1016/J.CORSCI.2021.109315.

[12] Y.C. Malede, J.P. Simon, T. Jonsson, M. Montgomery, K. V Dahl, J. Hald, KCl-induced corrosion of Ni-based alloys containing 35–45 wt% Cr, Materials and Corrosion 70 (2019) 1486–1506. https://doi.org/10.1002/maco.201810658.

[13] N. Israelsson, K. Hellström, J.-E. Svensson, L.-G. Johansson, KCl-Induced Corrosion of the FeCrAl Alloy Kanthal® AF at 600 °C and the Effect of H2O, Oxidation of Metals 83 (2015) 1–27. https://doi.org/10.1007/s11085-014-9506-3.

[14] J. Sui, J. Lehmusto, M. Bergelin, M. Hupa, The Effects of KCl, NaCl and K2CO3 on the High-Temperature Oxidation Onset of Sanicro 28 Steel, Oxidation of Metals 85 (2016) 565–598. https://doi.org/10.1007/s11085-016-9613-4.

[15] J. Pettersson, N. Folkeson, L.-G. Johansson, J.-E. Svensson, The Effects of KCl, K2SO4 and K2CO3 on the High Temperature Corrosion of a 304-Type Austenitic Stainless Steel, Oxidation of Metals 76 (2011) 93–109. https://doi.org/10.1007/s11085-011-9240-z.

[16] S. Enestam, D. Bankiewicz, J. Tuiremo, K. Mäkelä, M. Hupa, Are NaCl and KCl equally corrosive on superheater materials of steam boilers?, (2012). https://doi.org/10.1016/j.fuel.2012.07.020.

[17] S. Karlsson, J. Pettersson, L.-G. Johansson, J.-E. Svensson, Alkali Induced High Temperature Corrosion of Stainless Steel: The Influence of NaCl, KCl and CaCl2, Oxidation of Metals 78 (2012) 83–102. https://doi.org/10.1007/s11085-012-9293-7.

[18] L. Reddy, M. Sattari, C.J. Davis, P.H. Shipway, M. Halvarsson, T. Hussain, Influence of KCl and HCl on a laser clad FeCrAl alloy: In-Situ SEM and controlled environment High temperature corrosion, Corros Sci 158 (2019) 108076. https://doi.org/10.1016/J.CORSCI.2019.07.003.

[19] J. Eklund, I. Hanif, S. Bigdeli, T. Jonsson, High temperature corrosion behavior of FeCrAlSi model alloys in the presence of water vapor and KCl at 600 °C – The influence of Cr content, Corros Sci 198 (2022) 110114. https://doi.org/10.1016/J.CORSCI.2022.110114.

[20] J. Lehmusto, P. Yrjas, B.J. Skrifvars, M. Hupa, High temperature corrosion of superheater steels by KCl and K2CO3 under dry and wet conditions, Fuel Processing Technology 104 (2012) 253–264. https://doi.org/10.1016/J.FUPROC.2012.05.020.

[21] K.O. Davidsson, L.-E. Åmand, B. Leckner, B. Kovacevik, M. Svane, M. Hagström, J.B.C. Pettersson, J. Pettersson, H. Asteman, J.-E. Svensson, L.-G. Johansson, Potassium, Chlorine, and Sulfur in Ash, Particles, Deposits, and Corrosion during Wood Combustion in a Circulating Fluidized-Bed Boiler, (2007). https://doi.org/10.1021/ef060306c.

[22] T. Jonsson, B. Pujilaksono, A. Fuchs, J.E. Svensson, L.G. Johansson, M. Halvarsson, The influence of H2O on iron oxidation at 600ºC: A microstructural study, Materials Science Forum 595–598 (2008) 1005–1012. https://doi.org/10.4028/www.scientific.net/MSF.595-598.1005.

[23] D.J. Young, Corrosion in Complex Environments, High Temperature Oxidation and Corrosion of Metals (2016) 603–645. https://doi.org/10.1016/B978-0-08-100101-1.00012-1.

[24] S.C. Okoro, S. Kiamehr, M. Montgomery, F.J. Frandsen, K. Pantleon, Effect of flue gas composition on deposit induced high temperature corrosion under laboratory conditions mimicking biomass firing. Part I: Exposures in oxidizing and chlorinating atmospheres, Materials and Corrosion 68 (2017) 499–514. https://doi.org/10.1002/maco.201609173.

[25] W. Ma, T. Wenga, F.J. Frandsen, B. Yan, G. Chen, The fate of chlorine during MSW incineration: Vaporization, transformation, deposition, corrosion and remedies, Prog Energy Combust Sci 76 (2020) 100789. https://doi.org/10.1016/j.pecs.2019.100789.

[26] J.R. Keiser, W.B.A. (Sandy) Sharp, D.L. Singbeil, P.M. Singh, L.A. Frederick, J.F. Meyer, IMPROVING HEAT RECOVERY IN BIOMASS-FIRED BOILERS, Oak Ridge, 2013. https://info.ornl.gov/sites/publications/files/Pub44810.pdf.

[27] M. Broström, H. Kassman, A. Helgesson, M. Berg, C. Andersson, R. Backman, A. Nordin, Sulfation of corrosive alkali chlorides by ammonium sulfate in a biomass fired CFB boiler, Fuel Processing Technology 88 (2007) 1171–1177. https://doi.org/10.1016/j.fuproc.2007.06.023.

[28] G.Y. Lai, Waste-to-Energy Boilers and Waste Incinerators, in: High-Temperature Corrosion and Materials Applications, Lai, George Y, ASM International, 2007: pp. 335–358.

[29] G.Y. Lai, P.N. Hulsizer, S. Court, Norcross, CORROSION CONTROL BY MODERN WELD OVERLAY TECHNOLOGY, in: 1999. https://api.semanticscholar.org/CorpusID:149447170.

[30] K. Sipilä, Cogeneration, biomass, waste to energy and industrial waste heat for district heating, Advanced District Heating and Cooling (DHC) Systems (2016) 45–73. https://doi.org/10.1016/B978-1-78242-374-4.00003-3.

[31] Directorate-General for Energy, Review of the Reference Values for High-Efficiency Cogeneration, United Kingdom, 2015. https://doi.org/Ref: ED59519.

[32] A. Faaij, Modern Biomass Conversion Technologies, Mitig Adapt Strateg Glob Chang 11 (2006) 343–375. https://doi.org/10.1007/s11027-005-9004-7.

[33] S. Andersson, M.D. Paz, J. Phother-Simon, T. Jonsson, High temperature corrosion and dioxin abatement using sulfur recirculation in a waste-to-energy plant, Detritus 5 (2019) 92–98. https://doi.org/10.31025/2611-4135/2019.13784.

[34] N. Scarlat, J.F. Dallemand, F. Monforti-Ferrario, M. Banja, V. Motola, Renewable energy policy framework and bioenergy contribution in the European Union – An overview from National Renewable Energy Action Plans and Progress Reports, Renewable and Sustainable Energy Reviews 51 (2015) 969–985. https://doi.org/10.1016/J.RSER.2015.06.062.

[35] J.R. Centre, Brief on biomass for energy in the European Union, 2019. https://doi.org/10.2760/546943.

[36] A. Thorenz, L. Wietschel, D. Stindt, A. Tuma, Assessment of agroforestry residue potentials for the bioeconomy in the European Union, J Clean Prod 176 (2018) 348–359. https://doi.org/10.1016/J.JCLEPRO.2017.12.143.

[37] S. Caillat, E. Vakkilainen, Large-scale biomass combustion plants: an overview, Biomass Combustion Science, Technology and Engineering (2013) 189–224. https://doi.org/10.1533/9780857097439.3.189.

[38] C. Yin, L.A. Rosendahl, S.K. Kær, Grate-firing of biomass for heat and power production, Prog Energy Combust Sci 34 (2008) 725–754. https://doi.org/10.1016/J.PECS.2008.05.002.

[39] Babcock & Wilcox Company, Fluidized Bed boiler, (n.d.).

[40] A. Corcoran, J. Marinkovic, F. Lind, H. Thunman, P. Knutsson, M. Seemann, Ash Properties of Ilmenite Used as Bed Material for Combustion of Biomass in a Circulating Fluidized Bed Boiler, Energy & Fuels 28 (2014) 7672–7679. https://doi.org/10.1021/ef501810u.

[41] Internation Standard Organization, Carbon and low alloy cast steels for general applications (ISO Standard No. 14737:2021), 3rd ed., 2021. https://www.iso.org/standard/79985.html (accessed March 13, 2023).

[42] International Organization for Standardization, Stainless steels — Chemical composition (ISO Standard No. 15510:2014), 2nd ed., 2014. https://www.iso.org/standard/61187.html (accessed March 10, 2023).

[43] P. Lambert, 6 - Sustainability of metals and alloys in construction, in: J.M. Khatib (Ed.), Sustainability of Construction Materials, Woodhead Publishing, 2009: pp. 148–170. https://doi.org/10.1533/9781845695842.148.

[44] P. Kofstad, High temperature corrosion, Elsevier Applied Science Publishers, Crown House, Linton Road, Barking, Essex IG 11 8 JU, UK, 1988. (1988).

[45] I. Gaballah, N. Kanari, S. Ivanaj, Kinetics of chlorination and oxychlorination of chromium (III) oxide, Metallurgical and Materials Transactions A 29 (1998) 1299–1308. https://doi.org/10.1007/s11661-998-0256-1.

[46] J.M. Wheeldon, J.P. Shingledecker, Materials for boilers operating under supercritical steam conditions, Ultra-Supercritical Coal Power Plants: Materials, Technologies and Optimisation (2013) 81–103. https://doi.org/10.1533/9780857097514.1.81.

[47] Y.S. Li, Y. Niu, M. Spiegel, High temperature interaction of Al/Si-modified Fe–Cr alloys with KCl, Corros Sci 49 (2007) 1799–1815. https://doi.org/10.1016/j.corsci.2006.10.019.

[48] J. Eklund, M.D. Paz, B. Jönsson, J. Liske, J.-E. Svensson, T. Jonsson, Field exposure of FeCrAl model alloys in a waste-fired boiler at 600°C: The influence of Cr and Si on the corrosion behaviour, Materials and Corrosion 70 (2019) 1476–1485. https://doi.org/10.1002/maco.201810618.

[49] J. Eklund, B. Jönsson, A. Persdotter, J. Liske, J.-E. Svensson, T. Jonsson, The influence of silicon on the corrosion properties of FeCrAl model alloys in oxidizing environments at 600 °C, Corros Sci 144 (2018) 266–276. https://doi.org/10.1016/j.corsci.2018.09.004.

[50] M. Subanović, J. Pirón, F. Zeller, M. Jarrar, A. Schneider, DEVELOPMENT OF A NEW HIGH-PERFORMANCE MARTENSITIC HEATRESISTANT STEEL FOR BOILER APPLICATIONS, in: Proceedings of the ASME 2018 Symposium on Elevated Temperature Application of Materials for Fossil, Nuclear, and Petrochemical Industries. ASME 2018 Symposium on Elevated Temperature Application of Materials for Fossil, Nuclear, and Petrochemical Industri, Seattle, 2018. https://doi.org/10.1115/ETAM2018-6748.

[51] M. Subanović, J. Pirón, F. Zeller, M. Jarrar, A. Schneider, Super VM12 - A New 12% Cr Boiler Steel, in: J. Shingledecker, M. Takeyama (Eds.), Joint EPRI – 123HiMAT International Conference on Advances in High Temperature Materials, ASM International, 2019: pp. 205–216. https://books.google.se/books?id=zbq9DwAAQBAJ&lpg=PA207&vq=Super VM12&pg=PA205#v=snippet&q=Super VM12 &f=false.

[52] M.M.A. Bepari, K.M. Shorowordi, Effects of molybdenum and nickel additions on the structure and properties of carburized and hardened low carbon steels, J Mater Process Technol 155–156 (2004) 1972–1979. https://doi.org/10.1016/j.jmatprotec.2004.04.060.

[53] J. You, H.G. Kim, J. Lee, H.-H. Kim, Y. Cho, B.-S. Jeong, K. Kang, H.M. Lee, H.N. Han, M. Kim, S.-H. Hong, Effects of molybdenum addition on microstructure and mechanical properties of Fe-B-C sintered alloys, Mater Charact 173 (2021) 110915. https://doi.org/10.1016/j.matchar.2021.110915.

[54] inQbrands, Boiler Steel Tube Price, (2023). https://www.made-in-china.com/ (accessed February 20, 2023).

[55] E. Sadeghi, N. Markocsan, S. Joshi, Advances in Corrosion-Resistant Thermal Spray Coatings for Renewable Energy Power Plants. Part I: Effect of Composition and Microstructure, Journal of Thermal Spray Technology 28 (2019) 1749–1788. https://doi.org/10.1007/s11666-019-00938-1.

[56] Frank B. Quinlan, Lloyd P. Grobe, TREATMENT OF METALS, 2,303,869, 1942.

[57] S. Zanzarin, S. Bengtsson, A. Molinari, Study of dilution in laser cladding of a carbon steel substrate with Co alloy powders, Powder Metallurgy 59 (2016) 85–94. https://doi.org/10.1080/00325899.2015.1118842.

[58] S.S. Sandhu, A.S. Shahi, Metallurgical, wear and fatigue performance of Inconel 625 weld claddings, J Mater Process Technol 233 (2016) 1–8. https://doi.org/10.1016/j.jmatprotec.2016.02.010.

[59] S. Bigdeli, L. Kjellqvist, R. Naraghi, L. Höglund, H. Larsson, T. Jonsson, Strategies for High-Temperature Corrosion Simulations of Fe-Based Alloys Using the Calphad Approach: Part I, J Phase Equilibria Diffus 42 (2021) 403–418. https://doi.org/10.1007/s11669-021-00893-x.

[60] N Cabrera, N F Mott, Theory of the oxidation of metals, Reports on Progress in Physics 12 (1949) 163. https://doi.org/10.1088/0034-4885/12/1/308.

[61] C. Wagner, Beitrag zur Theorie des Anlaufvorgangs, 21B (1933) 25–41. https://doi.org/doi:10.1515/zpch-1933-2105.

[62] L. Bataillou, C. Desgranges, L. Martinelli, D. Monceau, Modelling of the effect of grain boundary diffusion on the oxidation of Ni-Cr alloys at high temperature, Corros Sci 136 (2018) 148–160. https://doi.org/10.1016/J.CORSCI.2018.03.001.

[63] W.J. Quadakkers, D. Naumenko, E. Wessel, V. Kochubey, L. Singheiser, Growth Rates of Alumina Scales on Fe–Cr–Al Alloys, Oxidation of Metals 61 (2004) 17–37. https://doi.org/10.1023/B:OXID.0000016274.78642.ae.

[64] A. Persdotter, J. Eklund, J. Liske, T. Jonsson, Beyond breakaway corrosion – Influence of chromium, nickel and aluminum on corrosion of iron-based alloys at 600 °C, Corros Sci 177 (2020) 108961. https://doi.org/10.1016/j.corsci.2020.108961.

[65] A. Galerie, S. Henry, Y. Wouters, M. Mermoux, J.-P. Petit, L. Antoni, Mechanisms of chromia scale failure during the course of 15–18Cr ferritic stainless steel oxidation in water vapour, Materials at High Temperatures 22 (2005) 105–112. https://doi.org/10.1179/mht.2005.012.

[66] V.K. Tolpygo, D.R. Clarke, Alumina scale failure resulting from stress relaxation, Surf Coat Technol 120–121 (1999) 1–7. https://doi.org/10.1016/S0257-8972(99)00331-X.

[67] B. Chattopadhyay, G.C. Wood, The transient oxidation of alloys, Oxidation of Metals 2 (1970) 373–399. https://doi.org/10.1007/BF00604477.

[68] G.C. Wood, High-temperature oxidation of alloys, Oxidation of Metals 2 (1970) 11–57. https://doi.org/10.1007/BF00603581.

[69] H. Asteman, J.-E. Svensson, L.-G. Johansson, Effect of Water-Vapor-Induced Cr Vaporization on the Oxidation of Austenitic Stainless Steels at 700 and 900°C, J Electrochem Soc 151 (2004) B141. https://doi.org/10.1149/1.1644138.

[70] F.H. Stott, G.C. Wood, J. Stringer, The influence of alloying elements on the development and maintenance of protective scales, Oxidation of Metals 44 (1995) 113–145. https://doi.org/10.1007/BF01046725.

[71] H.El. Kadiri, R. Molins, Y. Bienvenu, M.F. Horstemeyer, Abnormal High Growth Rates of Metastable Aluminas on FeCrAl Alloys, Oxidation of Metals 64 (2005) 63–97. https://doi.org/10.1007/s11085-005-5715-0.

[72] A. Agüero, P. Audigié, S. Rodríguez, M. Gutiérrez del Olmo, J. Pascual, V. Ssenteza, T. Jonsson, L.-G. Johansson, Rapid α-Al2O3 Growth on an Iron Aluminide Coating at 600 °C in the Presence of O2, H2O, and KCl, ACS Appl Mater Interfaces (2024). https://doi.org/10.1021/acsami.4c11719.

[73] B. Pujilaksono, T. Jonsson, M. Halvarsson, J.-E. Svensson, L.-G. Johansson, Oxidation of iron at 400–600 °C in dry and wet O2, Corros Sci 52 (2010) 1560–1569. https://doi.org/10.1016/J.CORSCI.2010.01.002.

[74] J. Töpfer, S. Aggarwal, R. Dieckmann, Point defects and cation tracer diffusion in (CrxFe1 − x)3 − δO4 spinels, Solid State Ion 81 (1995) 251–266. https://doi.org/10.1016/0167-2738(95)00190-H.

[75] R. Dieckmann, M.R. Hilton, T.O. Mason, Defects and Cation Diffusion in Magnetite (VIII): Migration Enthalpies for Iron and Impurity Cations, Berichte Der Bunsengesellschaft Für Physikalische Chemie 91 (1987) 59–66. https://doi.org/10.1002/bbpc.19870910113.

[76] A. Col, V. Parry, C. Pascal, Oxidation of a Fe–18Cr–8Ni austenitic stainless steel at 850 °C in O2: Microstructure evolution during breakaway oxidation, Corros Sci 114 (2017) 17–27. https://doi.org/10.1016/j.corsci.2016.10.029.

[77] H.W. Grünling, R. Bauer, The role of silicon in corrosion-resistant high temperature coatings, Thin Solid Films 95 (1982) 3–20. https://doi.org/10.1016/0040-6090(82)90578-8.

[78] V. Ssenteza, J. Eklund, I. Hanif, J. Liske, T. Jonsson, High temperature corrosion resistance of FeCr(Ni, Al) alloys as bulk/overlay weld coatings in the presence of KCl at 600 °C, Corros Sci 213 (2023) 110896. https://doi.org/10.1016/J.CORSCI.2022.110896.

[79] N. Israelsson, K.A. Unocic, K. Hellström, T. Jonsson, M. Norell, J.-E. Svensson, L.-G. Johansson, A Microstructural and Kinetic Investigation of the KCl-Induced Corrosion of an FeCrAl Alloy at 600 °C, Oxidation of Metals 84 (2015) 105–127. https://doi.org/10.1007/s11085-015-9546-3.

[80] M. Cao, L. Liu, Z. Yu, L. Fan, L. Ying, F. Wang, Studies on the corrosion behavior of Fe-20Cr alloy in NaCl solution spray at 600 °C, Corros Sci 133 (2018) 165–177. https://doi.org/10.1016/j.corsci.2018.01.033.

[81] S. Karlsson, J. Pettersson, L.-G. Johansson, J.-E. Svensson, Alkali Induced High Temperature Corrosion of Stainless Steel: The Influence of NaCl, KCl and CaCl2, Oxidation of Metals 78 (2012) 83–102. https://doi.org/10.1007/s11085-012-9293-7.

[82] C. Pettersson, L.-G. Johansson, J.-E. Svensson, The Influence of Small Amounts of KCl(s) on the Initial Stages of the Corrosion of Alloy Sanicro 28 at 600 °C, Oxidation of Metals 70 (2008) 241–256. https://doi.org/10.1007/s11085-008-9118-x.

[83] J. Lehmusto, M. Sattari, M. Halvarsson, L. Hupa, Should the oxygen source be considered in the initiation of KCl-induced high-temperature corrosion?, Corros Sci 183 (2021) 109332. https://doi.org/10.1016/j.corsci.2021.109332.

[84] J. Sui, J. Lehmusto, M. Bergelin, M. Hupa, The Effects of KCl, NaCl and K2CO3 on the High-Temperature Oxidation Onset of Sanicro 28 Steel, Oxidation of Metals 85 (2016) 565–598. https://doi.org/10.1007/s11085-016-9613-4.

[85] M. Mcnallan, W.W. Liang, S.H. Kim, C.T. Kang, ACCELERATION OF THE HIGH TEMPERATURE OXIDATION OF METALS BY CHLORINE., NACE (1983) 316–321.

[86] H.J. Grabke, E. Reese, M. Spiegel, The effects of chlorides, hydrogen chloride, and sulfur dioxide in the oxidation of steels below deposits, Corros Sci 37 (1995) 1023–1043. https://doi.org/10.1016/0010-938X(95)00011-8.

[87] N. Folkeson, L.-G. Johansson, J.-E. Svensson, Initial Stages of the HCl-Induced High-Temperature Corrosion of Alloy 310, J Electrochem Soc 154 (2007) C515. https://doi.org/10.1149/1.2754174.

[88] H. Asteman, J.-E. Svensson, L.-G. Johansson, M. Norell, Indication of Chromium Oxide Hydroxide Evaporation During Oxidation of 304L at 873 K in the Presence of 10% Water Vapor, Oxidation of Metals 52 (1999) 95–111. https://doi.org/10.1023/A:1018875024306.

[89] H. Asteman, J.-E. Svensson, M. Norell, L.-G. Johansson, Influence of Water Vapor and Flow Rate on the High-Temperature Oxidation of 304L; Effect of Chromium Oxide Hydroxide Evaporation, Oxidation of Metals 54 (2000) 11–26. https://doi.org/10.1023/A:1004642310974.

[90] M. Halvarsson, J.E. Tang, H. Asteman, J.-E. Svensson, L.-G. Johansson, Microstructural investigation of the breakdown of the protective oxide scale on a 304 steel in the presence of oxygen and water vapour at 600 °C, Corros Sci 48 (2006) 2014–2035. https://doi.org/10.1016/j.corsci.2005.08.012.

[91] H. Asteman, J.-E. Svensson, L.-G. Johansson, Evidence for Chromium Evaporation Influencing the Oxidation of 304L: The Effect of Temperature and Flow Rate, Oxidation of Metals 57 (2002) 193–216. https://doi.org/10.1023/A:1014877600235.

[92] E. Essuman, G.H. Meier, J. Zurek, M. Hänsel, L. Singheiser, W.J. Quadakkers, Enhanced internal oxidation as trigger for breakaway oxidation of Fe–Cr alloys in gases containing water vapor, Scr Mater 57 (2007) 845–848. https://doi.org/10.1016/J.SCRIPTAMAT.2007.06.058.

[93] J. Eklund, A. Persdotter, V. Ssenteza, T. Jonsson, The long-term corrosion behavior of FeCrAl(Si) alloys after breakaway oxidation at 600 °C, Corros Sci 217 (2023) 111155. https://doi.org/10.1016/j.corsci.2023.111155.

[94] A. Ul-Hamid, A beginners' guide to scanning electron microscopy, Springer, 2018.

[95] J.I. Goldstein, D.E. Newbury, J.R. Michael, N.W.M. Ritchie, J.H.J. Scott, D.C. Joy, Scanning electron microscopy and X-ray microanalysis, Third edit, Springer, 2017.

[96] A.J. Wilkinson, P.B. Hirsch, Electron diffraction based techniques in scanning electron microscopy of bulk materials, Micron 28 (1997) 279–308. https://doi.org/10.1016/S0968-4328(97)00032-2.

[97] D.B. Williams, C.B. Carter, Transmission Electron Microscopy, 2nd ed. 20, Springer US, 2009. https://doi.org/10.1007/978-0-387-76501-3 (accessed February 25, 2025).

[98] ASTM international, Standard Test Methods for Determining Average Grain Size, PA 19428-2959, 2013. https://doi.org/Designation: E112 − 12.

[99] R.S. Bradley, P. Volans, R. Whytlaw- Gray, Rates of evaporation VI. The vapour pressure and rate of evaporation of potassium chloride, Proc R Soc Lond A Math Phys Sci 217 (1997) 508–523. https://doi.org/10.1098/rspa.1953.0076.

[100] X. Montero, A. Ishida, M. Rudolphi, H. Murakami, M.C. Galetz, Breakaway corrosion of austenitic steel induced by fireside corrosion, Corros Sci 173 (2020) 108765. https://doi.org/10.1016/j.corsci.2020.108765.

[101] F. Liu, J.E. Tang, T. Jonsson, S. Canovic, K. Segerdahl, J.E. Svensson, M. Halvarsson, Microstructural investigation of protective and non-protective oxides on 11% chromium steel, Oxidation of Metals 66 (2006) 295–319. https://doi.org/10.1007/s11085-006-9035-9.

[102] V. Ssenteza, Materials and Coatings for Superheater Tubes in Biomass- and Waste-fired Boilers Insights into long-term high-temperature corrosion behaviour, LICENTIATE THESIS, Chalmers University of Technology, 2023.

[103] B. Liu, X. Chen, Impacts of Temperature and KCl on Corrosion Behavior of 12Cr1MoVG and T91 in HCl-Containing Atmosphere, Oxidation of Metals 90 (2018) 585–597. https://doi.org/10.1007/s11085-018-9864-3.

[104] T. Jonsson, B. Pujilaksono, H. Heidari, F. Liu, J.E. Svensson, M. Halvarsson, L.G. Johansson, Oxidation of Fe–10Cr in O2 and in O2 + H2O environment at 600 °C: A microstructural investigation, Corros Sci 75 (2013) 326–336. https://doi.org/10.1016/J.CORSCI.2013.06.016.

[105] J. Eklund, A. Persdotter, I. Hanif, S. Bigdeli, T. Jonsson, Secondary corrosion protection of FeCr(Al) model alloys at 600 °C – The influence of Cr and Al after breakaway corrosion, Corros Sci 189 (2021) 109584. https://doi.org/10.1016/J.CORSCI.2021.109584.

[106] J. Eklund, B. Paz, Maria Dolores Jönsson, J. Liske, J.-E. Svensson, T. Jonsson, Field exposure of FeCrAl model alloys in a waste-fired boiler at 600°C: The influence of Cr and Si on the corrosion behaviour, Materials and Corrosion 70 (2019) 1476– 1485.

[107] S. Hallström, M. Halvarsson, L. Höglund, T. Jonsson, J. Ågren, High temperature oxidation of chromium: Kinetic modeling and microstructural investigation, Solid State Ion 240 (2013) 41–50. https://doi.org/10.1016/j.ssi.2013.02.017.

[108] X. Peng, J. Yan, Y. Zhou, F. Wang, Effect of grain refinement on the resistance of 304 stainless steel to breakaway oxidation in wet air, Acta Mater 53 (2005) 5079–5088. https://doi.org/10.1016/J.ACTAMAT.2005.07.019.

[109] V. Trindade, H.-J. Christ, U. Krupp, Grain-Size Effects on the High-Temperature Oxidation Behaviour of Chromium Steels, Oxidation of Metals 73 (2010) 551–563. https://doi.org/10.1007/s11085-010-9192-8.

[110] M. Schütze, P.F. Tortorelli, I.G. Wright, Development of a Comprehensive Oxide Scale Failure Diagram, Oxidation of Metals 73 (2010) 389–418. https://doi.org/10.1007/s11085-009-9185-7.

[111] Y.S. Li, Y. Niu, M. Spiegel, High temperature interaction of Al/Si-modified Fe–Cr alloys with KCl, Corros Sci 49 (2007) 1799–1815. https://doi.org/10.1016/j.corsci.2006.10.019.

[112] A. Persdotter, H. Larsson, J. Eklund, S. Bigdeli, T. Jonsson, The influence of Nickel on the corrosion protection of FeCrNi alloys after breakaway corrosion at 600 °C, Corros Sci 240 (2024) 112473. https://doi.org/10.1016/j.corsci.2024.112473.

[113] S. Karlsson, T. Jonsson, J. Hall, J.-E. Svensson, J. Liske, Mitigation of Fireside Corrosion of Stainless Steel in Power Plants: A Laboratory Study of the Influences of SO2 and KCl on Initial Stages of Corrosion, Energy & Fuels 28 (2014) 3102–3109. https://doi.org/10.1021/ef402127h.

[114] X. Liang, Y. Zhong, S. Zhu, H. He, P. Yuan, J. Zhu, Z. Jiang, The valence and site occupancy of substituting metals in magnetite spinel structure Fe3−xMxO4 (M = Cr, Mn, Co and Ni) and their influence on thermal stability: An XANES and TG-DSC investigation, Solid State Sci 15 (2013) 115–122. https://doi.org/10.1016/j.solidstatesciences.2012.10.005.

[115] A. Stålenheim, P. Henderson, Materials for higher steam temperatures(up to 600°C) in biomass and waste fired plant - a review of present knowledge, Stockholm, 2011.

[116] W.B.A. Sharp, W. Frederick, J.R. Keiser, D.L. Singbeil, Could biomass-fueled boilers be operated at higher steam temperatures? Part 3: Initial analysis of costs and benefits, Tappi J 13 (2014) 65–78.